

Impact of Unit Web Height on the Structural Performance of Concrete Masonry Prisms

A Thesis Submitted to the College of

Graduate and Postdoctoral Studies

In Partial Fulfillment of the Requirements

For the Degree of Master of Science

In the Department of Civil, Geological, and Environmental Engineering

University of Saskatchewan

Saskatoon, SK, Canada

By

NITESH CHHETRI

© Copyright Nitesh Chhetri, September, 2022. All rights reserved.

Unless otherwise noted, copyright of the material in this thesis belongs to the author

PERMISSION TO USE

In presenting this thesis in partial fulfillment of the requirements for a Postgraduate degree from the University of Saskatchewan, I agree that the Libraries of this University may make it freely available for inspection. I further agree that permission for copying of this thesis in any manner, in whole or in part, for scholarly purposes may be granted by the professor or professors who supervised my thesis work or, in their absence, by the Head of the Department or the Dean of the College in which my thesis work was done. It is understood that any copying or publication or use of this thesis or parts thereof for financial gain shall not be allowed without my written permission. It is also understood that due recognition shall be given to me and to the University of Saskatchewan in any scholarly use which may be made of any material in my thesis.

Requests for permission to copy or to make other uses of materials in this thesis/dissertation in whole or part should be addressed to:

Head of the Department
Civil, Geological, and Environmental Engineering
University of Saskatchewan
57 Campus Drive
Saskatoon, Saskatchewan S7N 5A9
Canada

Or

Dean
College of Graduate and Postdoctoral Studies
University of Saskatchewan
116 Thorvaldson Building, 110 Science Place
Saskatoon, Saskatchewan S7N 5C9
Canada

ABSTRACT

Webs are responsible for the transfer of shear stress between the face shells of concrete masonry units (CMUs) and provide structural stability. Any changes to their geometry (i.e., their height and/or thickness) might therefore impact the structural performance of masonry members. While CAN/CSA S304-14 stipulates minimum web thickness requirements for each CMU size, there are no provisions for web height other than full-height web and so that would limit the range of CMU configurations. Nonetheless, Canadian block suppliers typically limit knock-out webs to heights of about 120 mm. In contrast, U.S. code ASTM C90-11 stipulates the web configurations of CMUs by minimum normalized web area requirements which allow for varying web heights including, but not limited to, web heights that are shorter than those typically used for Canadian knock-out web units. Shorter web heights reduce structural self-weight, and potentially minimize worker fatigue and injuries, and so would increase construction productivity. An extensive literature review did not, however, reveal the existence of published studies related to the impact of web height of CMUs on the structural performance of masonry assemblages.

An experimental investigation of three-course tall by one block wide masonry prisms was therefore conducted to evaluate the impact of CMU web height on the masonry assemblage strength and failure modes of prisms. Prisms constructed in running bond with face-shell mortar bedding were constructed and the following parameters were investigated: CMU size, web height, and the use of grout. A total of 18 unique prism configurations with 7 replicates of each resulted in a total of 126 prisms. The actuators available in the laboratory were used for compression testing; in addition, a digital image correlation (DIC) system was used to capture the deformation properties. The analysis of compression test results revealed that CMU web height was an influential parameter on the masonry assemblage strength of hollow prisms but not of grouted prisms, irrespective of CMU size. Failure of both hollow and grouted prisms, obtained from the DIC system results, was primarily governed by the tensile splitting of the webs, but the crack patterns varied with web height. Finite element modeling (FEM) of prisms within selected test series was conducted to predict the potential crack locations within the webs and results were in a good agreement with those obtained from the DIC system. It was found that CMUs with web heights shorter than typically used in Canadian masonry construction could be used without significantly compromising the structural performance of masonry members.

CO-AUTHORSHIP

All of the experimental work presented in this thesis was conducted by Nitesh Chhetri and reviewed by Dr. L.R Feldman. The results on failure modes of a select number of masonry prisms included in the experimental program were presented at the 2022 CSCE Annual General Conference in Whistler, BC, Canada and will be published in the upcoming proceedings. A journal manuscript will be prepared presenting the overall experimental program and resulting analysis at a later date.

ACKNOWLEDGEMENTS

The author would like to express utmost gratitude to his supervisor, Dr. Lisa R. Feldman, for her continuous support, guidance, and mentorship in preparing this thesis. The valuable feedback and constant encouragement from her will always be appreciated. The author also gratefully acknowledges the valuable advice from his advisory committee members: Dr. Mohamed Boulfiza, and Dr. Bruce Sparling.

The author would also like to extend a special thank you to the Structural Laboratory Technician, Brennan Pokoyoway, for his support throughout the laboratory work period and fellow graduate student, Gordon Chui, for his continuous help and support throughout the program duration. The author also acknowledges the help from other fellow graduate students: Thomas Vachon and Olga Savkina. A special thank-you is extended to close friend Uliana Morozovskaia for her continuous support and encouragement in the preparation of this thesis.

The author would like to thank Sasha Kisin from the Saskatchewan Masonry Institute for providing construction materials and mason's time for the construction of the specimens. The author also acknowledges the help from Monty and Rupert in constructing all the masonry prisms included in this experimental investigation.

The author gratefully acknowledges the financial support provided by the Canada Masonry Design Centre, the Saskatchewan Centre for Masonry Design, the Saskatchewan Masonry Institute, and scholarship provided by the University of Saskatchewan.

Finally, the author sincerely thanks his family members and friends for their continuous support and encouragement.

TABLE OF CONTENTS

Permission to Use	i
Abstract	ii
Co-Authorship.....	iii
Acknowledgements.....	iv
Table of Contents.....	v
List of Tables	ix
List of Figures	xi
List of Symbols.....	xvi
CHAPTER 1: Introduction	1
1.1 Background	1
1.2 Research Objectives	3
1.3 Methodology and Scope.....	3
1.4 Thesis Outline	4
CHAPTER 2: Literature Review	6
2.1 Introduction	6
2.2 Comparison Between CSA A165.1 and ASTM C90 in Terms of Minimum Geometric Requirements for the Webs in Hollow CMUs.....	7
2.3 Mechanics of Load Transfer in Concrete Masonry Assemblages Subjected to Axial Compression.....	10
2.4 Influential Parameters on Masonry Assemblage Strength	11
2.4.1 CMU Size.....	11
2.4.2 CMU Web Geometry.....	13
2.4.3 Presence of Grout.....	14

2.4.4	Height-to-Thickness (h/t) Ratio	16
2.5	Statistical Parameters for Masonry Prism Replicates	19
2.6	Relevant Studies on Failure Modes of Concrete Masonry Assemblages.....	20
2.7	Summary	22
CHAPTER 3: Experimental Design		23
3.1	Introduction	23
3.2	Specimen Description and Test Matrix.....	23
3.3	Construction Materials	26
3.3.1	Concrete Masonry Units	26
3.3.2	Mortar	27
3.3.3	Grout	28
3.4	Construction	28
3.4.1	Mortar Preparation	29
3.4.2	Grout Preparation.....	30
3.4.3	Prism Construction.....	32
3.5	Instrumentation and Testing.....	34
3.5.1	Setup of the Digital Image Correlation System	35
3.5.2	Loading Frame and Testing Procedures	36
3.5.3	Testing of Companion Specimens	39
3.6	Summary	41
CHAPTER 4: Experimental Results and Analysis		42
4.1	Companion Specimen Test Results.....	43
4.1.1	Concrete Masonry Units	43
4.1.2	Mortar Cubes	44

4.1.3	Non-Absorbent Grout Cylinders and Absorptive Grout Prisms	45
4.2	Masonry Prism Compression Test Results and Analysis.....	47
4.2.1	Hollow Prisms.....	48
4.2.2	Grouted Prisms.....	53
4.2.3	Comparison of Experimental Results with CSA S304-14.....	57
4.3	DIC Results and Analysis	59
4.3.1	Crack Patterns and Failure Modes	59
4.3.2	Stress versus Strain Characteristics	68
4.4	FEM Analysis and Results	73
4.5	Practical Implications	80
4.6	Summary	81
CHAPTER 5: Conclusions and Recommendations.....		83
5.1	Overview	83
5.2	Conclusions	84
5.2.1	Influence of CMU Web Height on the Resulting Masonry Assemblage Strength. 84	
5.2.2	Determining Statistical Difference in Masonry Assemblage Strength Between Prisms Constructed Using CMUs with Web Height Conforming to CSA A165.1 and ASTM C90.....	84
5.2.3	Influence of CMU Web Height on the Failure Mode of Masonry Prisms	85
5.2.4	Comparison of Failure Modes Predicted Using the Finite Element Modeling Approach to Those Evaluated Using the Results Obtained from the DIC System. 86	
5.3	Recommendations for Future Research	87
REFERENCES		88
APPENDICES		92
Appendix 3A: Determination of the Number of Replicate Masonry Prisms.....		93

Appendix 4A: Companion Specimen Test Results.....	95
Appendix 4B: Masonry Prism Compression Test Results.....	101
Appendix 4C: DIC System Results.....	107
Appendix 4D: Finite Element Modeling Results.....	129

LIST OF TABLES

Table 2.1: Minimum Geometric Requirements for the Webs in Hollow CMUs as Specified in CSA A165.1 and ASTM C90	7
Table 2.2: Correction Factors Provided in CSA S304-14.....	18
Table 3.1: Test Matrix.....	26
Table 3.2: Masonry Prism Construction Schedule	32
Table 4.1: Test Schedule.....	42
Table 4.2: Compression Test Results for Concrete Masonry Units.....	43
Table 4.3: Absorption Test Results for Concrete Masonry Units.....	44
Table 4.4: Compression Test Results for Mortar Cubes.....	45
Table 4.5: Compression Test Results for Non-Absorbent Grout Cylinders and Absorptive Grout Prisms.....	46
Table 4.6: Compression Test Results for Masonry Prisms.....	48
Table 4.7: Comparison Between Experimental and Minimum Specified Masonry Compressive Strength.....	58
Table 4.8: Initial Cracking and Peak Load for Prisms within Different Test Series	67
Table 4.9: Mechanical Properties of Materials Used for Finite Element Modeling.....	76
Table 3A- 1: Reported Data for Determining the Required Number of Replicates	93
Table 3A- 2: t-Value and Confidence Level Based on the Number of Replicate Specimens	94
Table 4A-1: As-Measured Minimum CMU Dimensions	96
Table 4A-2: As-Calculated Effective Areas	96
Table 4A-3: CMU Compression Test Results	97
Table 4A-4: CMU Absorption Test Results	97
Table 4A-5: Mortar Cube Compression Test Results.....	98

Table 4A-6: Non-Absorbent Grout Cylinder Test Results	100
Table 4A-7: Absorptive Grout Prism Test Results	100
Table 4B-1: As-Tested Masonry Assemblage Strength for Prisms	102
Table 4B-2: One-Way ANOVA Results.....	103
Table 4B-3: Post-Hoc Analysis Results.....	104
Table 4B-4: Calculation Results for Experimental and Minimum Specified Masonry Compressive Strength.....	106
Table 4C-1: Summary of Initial Cracking and Peak Load	113
Table 4D-1: Maximum Principal Stress Distribution - Test Series A200H	130
Table 4D-2: Maximum Principal Stress Distribution - Test Series B200H.....	132
Table 4D-3: Maximum Principal Stress Distribution - Test Series C200H.....	134

LIST OF FIGURES

Figure 1.1: Typical Geometric Properties of Webs in CMU	2
Figure 2.1: Cross-Sections of Acceptable Web Geometries Allowed in ASTM C90: (a) Standard Stretcher Unit, (b) A-Shaped Unit, (c) H-Shaped Unit, (d) Knock-Out Three Webs Unit, and (e) Knock-Out Single Web Unit.....	8
Figure 2.2: Mechanics of Load Transfer in UngROUTED and Grouted Concrete Masonry Assemblages	10
Figure 2.3: Sectional View of Webs in Successive Courses for Ganesan and Ramamurthy's 1992 Investigation: (a) Misaligned, and (b) Aligned.....	14
Figure 2.4: Prism Dimensions	17
Figure 3.1: CMU Web Heights: (a) CSA A165.1 Regular Stretcher Unit, (b) CSA A165.1 Knock-Out Web Unit, and (c) ASTM C90 Knock-Out Web Unit	24
Figure 3.2: Top View of Prisms Constructed Using: (a) 150 mm CMUs, (b) 200 mm CMUs, and (c) 300 mm CMUs	25
Figure 3.3: Dimensions and Cross-Sections of Standard Concrete Masonry Units of Size: (a) 300 mm (b) 200 mm, and (c) 150 mm.....	27
Figure 3.4: Mortar Preparation: (a) Mortar Mixer, and (b) Cast Mortar Cubes	29
Figure 3.5: Grout Preparation: (a) Grout Mixer, (b) Slump Test, (c) Absorbent Grout Prism, and (d) Non-Absorbent Grout Cylinders	31
Figure 3.6: Formwork: (a) Open-Ended Knock-Out Prisms, (b) Preliminary Formwork, and (c) Completed Formwork	33
Figure 3.7: Prism Curing: (a) Hollow Prisms, and (b) Grouted Prisms.....	34
Figure 3.8: Setup for Digital Image Correlation System	35
Figure 3.9: Painted Face-Shell for DIC: (a) Flat White, and (b) Black Speckle Pattern.....	36
Figure 3.10: Prism Test Setup: (a) Front View, and (b) Side View.....	37
Figure 3.11: Prism Positioned in the Test Setup.....	38

Figure 3.12: Concrete Masonry Unit Test Setup	39
Figure 3.13: Mortar Cube Test Setup	40
Figure 3.14: Non-Absorbent Grout Cylinder Test Setup.....	40
Figure 3.15: Absorptive Grout Prism Test Setup.....	41
Figure 4.1: Assemblage Strength of Hollow Prisms Constructed with 150 mm CMUs	49
Figure 4.2: Assemblage Strength of Hollow Prisms Constructed with 200 mm CMUs	50
Figure 4.3: Assemblage Strength of Hollow Prisms Constructed with 300 mm CMUs	52
Figure 4.4: Summary of Assemblage Strength for Hollow Prisms	53
Figure 4.5: Assemblage Strength of Grouted Prisms Constructed with 150 mm CMUs	54
Figure 4.6: Assemblage Strength of Grouted Prisms Constructed with 200 mm CMUs	56
Figure 4.7: Summary of Assemblage Strength for Grouted Prisms	57
Figure 4.8: Typical Initial Cracking and Peak Load States for a Hollow Prism within Test Series: (a) A200H, (b) B200H, and (c) C200H	61
Figure 4.9: Typical Initial Cracking and Peak Load States for a Hollow Prism within Test Series: (a) A150H, (b) B150H, and (c) C150H	62
Figure 4.10: Typical Initial Cracking and Peak Load States for a Hollow Prism within Test Series: (a) A300H, (b) B300H, and (c) C300H	63
Figure 4.11: Typical Initial Cracking and Peak Load States for a Grouted Prism within Test Series: (a) A200G, (b) B200G, and (c) C200G	65
Figure 4.12: Typical Initial Cracking and Peak Load States for a Grouted Prism within Test Series: (a) A150G, (b) B150G, and (c) C150G	66
Figure 4.13: Typical Axial Stress versus Principal Strain Plot for Prisms within Test Series A200H, B200H, and C200H on: (a) Exterior Web Face, and (b) Face Shell.....	69
Figure 4.14: Typical Axial Stress versus Principal Strain Plot for Prisms within Test Series A150H, B150H, and C150H on the Exterior Web Face.....	70

Figure 4.15: Typical Axial Stress versus Principal Strain Plot for Prisms within Test Series A300H, B300H, and C300H on: (a) Exterior Web Face, and (b) Face Shell.....	71
Figure 4.16: Typical Axial Stress versus Principal Strain Plot for Prisms within Test Series A200G, B200G, and C200G on: (a) Exterior Web Face, and (b) Face Shell.....	72
Figure 4.17: Typical Axial Stress versus Principal Strain Plot for Prisms within Test Series A150G, B150G, and C150G on: (a) Exterior Web Face, and (b) Face Shell.....	73
Figure 4.18: Geometry of Finite Element Prism Model: (a) Typical Masonry Prism Model, (b) Rounded Geometry at the Corners, and (c) Tapered Face Shell Geometry.....	75
Figure 4.19: Maximum Principal Stress Contour Map for Prisms within Test Series: (a) A200H, (b) B200H, and (c) C200H.....	77
Figure 4.20: Maximum Principal Stress Distribution along the Top and Bottom Web Surfaces for Prisms within Test Series: (a) A200H. (b) B200H, and (c) C200H	79
Figure 4B-1: Regression Analysis Plots for Hollow Masonry Prisms	105
Figure 4C-1: Maximum Principal Strain Contour Map at Peak Load on Web Face for Prisms: (a) A150H-1, (b) A150H-2, (c) A150H-3, (d) A150H-4, and (e) A150H-5	108
Figure 4C-2: Maximum Principal Strain Contour Map at Peak Load on Web Face for Prisms: (a) B150H-1, (b) B150H-2, (c) B150H-3, (d) B150H-4, and (e) B150H-5	108
Figure 4C-3: Maximum Principal Strain Contour Map at Peak Load on Web Face for Prisms: (a) C150H-1, (b) C150H-2, (c) C150H-3, (d) C150H-4, and (e) C150H-5	108
Figure 4C-4: Maximum Principal Strain Contour Map at Peak Load on Web Face for Prisms: (a) A200H-1, (b) A200H-2, (c) A200H-3, (d) A200H-4, and (e) A200H-5	109
Figure 4C-5: Maximum Principal Strain Contour Map at Peak Load on Web Face for Prisms: (a) B200H-1, (b) B200H-2, (c) B200H-3, (d) B200H-4, and (e) B200H-5	109
Figure 4C-6: Maximum Principal Strain Contour Map at Peak Load on Web Face for Prisms: (a) C200H-1, (b) C200H-2, (c) C200H-3, (d) C200H-4, and (e) C200H-5	109
Figure 4C-7: Maximum Principal Strain Contour Map at Peak Load on Web Face for Prisms: (a) A300H-1, (b) A300H-2, (c) A300H-3, (d) A300H-4, and (e) A300H-5	110

Figure 4C-8: Maximum Principal Strain Contour Map at Peak Load on Web Face for Prisms: (a) B300H-1, (b) B300H-2, (c) B300H-3, (d) B300H-4, and (e) B300H-5	110
Figure 4C-9: Maximum Principal Strain Contour Map at Peak Load on Web Face for Prisms: (a) C300H-1, (b) C300H-2, (c) C300H-3, (d) C300H-4, and (e) C300H-5	110
Figure 4C-10: Maximum Principal Strain Contour Map at Peak Load on Web Face for Prisms: (a) A150G-1, (b) A150G-2, (c) A150G-3, (d) A150G-4, and (e) A150G-5	111
Figure 4C-11: Maximum Principal Strain Contour Map at Peak Load on Web Face for Prisms: (a) B150G-1, (b) B150G-2, (c) B150G-3, (d) B150G-4, and (e) B150G-5	111
Figure 4C-12: Maximum Principal Strain Contour Map at Peak Load on Web Face for Prisms: (a) C150G-1, (b) C150G-2, (c) C150G-3, (d) C150G-4, and (e) C150G-5	111
Figure 4C-13: Maximum Principal Strain Contour Map at Peak Load on Web Face for Prisms: (a) A200G-1, (b) A200G-2, (c) A200G-3, (d) A200G-4, and (e) A200G-5	112
Figure 4C-14: Maximum Principal Strain Contour Map at Peak Load on Web Face for Prisms: (a) B200G-1, (b) B200G-2, (c) B200G-3, (d) B200G-4, and (e) B200G-5	112
Figure 4C-15: Maximum Principal Strain Contour Map at Peak Load on Web Face for Prisms: (a) C200G-1, (b) C200G-2, (c) C200G-3, (d) C200G-4, and (e) C200G-5	112
Figure 4C-16: Axial Stress versus Principal Strain Plot for Prisms: (a) A150H-1, (b) A150H-2, (c) A150H-3, (d) A150H-4, and (e) A150H-5	114
Figure 4C-17: Axial Stress versus Principal Strain Plot for Prisms: (a) B150H-1, (b) B150H-2, (c) B150H-3, (d) B150H-4, and (e) B150H-5	115
Figure 4C-18: Axial Stress versus Principal Strain Plot for Prisms: (a) C150H-1, (b) C150H-2, (c) C150H-3, (d) C150H-4, and (e) C150H-5	116
Figure 4C-19: Axial Stress versus Principal Strain Plot for Prisms: (a) A200H-1, (b) A200H-2, (c) A200H-3, (d) A200H-4, and (e) A200H-5	117
Figure 4C-20: Axial Stress versus Principal Strain Plot for Prisms: (a) B200H-1, (b) B200H-2, (c) B200H-3, (d) B200H-4, and (e) B200H-5	118

Figure 4C-21: Axial Stress versus Principal Strain Plot for Prisms: (a) C200H-1, (b) C200H-2, (c) C200H-3, (d) C200H-4, and (e) C200H-5	119
Figure 4C-22: Axial Stress versus Principal Strain Plot for Prisms: (a) A300H-1, (b) A300H-2, (c) A300H-3, (d) A300H-4, and (e) A300H-5	120
Figure 4C-23: Axial Stress versus Principal Strain Plot for Prisms: (a) B300H-1, (b) B300H-2, (c) B300H-3, (d) B300H-4, and (e) B300H-5	121
Figure 4C-24: Axial Stress versus Principal Strain Plot for Prisms: (a) C300H-1, (b) C300H-2, (c) C300H-3, (d) C300H-4, and (e) C300H-5	122
Figure 4C-25: Axial Stress versus Principal Strain Plot for Prisms: (a) A150G-1, (b) A150G-2, (c) A150G-3, and (d) A150G-4.....	123
Figure 4C-26: Axial Stress versus Principal Strain Plot for Prisms: (a) B150G-1, (b) B150G-2, (c) B150G-3, (d) B150G-4, and (e) B150G-5	124
Figure 4C-27: Axial Stress versus Principal Strain Plot for Prisms: (a) C150G-1, (b) C150G-2, (c) C150G-3, (d) C150G-4, and (e) C150G-5	125
Figure 4C-28: Axial Stress versus Principal Strain Plot for Prisms: (a) A200G-1, (b) A200G-2, (c) A200G-3, (d) A200G-4, and (e) A200G-5	126
Figure 4C-29: Axial Stress versus Principal Strain Plot for Prisms: (a) B200G-1, (b) B200G-2, (c) B200G-3, (d) B200G-4, and (e) B200G-5	127
Figure 4C-30: Axial Stress versus Principal Strain Plot for Prisms: (a) C200G-1, (b) C200G-2, (c) C200G-3, (d) C200G-4, and (e) C200G-5	128
Figure 4D-1: Typical Width of the Web at the Top Surface for CMUs with: (a) Full-Height Webs, (b) 120 mm Tall Webs, and (c) 50 mm Tall Webs	129

LIST OF SYMBOLS

b_w	Web width
COV	Coefficient of variation
DOF	Degrees of freedom
\bar{f}_m	Mean masonry assemblage strength
\bar{f}_{mG}	Mean masonry assemblage strength for grouted prisms
\bar{f}_{mH}	Mean masonry assemblage strength for hollow prisms
f'_{block}	Specified compressive strength of masonry unit
f'_{m_CSA}	Minimum specified masonry compressive strength specified by CSA S304-14
f'_{m_expt}	Specified masonry compressive strength
h	Prism height
h_w	Web height
l	Prism length
n_G	Number of grouted prism replicates
n_H	Number of hollow prism replicates
P_{cr}	Cracking load
P_{max}	Maximum load
SD	Standard deviation
s_G	Standard deviation of masonry assemblage strength for grouted prisms

s_H	Standard deviation of masonry assemblage strength for hollow prisms
t	Prism thickness
$t_{min_{fs}}$	Minimum face shell thickness
t_{min_w}	Minimum web thickness
ε_{max}	Maximum principal strain
ε_{min}	Minimum principal strain
σ_t	Tensile strength
σ_{max}	Maximum principal stress
σ_{min}	Minimum principal stress

CHAPTER 1: INTRODUCTION

1.1 Background

Masonry has been used as a construction material since the beginning of human civilization for its durability and aesthetic reasons. Many masonry structures that were built centuries ago still stand to this day, with more being constructed for residential and commercial purposes. However, the structural use of masonry declined in the last century due to the slow development and implementation of rational design standards (Kaaki, 2013). Efforts are being made to make masonry construction more competitive and cost-efficient while ensuring a satisfactory level of performance. For example, the advancement in production technology in the last few decades has encouraged manufacturers to explore different ways to optimize the geometry of concrete masonry units (CMUs). Optimized CMUs can better meet the current market demands on energy efficiency and sustainable building requirements.

CSA A165.1-14 – *CSA Standard on Concrete Block Masonry Units* (CSA, 2014a) and ASTM C90-11 – *Standard Specification for Loadbearing Concrete Masonry Units* (ASTM, 2011) contain minimum requirements for concrete block masonry units used in Canada and the U.S., respectively. Although these two standards share many similarities that allow for cross-border harmonization in terms of masonry products, some differences also exist. The minimum geometric requirements of the webs in concrete masonry units (CMUs) were the same in both of the standards until 2011, when the provisions governing these requirements in the United States were revised with the publication of ASTM C90-11 (ASTM, 2011) to improve the thermal resistance of CMUs (Lang & Thompson, 2014). Figure 1.1 shows the typical geometric properties of webs: minimum thickness (t_{min_w}), height (h_w), and width (b_w), which may vary with CMU size. Webs in CMUs are generally flared at the top and slightly tapered towards the bottom for the ease of handling during construction. The current provisions for minimum geometric requirements of webs in CSA A165.1-14 (CSA, 2014a) include minimum and equivalent web thickness requirements that are identical to the pre-2011 U.S. requirements. These requirements for CMU web geometry were included in CSA A165.1-14 (CSA, 2014a) based on the best production practices available at that time but lack a rational basis.

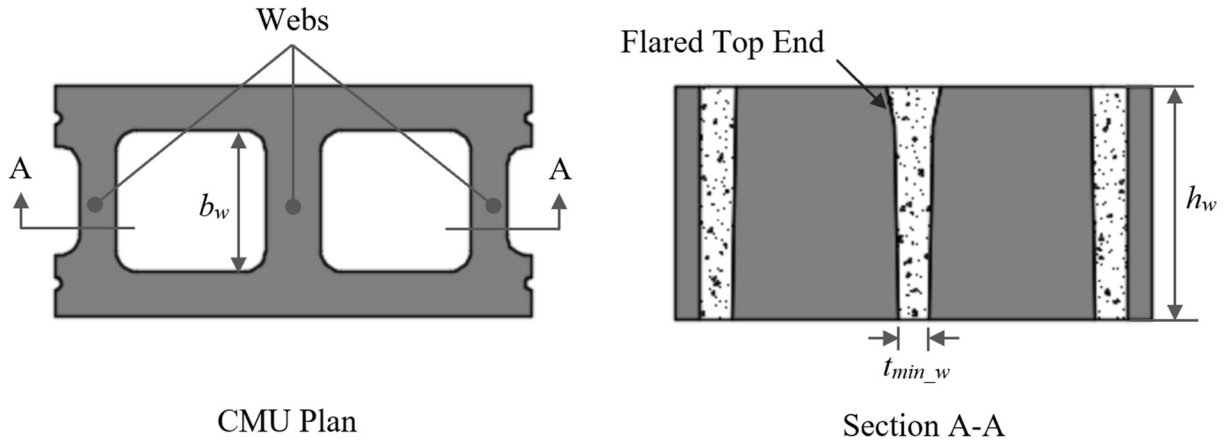


Figure 1.1: Typical Geometric Properties of Webs in CMU

The changing environment for building requirements, especially those related to energy efficiency and sustainability (Lang & Thompson, 2014), provide motivation for a re-evaluation of CMU web geometry in Canada. There are no current provisions in CSA A165.1-14 (CSA, 2014a) that allow for a reduced height of webs or that specify the required number of webs in CMUs. The lack of such provisions limits the range of web geometries in CMUs as used in Canada, thereby making it difficult to optimize them. In contrast, the provisions in ASTM C90-11 (ASTM, 2011) include a minimum normalized web area requirement of $45,140 \text{ mm}^2/\text{m}^2$, a measure of the web area in contact with the face shells per square meter of face shell, which indirectly governs the minimum height and number of webs in CMUs. This minimum normalized web area requirement allows CMUs to have webs with varying heights, thicknesses, and numbers including, but not limited to, CMUs with web heights that are shorter than 120 mm as used for typical Canadian knock-out web units. This flexibility in CMU web geometry provides manufacturers, designers, and contractors in the U.S. with the means to adjust CMU configurations to meet the current market demands related to sustainable building requirements (Lang & Thompson, 2014). This difference in minimum geometric requirements of the webs results in differences in masonry products between the U.S. and Canada, thereby affecting the cross-border trade and holding back potential synergies and cost savings.

The Canadian masonry construction industry may benefit if they could adopt the geometric requirements for webs as included in ASTM C90-11 (ASTM, 2011). This will help to reconcile the masonry industries within the two countries and also result in several other benefits such as

reduced material use resulting in lower unit weight, reduced mason fatigue, and reduced potential for injuries (Anton et al. 2005, Hoozemans et al. 2008, Faber et al. 2009). At the same time, any such changes to the CMU web geometry will potentially impact the structural performance of masonry members as webs are primarily responsible for the transfer of shear stress between the face shells in CMUs. A review of the available literature, however, suggested that the impact of such changes to the web geometry of CMUs on the structural performance of masonry assemblages has not been experimentally investigated.

An experimental investigation was therefore initiated at the University of Saskatchewan to evaluate the impact of web height of CMUs on the resulting masonry assemblage strength and failure mode of prisms constructed and tested in accordance with CSA S304-14 (CSA, 2014b). The viability of using CMUs with different web heights in masonry construction was evaluated based on the limited results from this study in an effort to optimize the CMU web geometry.

1.2 Research Objectives

The principal objective of this research program is the qualitative and quantitative comparison of the effect that web height of CMUs has on the assemblage strength and failure modes of prisms.

The following are the specific objectives of this experimental investigation:

1. To evaluate the impact of CMU web height on the resulting masonry assemblage strength of both hollow and grouted prisms;
2. To determine using statistical means if prisms constructed using CMUs conforming to ASTM C90-11 (ASTM, 2011) can achieve similar masonry assemblage strength as that of prisms constructed using CMUs conforming to CSA A165.1-14 (CSA, 2014a);
3. To evaluate the impact of CMU web height on the resulting failure mode of both hollow and grouted prisms; and
4. To compare the failure modes of prisms as predicted using analytical means to those obtained experimentally.

1.3 Methodology and Scope

A total of 126 prisms were constructed and tested to address the previously stated objectives. Seven replicates within each test series were included to identify statistically significant differences in

masonry assemblage strength between any two prism test series at a minimum 95% confidence level. Three CMU configurations consisting of two different knock-out web heights and full-height webs of the same web thickness were considered. Three CMU sizes for each configuration were also investigated. Both hollow and grouted prisms were included. The experimental program was divided into two phases due to space limitations in the laboratory. All prisms were constructed by an experienced mason. An effort was made to keep the properties of each material used in prism construction as consistent as practically possible between the construction phases, as well as between individual batches within each phase. Companion specimens were cast and tested together with masonry prisms to establish the properties of individual materials used in prism construction. Masonry prisms were tested under concentric axial compression using actuators that were operated in load control in accordance with CSA S304-14 (CSA, 2014b). A statistical analysis of the resulting masonry assemblage strengths was conducted across different test series of prisms to evaluate the impact of CMU web height on the masonry assemblage strength. A non-contact optical technique known as Digital Image Correlation (DIC) was used to obtain the full-field surface deformation results of prisms subjected to loading. Crack patterns and stress versus strain relationships for various test series were then evaluated using the DIC system results to assess the impact of CMU web height on the resulting failure mode of masonry prisms. Finite element modeling of selected prism geometries was also conducted to predict their failure mode and validate the results obtained from the DIC system. The viability of using CMUs with different web heights in both hollow and grouted masonry construction in Canada was then assessed.

1.4 Thesis Outline

Chapter 1 – A brief background of CMU web geometries and the need for further investigation of shorter web heights in CMUs were included in this chapter. The objectives of this study were stated, and the methodology used to address the stated objectives was then discussed.

Chapter 2 – A review of relevant code provisions related to the minimum geometric requirements of the webs in CMUs is provided in this chapter, followed by a discussion of the basic mechanics of load transfer in hollow and grouted masonry. The results from relevant previous investigations related to the impact of various parameters on the resulting masonry assemblage strength and failure modes of prisms are then summarized.

Chapter 3 – The experimental program that was designed to achieve the objective of this investigation is presented in this chapter. An outline of the construction and testing procedures for all specimens is also included.

Chapter 4 – The test results from the masonry prisms and associated companion specimens are presented in this chapter. The resulting masonry assemblage strength of prisms constructed using CMUs of the same size, but with different web heights are compared. Strain contour maps and stress versus strain plots generated from the DIC system results are presented and compared for different prism test series. A finite element model was then developed to compare the predicted failure mode of the selected prisms to those evaluated using the DIC system results. A discussion of the practical implications derived from the experimental results follows.

Chapter 5 – A summary of the experimental results, followed by the conclusions as related to the stated objectives are presented. Recommendations for future research are also provided.

CHAPTER 2: LITERATURE REVIEW

2.1 Introduction

Concrete masonry is a composite material that consists of concrete masonry units (CMUs), mortar, and, possibly, grout. Building components constructed using concrete masonry units are commonly subjected to axial compression that induces internal forces that must be resisted by the constituent materials. Mortar and grout are generally subjected to triaxial compression under such loading, whereas CMUs are under an axial compression and biaxial tension state. Constituent materials behave differently under similar loading conditions due to the differences in their mechanical properties. The results reported in past studies (Chahine, 1989; Hamid et al., 1985; Wong & Drysdale, 1985) have shown that the failure in both ungrouted and grouted concrete block masonry assemblages is primarily due to the tensile splitting of the webs in CMUs.

The code provisions for the minimum geometric requirements for the webs of CMUs as used in Canada and the United States are prescribed by CSA A165.1-14 (CSA, 2014a) and ASTM C90-11 (ASTM, 2011), respectively. However, there are differences in the requirements between these two standards. This will potentially impact the behavior of concrete masonry assemblages subjected to axial compression and might therefore create differences in the resulting masonry assemblage strength and failure modes. Such disparities will result in differences in masonry products and design methods between the U.S and Canada. A better understanding of the impact of web geometry of CMUs on the structural performance of concrete masonry assemblages will therefore minimize the discrepancies in masonry construction between the two countries.

This chapter includes a comparison of the minimum geometric requirements for the webs of CMUs as specified in CSA A165.1-14 (CSA, 2014a) and ASTM C90-11 (ASTM, 2011), introduces the mechanics of load transfer in both ungrouted and grouted concrete masonry assemblages subjected to concentric axial compression, and summarizes the results from the available literature that forms the basis of the current study.

2.2 Comparison Between CSA A165.1 and ASTM C90 in Terms of Minimum Geometric Requirements for the Webs in Hollow CMUs

Table 2.1 shows the minimum geometric requirements for the webs of hollow CMUs as included in CSA A165.1-14 (CSA, 2014a) and ASTM C90-11 (ASTM, 2011). These requirements have remained unchanged in CSA A165.1-14 (CSA, 2014a) over last six decades, whereas they were revised in 2011 for ASTM C90-11 (ASTM, 2011). The current provisions in CSA A165.1-14 (CSA, 2014a) stipulate the CMU web geometry by minimum web thickness that varies non-linearly with the CMU size (similar to pre-2011 U.S. requirements). There are no provisions that allow for a reduced web height or that specify the required number of webs in CMUs, thus allowing only a limited range of web geometries for CMUs used in Canada. In contrast, the provisions in ASTM C90-11 (ASTM, 2011) replaced the pre-2011 minimum web thickness requirement with a single minimum web thickness of 19 mm, regardless of CMU size. The requirement for the minimum equivalent web thickness, a sum of individual web thicknesses per meter of block length, was also replaced with a minimum normalized web area, a measure of the web area in contact with the face shells per square meter of face shell, of 45,140 mm²/m², irrespective of CMU size.

Table 2.1: Minimum Geometric Requirements for the Webs in Hollow CMUs as Specified in CSA A165.1 and ASTM C90

Nominal CMU Size (mm)	CSA A165.1 Web Thickness (mm)	ASTM C90			
		Prior to 2011		Current	
		Web Thickness (mm)	Equivalent Web Thickness (mm/linear m)	Web Thickness (mm)	Normalized Web Area (mm ² /m ²)
75	-	19	136		
100	26				
150	26	25	188	19	45,140
200					
250	28				
300	32	29	209		

The inclusion of a minimum normalized web area requirement in ASTM C90-11 (ASTM, 2011) allows for CMUs with a wide range of web geometries, including, but not limited to, CMUs with web heights that are shorter than typically used for Canadian knock-out web units for the same web thickness. Figure 2.1 shows a few examples of web geometry of typical 200 mm CMUs (both

top and sectional view) that meet the minimum web requirements as included in ASTM C90-11 (ASTM, 2011). Figure 2.1 (a) shows the standard stretcher unit with three full-height webs, whereas Figures 2.1 (b) and (c) show A and H-shaped units with two full-height webs and a single full-height web, respectively. Similarly, Figures 2.1 (d) and (e) show CMUs with different knock-out web configurations, as labeled. A greater array of CMU web geometries provides CMU producers, designers, and contractors in the U.S. with the means to reduce unit weight and also to adjust unit configurations to meet specific project needs (Lang & Thompson, 2014). In contrast, CSA A165.1-14 (CSA, 2014a) specifies a fixed type of web geometry in CMUs that is identical to the one in Figure 2.1 (a), except for the minimum web thickness that varies with CMU size.

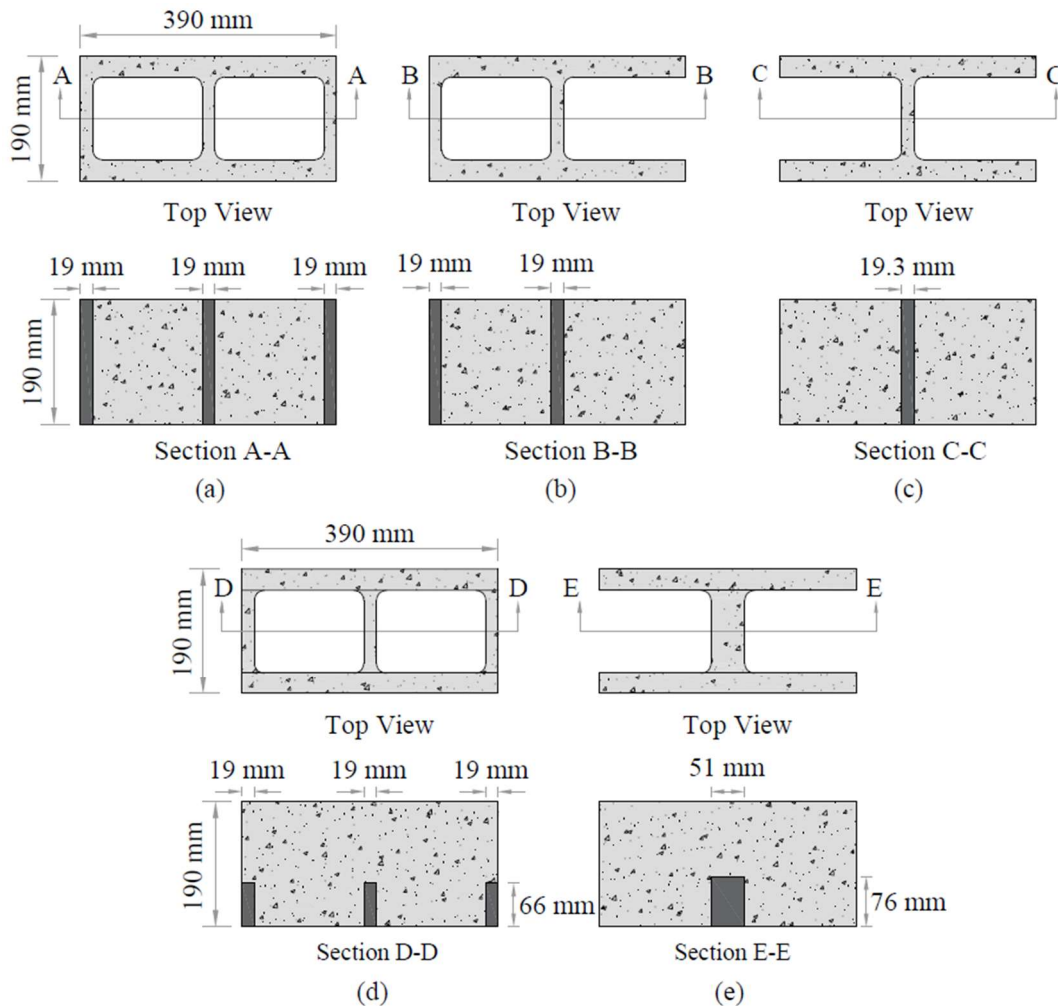


Figure 2.1: Cross-Sections of Acceptable Web Geometries Allowed in ASTM C90: (a) Standard Stretcher Unit, (b) A-Shaped Unit, (c) H-Shaped Unit, (d) Knock-Out Three Webs Unit, and (e) Knock-Out Single Web Unit

Lang and Thompson (2014) conducted a preliminary study related to the changes in minimum geometric requirements of webs as included in the 2011 edition of ASTM C90-11 (ASTM, 2011). This study included a review of the rationale behind adopting such changes. The authors used two simple design examples to illustrate that the minimum required equivalent web thickness in historical (pre-2011) versions of ASTM C90 provided greater web area than is typically needed in the design. The authors used another design example to calculate the minimum required web area to resist extreme loading conditions. A concrete masonry unit with nominal dimensions of 200 mm wide by 200 mm high and 400 mm long only required one full-height web measuring approximately 19 mm in thickness. This requirement is now expressed more generically as the normalized web area. The authors reported that many other design examples including varying unit sizes, reinforcement and grouting, design strength, and loading conditions, were considered while reviewing the potential inclusion of such changes in ASTM C90-11 (ASTM, 2011). In these cases, the results reported by the authors regarding the minimum area of web necessary for structural purposes were validated. The authors also reported that these changes helped to improve the properties of CMUs and result in several benefits such as reduced material use resulting in lower unit weight, reduced mason fatigue, and reduced potential for injuries. The authors also found that the reduction in web area connecting the face shells increases the thermal resistance property of concrete masonry assemblages. Although a critical review of minimum geometric requirements of webs was performed considering several aspects of masonry construction, the primary reason for considering such changes in ASTM C90-11 (ASTM, 2011) was to increase the thermal resistance of masonry assemblages (Lang and Thompson, 2014). The authors reported that this will help to meet the changing energy efficiency requirements for building systems in the U.S.

Despite having considerable advantages, the impact of changes to minimum geometric requirements of webs in CMUs as included in ASTM C90-11 (ASTM, 2011) on structural aspects of the masonry construction industry needs to be experimentally evaluated. A literature review revealed that no research has been conducted as of yet to investigate the impact of such changes on the resulting masonry assemblage strength, which is a primary characteristic of masonry. Additional experimental investigations are therefore warranted to help better understand the impact of such changes on the resulting masonry assemblage strength. The following section will

discuss the mechanics of load transfer in both ungrouted and grouted concrete masonry assemblages loaded under concentric axial compression.

2.3 Mechanics of Load Transfer in Concrete Masonry Assemblages Subjected to Axial Compression

Several researchers (Chahine, 1989; Hamid et al., 1985; Wong & Drysdale, 1985) have reported that the tensile splitting of the webs is the predominant mode of failure in concrete masonry assemblages subjected to axial compression. It is therefore necessary to understand the mechanics of load transfer to illustrate the significance of webs as are present in concrete masonry units (CMUs). Figure 2.2 shows the load resisting mechanism of both ungrouted and grouted masonry assemblages which are at least three courses tall, constructed in a running bond with face-shell mortar bedding, and subjected to concentric axial load. The CMUs within the intermediate course was selected for the illustration purpose as they are confined by mortar bedding at both top and bottom and are not directly subjected to end platen restraint.

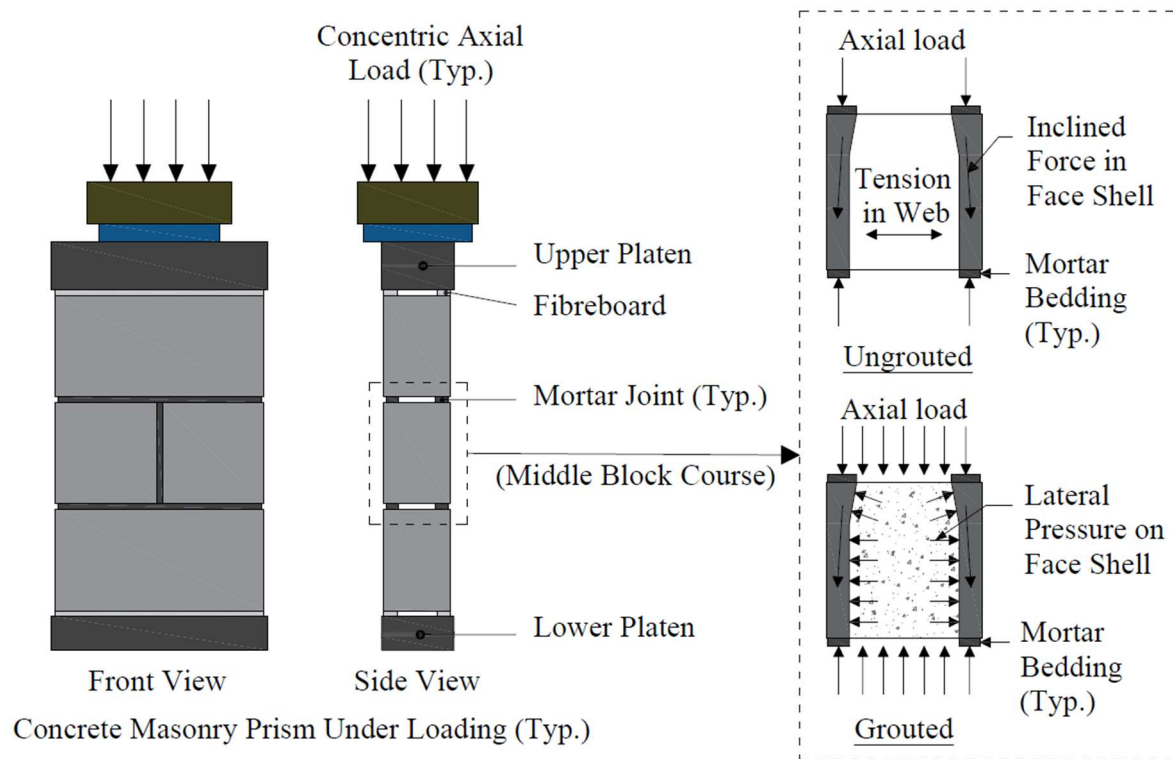


Figure 2.2: Mechanics of Load Transfer in UngROUTED and Grouted Concrete Masonry Assemblages

The concentrically applied axial load in ungrouted prisms is transferred as an inclined load into the face shell for two different reasons. First, a part of concentrically applied axial load causes lateral expansion of mortar (given that it is softer than the CMU) in both in-plane directions that induces horizontal tensile forces at the top and bottom of face shells throughout the length. The resultant of this horizontal tensile force and axially applied vertical force results in an inclined load within the face shells. Second, the CMU geometry includes a flange at the top of face shells that causes the transfer of externally applied axial load at a very acute angle of inclination into the face shells (Figure 2.2). The horizontal component of these inclined forces creates lateral tension on face shells along the prism width. This tensile force is resisted by the webs that connect two face shells. In the case of a grouted masonry assemblage, lateral expansion of the grout under the concentric axial load adds to the tension in the webs (over the previously described tensile force) of CMUs. This is due to the tendency of grout to expand more under axial loading than the CMU itself because of the differences in their elastic properties. The tension induced in webs of CMUs in both ungrouted and grouted masonry assemblages ultimately cause their vertical splitting as concrete masonry units are weak in tension. Therefore, tensile splitting of the web primarily governs the failure in concrete block masonry and is a critical parameter when evaluating the masonry assemblage strength (Chahine, 1989; Hamid et al., 1985; Köksal et al., 2005; Wong & Drysdale, 1985).

2.4 Influential Parameters on Masonry Assemblage Strength

All parameters considered in the current experimental design are included in this review to highlight their importance and potential impact. These are: CMU size, CMU web geometry, presence of grout, and height-to-thickness (h/t) ratio. The following sub-sections outline the impact of these parameters on the masonry assemblage strength, as obtained from prism testing, based on a review of available literature.

2.4.1 CMU Size

CMUs of various sizes are used in masonry construction to meet the design requirements, with 200 mm CMUs being the most commonly used. As explained in Section 2.3, the failure of concrete masonry primarily occurs due to tensile splitting of the webs. The CMU web thickness, however, does not vary linearly with the CMU size (for CMUs governed by both the U.S. and Canadian

standards and shown in Table 2.1) and so the effect of any changes to the web geometry on masonry assemblage strength needs to be evaluated across all CMU sizes. The majority of compression test data as reported in the available literature resulted from prisms constructed using 200 mm CMUs and the impact of using CMUs of various sizes has rarely been examined (Chahine, 1989).

Hamid and Chukwunenye (1986) conducted an analytical investigation using three-dimensional finite element modeling to study the effect of block size on the resulting assemblage strength of axially loaded masonry prisms. Three-course tall hollow prisms constructed in stack pattern using 200, 250, and 300 mm CMUs with otherwise similar material properties were modeled. The authors reported that no appreciable difference in either the magnitude or the distribution of stresses existed due to different block sizes. It was therefore concluded that the block size did not influence the resulting masonry assemblage strength.

Chahine (1989) studied the behavior of face shell mortared concrete block masonry subjected to axial compression. The evaluation of the effect of CMU sizes on the resulting masonry assemblage strength was one of the objectives of this study. A total of 50 four-course tall masonry prisms were constructed with face shell mortar bedding using five different CMU sizes (i.e., all sizes within 100 – 300 mm) and were tested under concentric axial load. Test results as reported by the authors were normalized in terms of the unit compressive strength so that they could be readily compared. However, the author did not consider the influence of prism aspect ratio (h/t) resulting due to different sizes of CMUs used for prism construction. The ratio of masonry assemblage strength to unit compressive strength decreased with increasing CMU size except for prisms constructed using 300 mm CMUs which exhibited a higher strength. This was attributed to the dominant effect of end platen restraint in prisms constructed using 300 mm CMUs that induced artificial high strength in prisms, presumably due to the smaller h/t ratio.

Only limited research has been conducted to investigate the effect of block size on the resulting masonry assemblage strength. While 200 mm CMUs are commonly used in masonry construction, 250 and 300 mm standard stretcher units are also used when larger cores for grouting and reinforcement are needed to obtain higher compression capacity. Further research is therefore warranted to provide additional insights regarding the influence of block size.

2.4.2 CMU Web Geometry

The most commonly used units in masonry construction are standard stretcher units. Nonetheless, other unit types such as knock-out units, lintel units, and open-end units are also used depending on the nature of construction (Duncan, 2008). Since the failure of concrete masonry assemblage is mainly due to the appearance of vertical cracks on the webs as explained in Section 2.3, the influence of any changes to the geometry of the webs on the resulting masonry assemblage strength needs to be examined.

Boult (1979) constructed and tested a total of 112 grouted prisms, of which the test results from 24 prisms were used to investigate the effect of CMU web thickness on the resulting masonry assemblage strength. Standard flat-ended 200 mm CMUs with two different web thicknesses (25 and 40 mm) were considered. It was found that the CMUs with a web thickness of 25 mm or greater have negligible influence on the resulting masonry assemblage strength. This was potentially due to the grout fulfilling the structural role of the webs.

Ganesan and Ramamurthy (1992) developed a finite element model to investigate the effect of CMU web geometry on masonry assemblage strength of 3-course tall hollow prisms subjected to axial load. Eight-node isoparametric solid elements were used for modeling the hollow masonry prisms and a linear elastic analysis approach was used. Figure 2.3 shows that flat-ended CMUs with two different web geometries: (a) all three webs of equal thickness (i.e., 40 mm) and (b) a thicker middle web of 70 mm with 30 mm thick end webs, were considered. The prisms constructed in running bond using CMUs with equal web thicknesses resulted in noticeably lower masonry assemblage strength as compared to those constructed using CMUs with a thicker middle web. This was attributed to very high lateral stresses in the webs due to the deep beam action resulting from the incomplete overlapping of the webs as shown in Figure 2.3 (a) (Ganesan & Ramamurthy, 1992). However, Figure 2.3 (b) shows that webs were fully aligned in prisms constructed using CMUs with a thicker middle web and thus allowed for the use of full mortar bedding. This eliminated stress concentrations in the webs and resulted in a higher masonry assemblage strength (Ganesan & Ramamurthy, 1992). The authors therefore concluded that the use of CMUs with different geometries (i.e., interior versus exterior) but of same strength can result in different assemblage strengths. Consideration for the effect of unit web geometry while

calculating masonry strength using the unit strength approach, as specified in relevant standards, was therefore recommended.

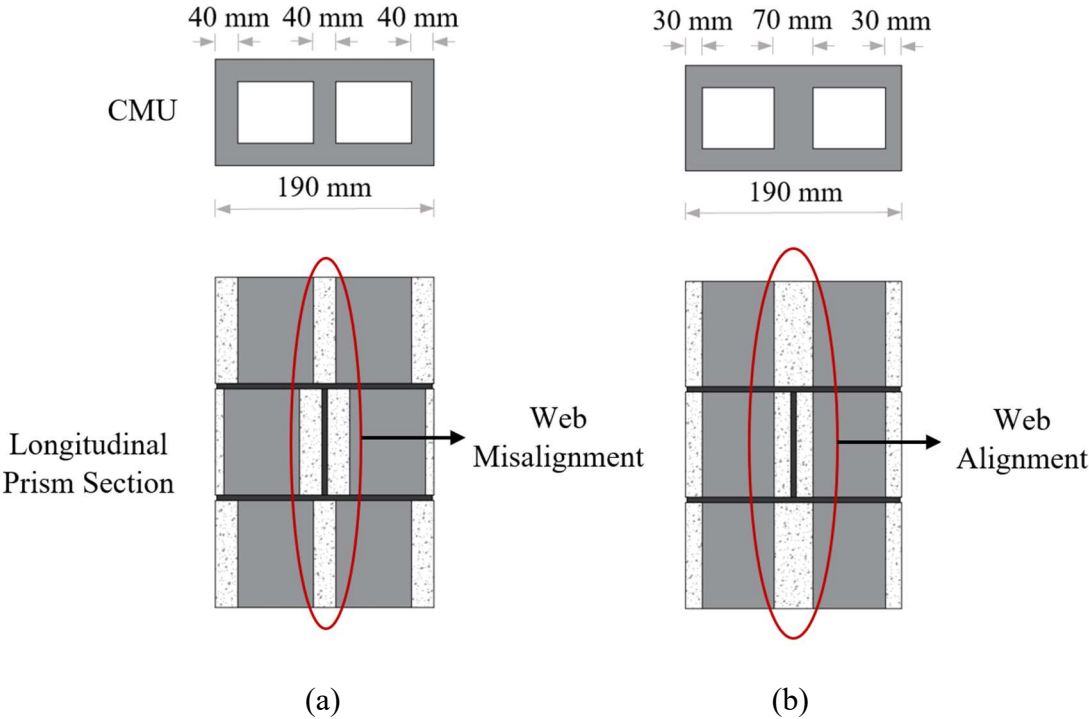


Figure 2.3: Sectional View of Webs in Successive Courses for Ganesan and Ramamurthy’s 1992 Investigation: (a) Misaligned, and (b) Aligned

A limited number of investigations are available that investigated the impact of the web geometry on the resulting masonry assemblage strength. A review of the available literature did not, however, reveal the existence of work exclusively related to the impact of CMU web height. Additional research is therefore warranted to achieve a better understanding of its influence.

2.4.3 Presence of Grout

Masonry walls are generally partially grouted and reinforced. The compressive strength of the grouted assemblage is lower than that of a corresponding ungrouted hollow assemblage due to the additional lateral pressure exerted by the grout on the blocks (as explained in Section 2.3). Several researchers have therefore investigated the effect of the presence of grout on the resulting masonry assemblage strength.

Drysdale & Hamid (1979) conducted an experimental study that focused, in part, on the effect of grouting and grout strength on the resulting masonry assemblage strength. A total of 73 three-course tall prisms were constructed and tested for this purpose. Test results of grouted and ungrouted prisms constructed using mortar of similar strength were compared. The grout, occupying 40% of the gross area of the prisms, did not contribute proportionally to the resulting masonry assemblage strength. This was attributed to the additional lateral pressure exerted by the grout onto the CMU, as previously explained. Test results of 5 grouted prism groups, each constructed using grout of different strength, were compared. Drysdale & Hamid (1979) reported that even a large increase of 172 % in grout strength resulted only in a relatively small increase of 26 % in the resulting masonry assemblage strength of the grouted prisms. The authors therefore suggested matching the deformation characteristics of the grout and block rather than increasing the grout strength to obtain higher resulting masonry assemblage strength for the grouted prisms.

Chahine (1989) also included the effect of grout in the resulting masonry assemblage strength and compared test results between ungrouted, grouted, and solid block masonry prisms. For this purpose, a total of 28 four-course tall prisms constructed using 200 mm standard stretcher units with face shell mortar bedding were subjected to concentric axial loading. The masonry assemblage strength of grouted prisms was 30 to 35% less than those of ungrouted prisms. Similarly, test results as reported by Chahine (1989) showed that the masonry assemblage strength of grouted prisms was 29% less than those prisms constructed using 100% solid CMUs. The author also reported different masonry assemblage strengths for two grouted prism groups constructed using the same grout but with CMUs of different strengths. Chahine (1989) suggested that the resulting masonry assemblage strength of grouted prisms mainly depended on the tensile strength of CMUs rather than the grout strength.

Khalaf (1996) constructed and tested a total of 60 full-block wide and 30 half-block wide prisms to investigate the effect of grout strength, mortar types, height-to-thickness (h/t) ratio, length-to-thickness (l/t) ratio, and mortar joint thickness on the resulting masonry assemblage strength. Prisms were filled with grout of three different strengths: (a) low-strength (1:5:2), medium-strength (1:3:2), and high-strength (1:1:2), to investigate its impact on the resulting masonry assemblage strength. The resulting masonry assemblage strength of half-block wide grouted prisms increased in proportion with increasing grout strength. This trend was observed until the

grout strength reached approximately 45.0 MPa (i.e., 1:1:2), at which point the masonry assemblage strength of grouted prisms approached that of corresponding ungrouted prisms (Khalaf, 1996). However, the authors did not find any considerable change in the resulting masonry assemblage strength of full-block wide grouted prisms for the included range of grout strengths. It was therefore concluded that matching the deformation characteristics of both the grout and CMUs is more influential than increasing the grout strength. This finding agrees with conclusions made by Drysdale and Hamid (1979).

The results reported in literature show good agreement and reported that the use of grout reduces the resulting masonry assemblage strength (Chahine, 1989; Drysdale & Hamid, 1979; Khalaf, 1996). It was also found that the masonry assemblage strength is not proportional to absolute grout strength; therefore, matching the strength of the grout to that of CMU is more effective than using grout with a substantially higher compressive strength than that of the CMUs (Drysdale & Hamid, 1979; Khalaf, 1996).

2.4.4 Height-to-Thickness (h/t) Ratio

Figure 2.4 shows typical dimensions of a three course tall (h), one unit long (l), and one unit wide (t) concrete masonry prism constructed in a running bond with face shell mortar bedding. Concrete masonry prisms of various heights and widths are generally tested in the laboratory to obtain the resulting masonry assemblage strength. The height of the prism can be varied by varying the CMU courses, while its width varies with varying CMU size. The ratio of a prism's height to its width, represented as h/t ratio, is often used in masonry research to quantify its aspect ratio. Prisms with varying h/t ratios are tested in the laboratory with steel bearing plates at the top and bottom. These bearing plates introduce lateral restraints at both ends that cause an apparent increase in the masonry assemblage strength. This effect is more pronounced in shorter prisms and diminishes as the height of the prism increases (Boult, 1979; Fahmy & Ghoneim, 1995). Numerous researchers have therefore studied the effect of h/t ratio on the resulting masonry assemblage strength. Results, in terms of correction factors, are included in the relevant standards used in the U.S. and Canada.

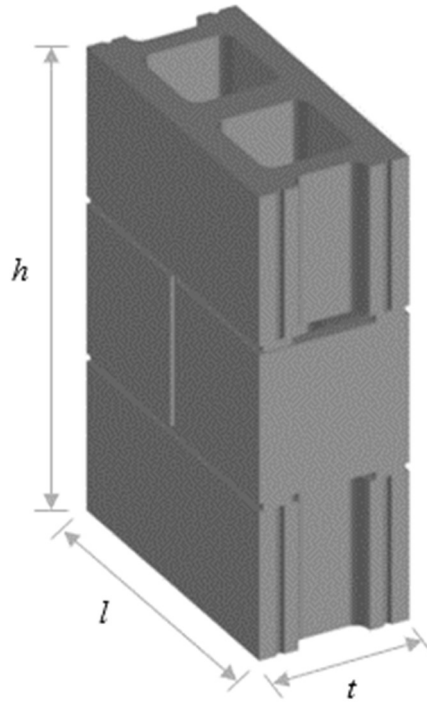


Figure 2.4: Prism Dimensions

The Canadian standard for masonry design, CSA S304-14 (CSA, 2014b), specifies correction factors to take into account the effect of end platen restraint on the resulting masonry assemblage strength and compare the strength of shorter prisms ($h/t < 5$) to that of full-scale masonry walls. Table 2.2 shows the correction factors for various h/t ratios for hollow concrete masonry prisms as included in CSA S304-14 (CSA, 2014b). The correction factor for grouted prisms, irrespective of their h/t ratio, is taken as unity. This is because the continuity provided by the grouted cores reduces the effect of end platen restraint (Fahmy & Ghoneim, 1995). The actual masonry assemblage strength is calculated by multiplying the assemblage strength of the prism as obtained from prism testing with a correction factor for a specific h/t ratio as listed in Table 2.2. These correction factors were established based on historical test results (Chahine, 1989; Fahmy & Ghoneim, 1995; Hamid et al., 1985; Hamid & Chukwunenye, 1986; Maurenbrecher, 1980; Wong & Drysdale, 1985).

Table 2.2: Correction Factors Provided in CSA S304-14

Height-to-Thickness Ratio*	Correction Factor
2	0.85
3	0.90
4	0.95
5 to 10	1.00

*Linear interpolation may be used.

Boult (1979) investigated the mechanism of strength reduction with increasing prism height to determine the minimum specimen size that can accurately represent the masonry assemblage strength as would be measured in a full-scale masonry wall. Experimental results from 112 grouted prisms of varying height constructed using 7 different CMU types were included in this study, of which results from 92 prisms were used to achieve these objectives. Test results showed that masonry assemblage strength for grouted prisms decreased with increasing prism height. However, the strength reduction with height was negligible between 5 and 12 courses. The author therefore reported that a 5-course tall prism represented the strength behavior of a full-scale masonry wall. No noticeable difference in masonry assemblage strength for 3 to 5-course tall grouted prisms was identified. The end platen restraint had a considerable effect on prisms with an h/t ratio of two but had a little effect on prisms with h/t ratio greater than two (Boult, 1979). It was concluded that three course-tall prisms should be used as a minimum specimen size for prism testing.

Fahmy & Ghoneim (1995) conducted three-dimensional non-linear finite element modeling (FEM) investigation that included an evaluation of the effect of h/t ratio on the resulting masonry assemblage strength for both grouted and ungrouted prisms. The authors modeled both grouted and ungrouted prisms with a varying h/t ratio of 2 to 12 with each subjected to a concentric axial load. Results showed that the masonry assemblage strength decreased with increasing h/t ratio for both grouted and ungrouted prisms (Fahmy & Ghoneim, 1995). However, there was only a 2% difference in the resulting masonry assemblage strength for ungrouted prisms between 5 and 12-course tall. In contrast, masonry assemblage strength for a 12-courses tall grouted prism was reported to be 98% of that for a 3-course tall grouted prism. Continuity provided by the grouted cores reduced the effect of end platen restraint for the shorter prisms (Fahmy & Ghoneim, 1995).

A review of Khalaf's (1996) study presented in Section 2.4.3 shows that an evaluation of the effect of h/t ratio on the resulting masonry assemblage strength was also included in this study. Test results from 36 prisms, 18 each for full block wide and half block wide prisms, with varying h/t ratios of 2 to 6 were analyzed for this purpose. Both grouted and ungrouted prisms were included for each prism width. The resulting masonry assemblage strength for both grouted and ungrouted prisms decreased with increasing prism height, irrespective of the prism width. The influence of confinement stresses produced at the top and bottom of the prisms, as a result of the difference in stiffness between the concrete masonry prism and the steel platens, decreased with the increasing prism height (Khalaf, 1996). The author also conducted a comparative analysis of test results for three and six-course tall prisms and found that there was no noticeable difference in the resulting masonry assemblage strength between these two prism groups, irrespective of the presence of grout. It was therefore recommended to use three-course tall prisms as a standard size for prism testing (Khalaf, 1996).

A review of results reported in the available literature (Boult, 1979; Fahmy & Ghoneim, 1995; Khalaf, 1996) showed that the effect of end platen restraint decreased with the increasing h/t ratio, as did the resulting masonry assemblage strength. This effect was consistently observed for ungrouted prisms while grouted prisms were relatively less affected by h/t ratio due to the continuity provided by grout columns which reduced the effect of end platen restraint. Correction factors dependent on the h/t ratio, along with a single correction factor of 1, are therefore included in CSA S304-14 (CSA, 2014b) for hollow and grouted masonry assemblages, respectively.

The parameters discussed in Section 2.4 not only influence the resulting masonry assemblage strength of prisms but also affect their failure behavior. Section 2.6 will include a discussion of the literature that focused on the investigation of failure modes of concrete masonry assemblages subjected to a concentric axial loading. The following section discusses the minimum number of replicates needed to identify a statistically significant difference in test results between two prism groups at a minimum of 95% confidence level.

2.5 Statistical Parameters for Masonry Prism Replicates

Gayed & Korany (2011) conducted a study to re-establish the correlation between unit strength and prism strength. A test database was established for the masonry assemblage strength of 1376

hollow and 310 grouted prisms that were reported in the literature from 1978 to 2011 in North America. A similar study was conducted by Ross & Korany (2012) which focussed on grouted prisms and included 730 individual prism test results that were reported in the literature for the same time period as was included in the previous study. The majority of the prisms included in the database used in both studies were three-course tall and consisted of 3 to 5 replicates.

The database reported by Gayed & Korany (2011) and Ross & Korany (2012) included 402 and 327 individual hollow and grouted prisms, respectively, that were three-course tall, one-block wide, and constructed using standard 200 mm units. The only parameter that varied between these two prism groups was the presence of grout. The average masonry assemblage strength and associated coefficient of variation (*COV*) for hollow prisms were reported to be 15.3 MPa and 6.02%, respectively (Gayed & Korany, 2011), whereas the reported average masonry assemblage strength for grouted prisms was 14.2 MPa with a *COV* of 6.88% (Ross & Korany, 2012). These results can be considered as known parameters in the statistical analysis for the calculation of the required number of replicate prisms to identify significant difference in the compression test results between hollow and grouted prisms at a minimum of 95% confidence level.

2.6 Relevant Studies on Failure Modes of Concrete Masonry Assemblages

Masonry exhibits complex behavior as it is composed of two or more constituents with different mechanical properties. It is therefore necessary to understand its failure characteristics along with the resulting assemblage strength when subjected to a concentric axial loading. For this, different conventional point-to-point deformation measuring devices such as strain gauges, linear variable differential transducers (LVDT), and dial gauges can be installed onto the prisms before they are subjected to loading. Numerous research have been conducted to date to better understand the failure behavior of concrete masonry assemblages subjected to a concentric axial loading.

Wong and Drysdale (1985) constructed and tested a total of 34 concrete masonry prisms, of which test results from 24 prisms were used in investigating the failure modes for both hollow and grouted prisms. All prisms were constructed in running bond with face shell mortar bedding using 200 mm standard stretcher units and were subjected to a concentric axial loading. Both mechanical and electrical measuring instruments were used to record the strain readings during the tests. Observations made during testing revealed that hollow prisms always failed by initial splitting of

the webs followed by the instability and the collapse of face shells (Wong and Drysdale, 1985). Grouted prisms failed in a similar fashion, but the crack widths were limited due to the presence of the grout (Wong & Drysdale, 1985). The stress versus strain characteristics of ungrouted and grouted prisms varied markedly even though they were constructed using similar units. The authors therefore suggested treating these prisms separately during the design process.

Ramamurthy (1995) conducted an analytical investigation using finite element modeling to investigate the failure modes of grouted concrete masonry prisms subjected to concentric axial compression. Eight-node isoparametric solid elements were used to model the hollow concrete masonry units needed to construct three-course tall prisms in running bond with full mortar bedding. CMUs with a thicker middle web as used by Ganesan & Ramamurthy (1992) and described in Section 2.4.2 was used to ensure the complete alignment of webs in successive block courses. Stress distributions along different vertical sections of CMU, grout, and mortar were analyzed in detail (Ramamurthy, 1995). Higher axial stresses developed in the mortar on the outer face of the face shell than at the inner face where the strain in mortar is limited by the presence of the stronger grout. This caused the mortar to reach its unconfined compressive strength at relatively early stage of loading and resulted in high lateral stress in the outer face of the face shell (Ramamurthy, 1995). This was reported to have caused the early splitting failure; therefore, authors concluded that the superposition of strength is not valid in the case of grouted masonry prisms. The authors also concluded that the matching of block-mortar material properties is equally important as matching block-grout material properties to allow for grouted masonry prisms with higher assemblage strengths.

Mohamad et al. (2017) conducted an experimental investigation to evaluate the failure modes of hollow concrete masonry prisms constructed using three different mortar strengths. Eleven three-course tall prisms were constructed in stack bond using 150 mm CMUs and were tested under uniaxial compression with load being applied in 4 increments until failure occurred. Two LVDTs were placed on the outer face shell across the top mortar bed joint. Readings from these devices were used to calculate strains and eventually to plot stress versus strain. Prisms constructed using strong mortar mainly failed due to tensile splitting of the CMU, where constituents acted as a homogeneous material. In contrast, mortar crushing initiated the failure in prisms constructed with weak mortars, which eventually caused localized tensile stresses in the CMUs (Mohamad et al.,

2017). The results reported in this study showed that the mortar governed the failure of hollow concrete masonry assemblages. It was therefore recommended that a better way to account for the behavior of mortar in the failure of hollow concrete masonry assemblages was required.

A general agreement was found in the available literature related to the tensile splitting failure in hollow concrete masonry assemblages. However, a consensus has yet to be reached on failure modes of grouted concrete masonry assemblages as the complex interaction between three constituent materials, including the grout, is involved. Additional research is therefore warranted to provide a better understanding of failure behavior in concrete masonry assemblages.

2.7 Summary

This chapter included a review of relevant code provisions and the available literature regarding the influence of CMU web geometry, CMU size, presence of the grout, and height-to-thickness (h/t) ratio on the resulting assemblage strength and failure modes of masonry prisms. The failure of concrete masonry prisms was found to be primarily governed by a tensile splitting of the webs. As a result, any changes in their geometry potentially influence the structural performance of masonry assemblages. Other parameters such as CMU size, presence of grout, and h/t ratio were also found to be influential. A review of available literature revealed that research efforts have rarely been made to investigate the impact of web geometry of CMUs on the resulting masonry assemblage strength and failure modes. Additional research is therefore warranted to better understand its influence. An experimental program involving prism testing was therefore conducted at the University of Saskatchewan to evaluate the impact of CMU web height on the resulting assemblage strength and failure modes of masonry prisms. The following chapter describes the experimental program designed to achieve the objective of this study and outlines the construction and testing procedures for all specimens.

CHAPTER 3: EXPERIMENTAL DESIGN

3.1 Introduction

The differences between the minimum geometric requirements for the webs of CMUs as included in CSA A165.1-14 (CSA, 2014a) and ASTM C90-11 (ASTM, 2011) potentially impacts the resulting masonry assemblage strength which forms the basis of establishing the resistance of masonry elements. It is important to minimize such discrepancies in masonry construction practice between the U.S and Canada as it will affect the exchange of masonry products and research between the two countries. A review of the available literature revealed that no research efforts have been made to investigate the impact of web geometry of CMUs on the resulting masonry assemblage strength and failure modes of prisms. An experimental investigation based on prism testing was therefore conducted at the University of Saskatchewan with the aim of evaluating the impact of CMU web height on the resulting masonry assemblage strength and failure modes of masonry prisms.

The test matrix included in the experimental design is presented in this chapter followed by the description of construction materials used to construct the masonry prisms. The procedure for constructing masonry prisms in the laboratory is then discussed. This chapter also includes a discussion of the instrumentation of prisms for strain measurement as well as the test setup for masonry prisms and associated companion specimens.

3.2 Specimen Description and Test Matrix

All prisms included in this experimental investigation were three courses tall (h), one unit long (l), and one unit wide (t), and were constructed in running bond with face shell mortar bedding (as shown in Figure 2.4) that followed the requirements as prescribed in CSA S304-14 (CSA, 2014b). A full block was used as the top and bottom courses for all prisms to prevent a plane of weakness adjacent to the bearing plates used in the test setup. Two half blocks were used as the middle course with the cut ends facing outwards.

Figure 3.1 shows three different web heights for the CMUs that were included in the current experimental investigation: full-height webs (Figure 3.1 (a)), knock-out webs cut such that they were 120 mm tall (Figure 3.1 (b)), and knock-out webs cut such that they were 50 mm tall (Figure

3.1 (c)). The two types of knock-out unit geometries were produced by cutting out the equivalent top flared portion of the web, following the typical local construction practice, in the laboratory from full-height web units to ensure that all CMU types, for a given size, originated from a common batch and had similar material properties. CMUs with full-height webs, as shown in Figure 3.1 (a), represented CSA A165.1-14 (CSA 2014a) regular stretcher units. Canadian block suppliers typically limit the height of knock-out webs to about 120 mm so that CMUs with 120 mm tall webs, as shown in Figure 3.1 (b), represented CSA A165.1-14 (CSA 2014a) knock-out web units. Provisions for minimum normalized web area requirements as specified in ASTM C90-11 (ASTM 2011) allow CMUs with a wide range of web geometries. CMUs with knock-out webs cut such that they were 50 mm tall, as shown in Figure 3.1 (c), approached the minimum requirement of $45,140 \text{ mm}^2/\text{m}^2$ as included in ASTM C90-11 (ASTM 2011). This unit type therefore represents ASTM C90-11 (ASTM 2011) knock-out web units which conform to ASTM C90-11 (ASTM 2011) but are not yet certified for use by CSA A165-14 (CSA 2014a).

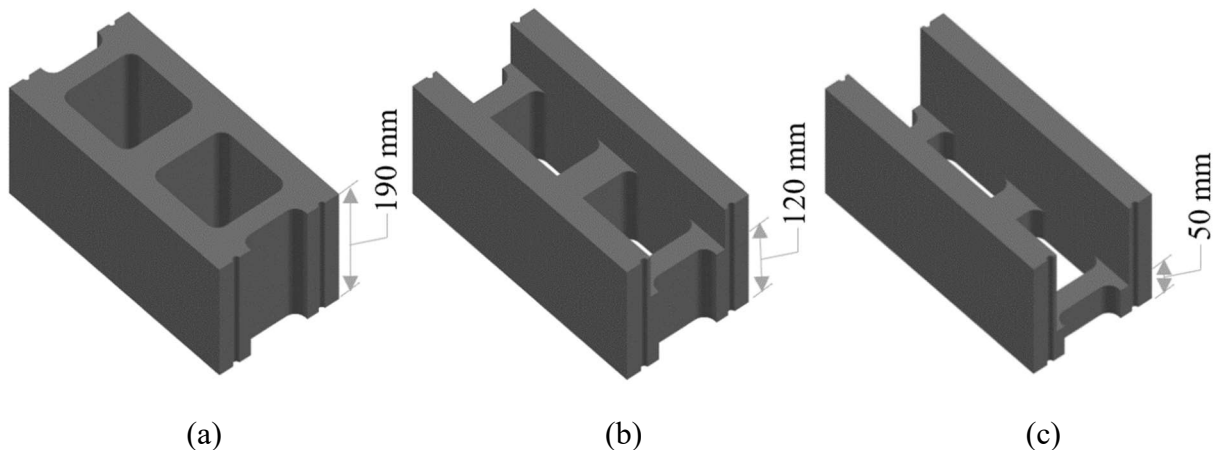
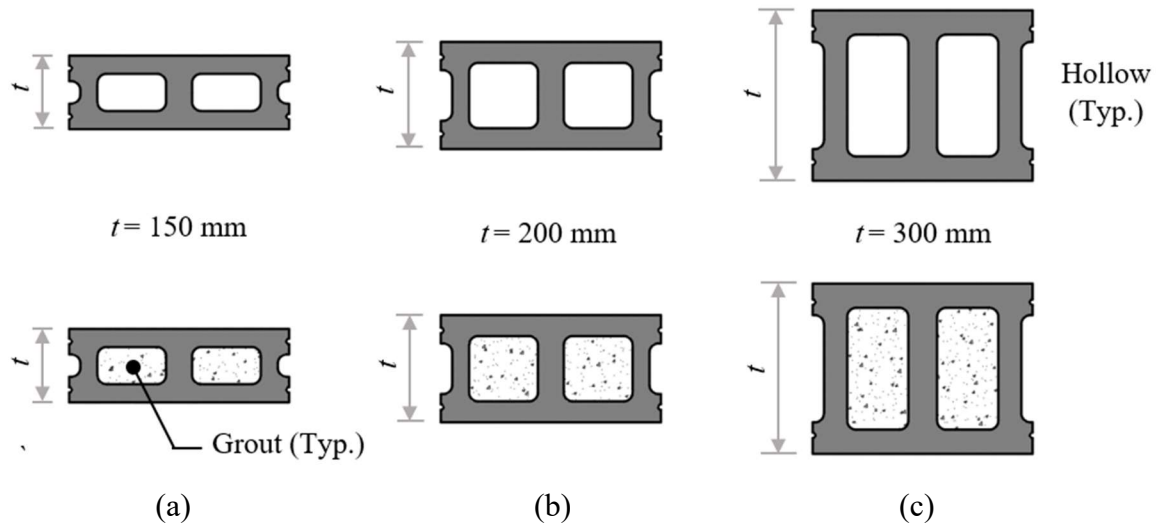


Figure 3.1: CMU Web Heights: (a) CSA A165.1 Regular Stretcher Unit, (b) CSA A165.1 Knock-Out Web Unit, and (c) ASTM C90 Knock-Out Web Unit

CMU web thickness does not vary proportionally with CMU size: three different CMU sizes (150 mm, 200 mm, and 300 mm) were therefore included in this experimental investigation to capture a wide range of web properties. Figure 3.2 shows the top view of typical prism configurations constructed using: 150 mm CMUs (Figure 3.2 (a)), 200 mm CMUs (Figure 3.2 (b)), and 300 mm CMUs (Figure 3.2 (c)). Prisms constructed using each CMU size included three unique configurations resulting from the use of three different web heights. Both hollow and grouted

prisms were included in the experimental program. It is to be noted that actual web thicknesses for the various block sizes are given in Figure 3.3.



Note: Knock-out web details, where applicable, are shown in Figure 3.1.

Figure 3.2: Top View of Prisms Constructed Using: (a) 150 mm CMUs, (b) 200 mm CMUs, and (c) 300 mm CMUs

The combinations of the investigated parameters, as discussed above, resulted in a total of 18 prism test series. Table 3.1 shows the overall test matrix included in this experimental investigation. Each test series was provided with a unique identification mark of the form X###Y in the first column of Table 3.1 to represent its important attributes, where X indicates the CMU type that resulted from different web heights (A – full-height, B – 120 mm tall, or C – 50 mm tall); ### represents the size of CMU used in prism construction (150, 200, or 300 mm); and Y indicates the grouting condition (H – Hollow, or G – Grouted). For example, A200G represents the test series that was constructed using 200 mm full-height web units (i.e., CSA A165.1 regular stretcher units) that were grouted. A total of seven replicates, as were found to be required in Appendix 3A, were included in each test series to identify a statistically significant differences in the masonry assemblage strength between any two test series of prisms at a minimum of 95% confidence level with a power of approximately 58%.

Table 3.1: Test Matrix

Test Series ID	CMU Type	Nominal CMU Size (mm)	Hollow/Grouted	
A150H	CSA A165.1 Regular Stretcher	150	Hollow	
A200H		200		
A300H		300		
A150G		150	Grouted	
A200G		200		
A300G		300		
B150H		CSA A165.1 Knock-Out	150	Hollow
B200H			200	
B300H			300	
B150G	150		Grouted	
B200G	200			
B300G	300			
C150H	ASTM C90 Knock-Out		150	Hollow
C200H			200	
C300H			300	
C150G		150	Grouted	
C200G		200		
C300G		300		

3.3 Construction Materials

Locally available materials meeting the requirements prescribed in relevant codes and standards were used to construct all prisms so that they represented local masonry construction practice. Aggregates, cement, and CMUs of each size were all procured from a single batch to ensure consistency in material properties. The following sections provide more details related to each of the construction materials.

3.3.1 Concrete Masonry Units

Three sizes (150, 200, and 300 mm) of normal weight regular stretcher concrete masonry units were supplied by Cindercrete Products Ltd. of Saskatoon. All CMUs were delivered in a single shipment on plastic-wrapped pallets and were stored in the Structures Laboratory for a minimum of two weeks prior to prism construction to equilibrate with laboratory humidity and temperature

conditions. Each pallet contained a combination of flat-ended and frog-ended CMUs, of which only the frog-ended CMUs were used for prism construction to maintain consistency in their resulting net surface area. Figure 3.3 shows the detailed dimensions and the cross-sections of CMUs of all sizes procured for this experimental investigation. CMUs are laid with flanged portion on top during the masonry construction; therefore, their elevations are drawn to represent the construction practice. Figure 3.3 also shows the height and minimum thickness of the webs for CMUs of each size. Half units were produced in the laboratory by cutting the standard stretcher units in two equal sections using the masonry saw to ensure that all units had similar material properties.

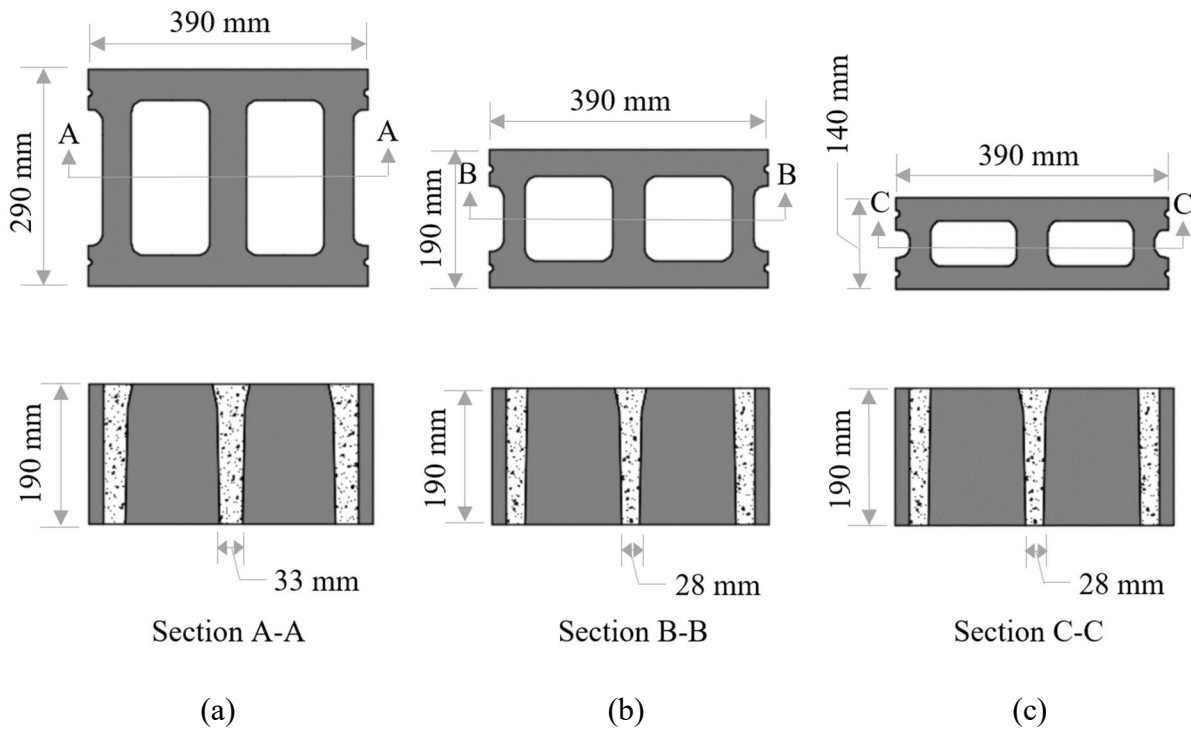


Figure 3.3: Dimensions and Cross-Sections of Standard Concrete Masonry Units of Size: (a) 300 mm (b) 200 mm, and (c) 150 mm

3.3.2 Mortar

Locally available masonry sand meeting the gradation requirements as specified in CSA A179-14 (CSA, 2014c) was supplied to the Structures Laboratory where it was stored in a steel bin until

needed. Lafarge Type MCS masonry cement was supplied in 17 kg moisture-resistant bags and stored on a wooden pallet. Mortar was batched and mixed in the laboratory, following the requirements specified in CSA A179-14 (CSA, 2014c), to meet the consistency desired by the mason for ease of block placement. The mortar used in prism construction was therefore categorized as a job-prepared mortar although it was mixed in the laboratory. CSA S304-14 (CSA, 2014b) requires a minimum 28-day compressive strength of 8.5 MPa for Type S job-prepared mortar in all structural applications. A cement-to-sand ratio of 1:2.5 by volume and a varying water-to-cement ratio of 0.7 to 0.8 were used to comply with the aforementioned criteria.

3.3.3 Grout

Lafarge Type GU cement was supplied in 20 kg moisture-resistant bags and was stored in the Structures Laboratory on a wooden pallet. Locally available masonry gravel containing a mixture of fine and coarse aggregates with a maximum aggregate size of 10 mm was delivered and stored in a steel bin until required. The gravel was pre-mixed by the supplier to satisfy the gradation requirements specified in CSA A179-14 (CSA, 2014c). Manual gradation was therefore not performed in the laboratory. Grout was batched and mixed in the laboratory with a 1:5 cement-to-aggregate ratio by volume and a target slump of 250 mm to meet the CSA A179-14 (CSA, 2014c) specifications. A water-to-cement ratio of approximately 1 was used to obtain the target slump.

3.4 Construction

All masonry prisms were constructed by an experienced mason. Mortar and grout were prepared by graduate students in the Structures Laboratory following the predefined mix designs as discussed in Sections 3.3.2 and 3.3.3, respectively. The properties of all constituent materials followed the minimum requirements as prescribed in CSA A179-14 (CSA, 2014c); an effort was made to keep these properties reasonably consistent for all specimens. Two construction phases were included in this investigation to limit the time between construction and testing to as close to the minimum 28 day curing time as possible. The mason was therefore retained for only one day a week such that prisms constructed in a single batch were all tested within a week following a minimum 28 day curing period. The detailed construction process of all prisms included in the current investigation is presented in the following sub-sections.

3.4.1 Mortar Preparation

Figure 3.4 (a) shows the mechanical mixer used for mixing the mortar following the specifications as described in Section 3.3.2. Mortar was hand-batched by first adding half of the sand and three-quarters of the estimated water into the rotating mixer. Mortar cement was then added slowly and mixed for one to two minutes, followed by the addition of the remaining water and sand. The mortar was further mixed for 3 minutes, and a small amount of additional water was added into the mix at the discretion of the mason until the desired consistency was reached.

CSA A179-14 (CSA, 2014c) requires a minimum of six 50 mm mortar cubes to be cast from each batch of mortar to determine its compressive strength. Two batches of mortar were prepared in a day during prism construction with each batch being used to construct fourteen prisms. A total of nine mortar cubes per batch were therefore cast to ensure that three mortar cubes were available during the first two days of prism testing and at least one mortar cube was available when the remaining prisms were tested. Figure 3.4 (b) shows the mortar cubes in the brass moulds that were cast in accordance with the moulding procedures in CSA A3004-C2 (CSA, 2008). Freshly mixed mortar was placed into these moulds in two 25 mm high layers with each layer tamped 32 times with a steel rod. These moulds were then covered with plastic sheets for approximately 48 hours following casting. The cubes were then removed from the moulds and stored in a similar curing environment to the corresponding prisms until they were tested.



(a)



(b)

Figure 3.4: Mortar Preparation: (a) Mortar Mixer, and (b) Cast Mortar Cubes

3.4.2 Grout Preparation

Figure 3.5 (a) shows the mechanical concrete mixer that was used for grout preparation. The quantity of materials required per batch of grout was estimated using the pre-determined mix design ratio as described in Section 3.3.3. The batching process involved placing half of the required water into the rotating mixer followed by the addition of half of the required gravel mix. All of the required cement was then added slowly into the rotating mixer. The remainder of the gravel mix and the water were then slowly added to attain the desired consistency. The grout was then allowed to mix for about five minutes and small amounts of additional water were added continuously, using judgment, to bring the slump of the grout to approximately 250 mm.

Slump testing, as shown in Figure 3.5 (b), was performed for every grout batch to ensure proper workability prior to filling the prisms. Two types of companion specimens were also cast to test the mechanical properties of each grout batch: absorptive prisms and non-absorbent cylinders in accordance with ASTM C1019-18 (ASTM, 2018) and CSA A179-14 (CSA, 2014c) specifications, respectively. Figure 3.5 (c) shows that four concrete blocks were arranged side by side to form a mould for absorptive grout prisms. A wooden piece of size 75 mm x 75 mm x 40 mm, covered by a plastic sheet, was used as a base to create the required 75 mm x 75 mm x 150 mm mould for the absorptive grout prisms. The height of these grout prisms was at least twice their width as specified in ASTM C1019-18 (ASTM, 2018). The moulds were then lined with permeable paper towels to ensure that the grout would not adhere to the concrete blocks. The grout was then placed in the moulds in two equal layers with each layer rodded 15 times in accordance with ASTM C1019-18 (ASTM, 2018). The top of the moulds was then covered with a plastic sheet and left for two days following initial casting before they were de-moulded and stored in a similar curing environment as the corresponding prisms until testing.

Figure 3.5 (d) shows that the non-absorbent grout cylinders were cast in 100 mm diameter by 200 mm high plastic moulds. The non-absorbent grout cylinders were cast in two equal layers with each layer rodded 20 times in accordance with CSA A179-14 (CSA, 2014c). The top of the non-absorbent grout cylinders was covered with a plastic sheet and allowed to cure under laboratory conditions for approximately 48 hours prior to demoulding. The specimens were then stored under similar curing conditions to the corresponding prisms until testing.



(a)



(b)



(c)



(d)

Figure 3.5: Grout Preparation: (a) Grout Mixer, (b) Slump Test, (c) Absorbent Grout Prism, and (d) Non-Absorbent Grout Cylinders

Three absorbent grout prisms were cast for each grout batch, resulting in a total of 36 grout prisms from 12 grout batches. An identical number of non-absorbent grout cylinders were also cast. Each set of grout specimens was labeled and recorded so that appropriate absorbent prisms and non-absorbent cylinders were tested on the same day as the corresponding masonry prisms.

3.4.3 Prism Construction

Table 3.2 shows the construction schedule for all prisms. A total of 28 masonry prisms representing four different test series were constructed in each of the first four building weeks. The remaining 14 prisms, representing two different test series, were constructed in the final week of construction.

Table 3.2: Masonry Prism Construction Schedule

Construction Phase	Construction Date	Test Series	Total Number of Prisms
1	Nov. 16, 2020	A200H	28
		A200G	
		C200H	
		C200G	
2	Dec. 11, 2020	B200H	21
		B200G	
		C150G	
2	Jan. 08, 2021	A150H	28
		A150G	
		B150H	
		B150G	
2	Jan. 18, 2021	A300H	28
		A300G	
		C300H	
		C300G	
2	Jan. 25, 2021	B300H	21
		B300G	
		C150H*	

*The construction of these prisms was originally planned to be included in the first phase but were ultimately cast in the second phase.

One batch of mortar was used to construct fourteen prisms making up all prisms in two test series. This ensured that all the mortar from a particular batch was consumed within an hour of mixing. Prisms were grouted, if applicable, one day after their construction. This allowed the mortar to set and cure for a minimum 24 hours prior to grouting and ensured that the mortar gained sufficient strength to resist any outward grout fluid pressure. Figure 3.6 (a) shows that the prisms constructed using knock-out CMUs had open ends on either side. Duct tape was used on the remaining portion

of the webs to facilitate the smooth removal of the formwork 48 hours after grouting. Figure 3.6 (b) shows that small plywood sheets were attached using duct seal on both sides of the bottom and top courses to accommodate the frog ends and confine the grout within the core of knock-out CMUs. This ensured consistency in the cross-sectional area across all grouted prisms constructed using CMUs of each size. Figure 3.6 (c) shows the completed formwork which consisted of two 25 mm x 400 mm x 600 mm plywood pieces wrapped with a plastic sheet and installed on the side faces of each prism. These plywood pieces were held together by four 50 mm x 100 mm wooden studs, two on each side, and two 50 mm long metal screws at either end of each wooden stud. The inner side of the plywood pieces used on either end of the prism was covered using a plastic sheet to prevent moisture absorption from the fresh grout. Required formwork was installed just before the grout was placed into the cells and was removed after 48 hours. Grout was manually compacted using a steel rod to ensure proper compaction.



(a)



(b)



(c)

Figure 3.6: Formwork: (a) Open-Ended Knock-Out Prisms, (b) Preliminary Formwork, and (c) Completed Formwork

All masonry prisms and corresponding companion specimens were cured for a minimum of 28 days in laboratory conditions in accordance with CSA S304-14 (CSA, 2014b) requirements. Figure 3.7 (a) shows the curing of hollow masonry prisms whereas, Figure 3.7 (b) shows the curing of grouted masonry prisms. The exposed top surface of the grouted prisms was covered with a plastic sheet for 48 hours following grout placement to prevent moisture loss and to match the curing conditions of the corresponding grout companion specimens consisting of non-absorbent grout cylinders and absorptive grout prisms.



(a)



(b)

Figure 3.7: Prism Curing: (a) Hollow Prisms, and (b) Grouted Prisms

3.5 Instrumentation and Testing

Masonry prisms included in this experimental investigation were evaluated for their assemblage strength and resulting failure modes. A compression test setup available in the laboratory was used to determine the masonry assemblage strength of prisms, whereas a non-contact and non-destructive technique known as digital image correlation (DIC) was used to investigate the resulting failure mode of the prisms. This method of measuring full-field surface deformation of masonry prisms is based on a principle of correlation between images of the undeformed and subsequently deformed specimen captured using digital cameras during testing. The following sub-sections outline the preparation of masonry prisms for use with the digital image correlation (DIC) system and describe the testing procedures for both the masonry prisms and companion specimens.

3.5.1 Setup of the Digital Image Correlation System

Figure 3.8 shows the setup for Digital Image Correlation (DIC) system that was used to measure the strain in each masonry prism during testing for the purpose of studying their failure modes. The lenses for the camera were chosen considering the size of the prisms and the space available in the laboratory. Two equipment sets (Systems 1, and 2) each consisting of two cameras with 2,448 x 2,048-pixel resolution and 1.4/17 mm Schneider lenses were set up facing one of the exterior face shell and web face of the masonry prism to obtain a full-field image. The cameras in each system were spaced 300 mm apart and at a 380 mm height from the floor level to obtain a suitable stereo angle that covered the entire specimen surface. An effort was made to ensure that each set of cameras was focused and leveled on both horizontal axes before they were used. Figure 3.8 also shows that light-emitting diodes (LED) were used as artificial lighting to illuminate the specimen surfaces under consideration so that the speckle patterns were clearly visible.

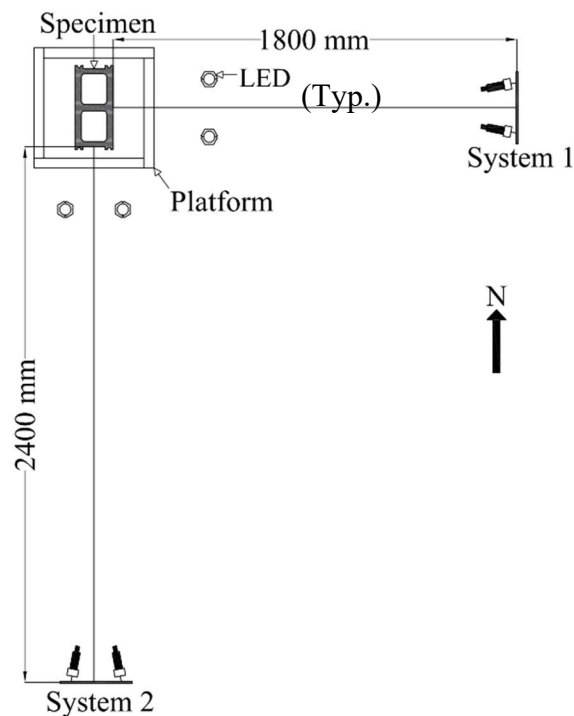


Figure 3.8: Setup for Digital Image Correlation System

Clause D.4.6 of Annex D as included in CSA S304-14 (CSA, 2014b) specifies instrumenting at least five prisms to measure their deformation properties. Five replicates from each test series were therefore used to obtain full-field strains and crack patterns on one of the exterior face shell and

web face of the prisms. For this, one front and side face of each specimen was painted flat white (Figure 3.9 (a)), followed by the application of random black dots known as a speckle pattern (Figure 3.9 (b)). Prisms were painted flat white using a polyester roller after removing any loose materials from the surface, with the speckle pattern applied using black spray paint once the previously applied white paint had dried. The specimen dimension (height = 590 mm) and the image resolution (2,448 pixel) were related to determine the appropriate pixel spacing in terms of mm/pixel (Cintron & Saouma, 2015) required for this research and was found to be approximately 0.25 mm/pixel (590 mm/2,448 pixel). Speckles of a minimum 3-pixel size were required to avoid distortion (Reu, 2015), resulting in speckles of a minimum 0.75 mm diameter to be painted on the test faces of the prism. A speckle pattern with a density of about 50 % was generated that allowed the DIC system to accurately measure the strain gradient (Reu, 2015).



Figure 3.9: Painted Face-Shell for DIC: (a) Flat White, and (b) Black Speckle Pattern

3.5.2 Loading Frame and Testing Procedures

Compressive strength testing of all masonry prisms was conducted in accordance with CSA S304-14 Annex D (CSA, 2014b). The prisms were tested in the same order as they were constructed after curing for a minimum of 28 days.

Figure 3.10 shows the test setup used for applying a concentric compressive load to the masonry prisms. Two 1000 kN actuators, as available in the Structures Laboratory, were connected using a

stiffened steel I-beam to obtain a combined capacity of 2000 kN. The actuators were braced laterally using two 64 mm x 64 mm equal leg steel angles to prevent any rotation of the knuckle joint and ensure that no bending was induced in prisms while loading. This allowed for the resulting masonry assemblage strengths to be directly compared. An upper masonry platen meeting CSA S304-14 (CSA, 2014b) requirements was attached to the lower flange of an I-beam using two 12 mm ASTM A325M bolts. The masonry platen assembly consisted of an upper platen attached to the spherical head seat fitted into a socket plate to ensure uniform load application. A 100 mm thick metal plate was used as a lower platen to provide a rigid and smooth surface for the masonry prisms. The actuators were operated in load control to apply the first half of the expected maximum load, P_{max} , (i.e., 0 to $0.5P_{max}$) at a convenient rate, with the remaining load (i.e., $0.5P_{max}$ to P_{max}) applied within one to two minutes at a uniform rate. A computer-controlled data acquisition system was used to record the applied load at a frequency of 1 Hz.

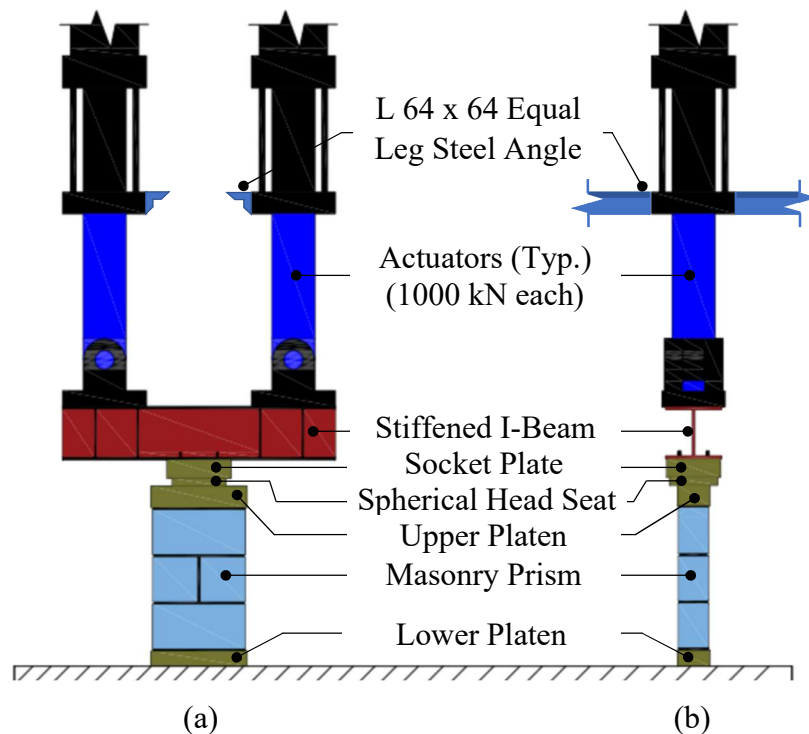


Figure 3.10: Prism Test Setup: (a) Front View, and (b) Side View

A two-wheeled trolley was used to transport the prisms onto the testing platform. Figure 3.11 shows a prism positioned for testing on the platform. Each prism was positioned in the test setup directly below the center of the upper platen to ensure that a concentric compression load was

applied. Fibreboard was also placed at the bottom and top of the prism to ensure uniform loading over the entire contact area of the prism. Strips of fibreboard were used along the face-shells for hollow prisms whereas a fibreboard sheet covering the entire width and length of the prisms was used for grouted prisms.



Figure 3.11: Prism Positioned in the Test Setup

The two sets of cameras for the operation of the DIC system were installed and focused on the painted prism faces, as discussed in Section 3.5.1. Stereo calibration of the cameras was then conducted using a 40 mm calibration grid placed over each painted prism surfaces to cover 100% of the area. A total of 25 images of the calibration grid per painted face were taken by rotating it about the X, Y, and Z axes before testing each prism, and were processed using a stereo calibration tool in Vic 3D software (Correlated Solutions, 2018) to calibrate both sets of cameras. An effort was made to ensure that the average error score was within the acceptable range as specified by the software.

The actuators were then lowered until the bottom face of the upper platen made contact with the fibreboard placed on top of the prism. Following this, a compressive load was applied to the prism until failure occurred and images were taken simultaneously at a frequency of 1Hz throughout loading.

3.5.3 Testing of Companion Specimens

Companion specimens were tested to evaluate the compressive strength of the concrete masonry units, mortar, and grout. All tests were performed in accordance with the relevant CSA and ASTM standards. Mortar cubes, non-absorbent grout cylinders, and absorptive grout prisms were tested on the same day as the corresponding masonry prisms in an effort to best predict the material properties at the time of prism testing.

Testing of Concrete Masonry Units

Six randomly selected units for each CMU size were tested for compressive strength in accordance with ASTM C140-20 (ASTM, 2020) using the 200-tonne capacity Amsler beam bender as available in the Structures Laboratory. Figure 3.12 shows that a 25 mm thick steel plate and a steel spreader beam were placed on top of the concrete masonry units to ensure that load was applied uniformly. Fibreboard was also placed just above and below each CMU to ensure smooth and flat loading surfaces. A 1500 kN load cell was used to measure the load, with a computerized data acquisition system used to record the applied load with a frequency of 10 Hz.

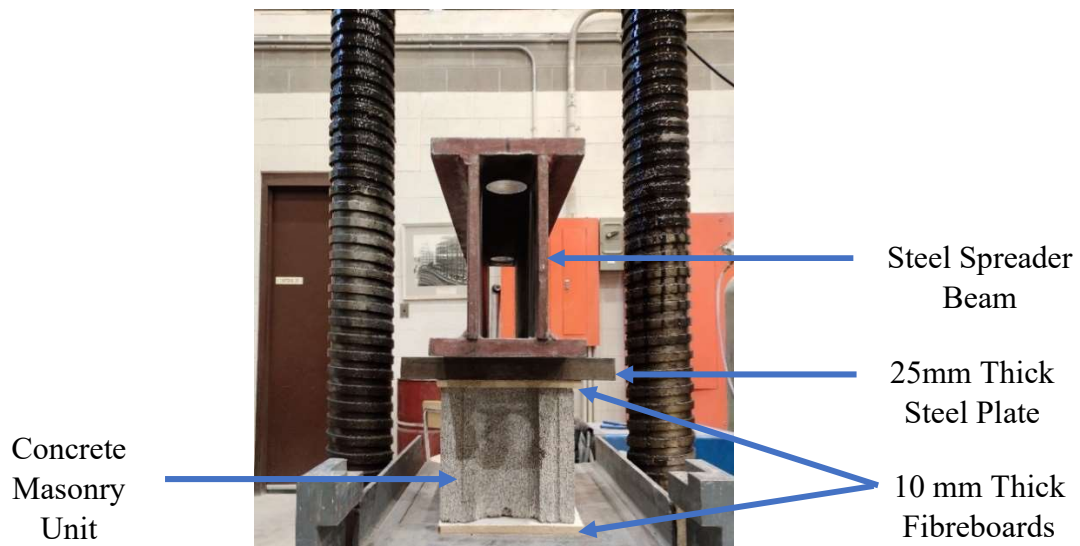


Figure 3.12: Concrete Masonry Unit Test Setup

Testing of Mortar Cubes

A total of 90 mortar cubes resulting from ten batches of mortar were tested according to CSA A179-14 (CSA, 2014c) during the experimental program. The Instron 600DX Universal Testing Machine (UTM), as shown in Figure 3.13, was used to determine the compressive strength (MPa)

of the mortar cubes. Each cube was placed in the UTM, as shown in Figure 3.13, with the smooth surfaces produced by the brass moulds in contact with the upper and lower bearing blocks of the test machine. This ensured the uniform loading over the contact surfaces of mortar cubes. All mortar cubes were tested until failure and the computerized data acquisition system recorded the applied stress at a frequency of 10 Hz.



Figure 3.13: Mortar Cube Test Setup

Testing of Non-Absorbent Grout Cylinders

Non-absorbent grout cylinders were tested in accordance with ASTM C1019-18 (ASTM, 2018) using the Instron 600DX Universal Testing Machine as available in the Structures Laboratory. Figure 3.14 shows a typical test of a grout cylinder. Sulfur capping was used at the top and bottom of each cylinder to ensure uniform load application. All specimens were tested until failure and the corresponding ultimate compressive stress was recorded using the computer-controlled data acquisition system at a frequency of 10 Hz.



Figure 3.14: Non-Absorbent Grout Cylinder Test Setup

Testing of Absorptive Grout Prisms

Absorptive grout prisms were also tested using the Instron 600DX Universal Testing Machine in accordance with ASTM C1019-18 (ASTM, 2018). Figure 3.15 shows the typical arrangement of a grout prism in the testing machine with fibreboard sheets placed both above and below the prism to ensure uniform loading over the contact surfaces. The cross-sectional dimensions of each grout prism were measured using a digital vernier caliper and recorded. This was done due to the slight variation in the cross-section of the as-arranged moulds using concrete masonry units. All specimens were tested until failure and the corresponding failure load was recorded using the computer-controlled data acquisition system at a frequency of 10 Hz. The failure load of each grout prism was divided by its measured cross-sectional area to obtain the compressive strength.

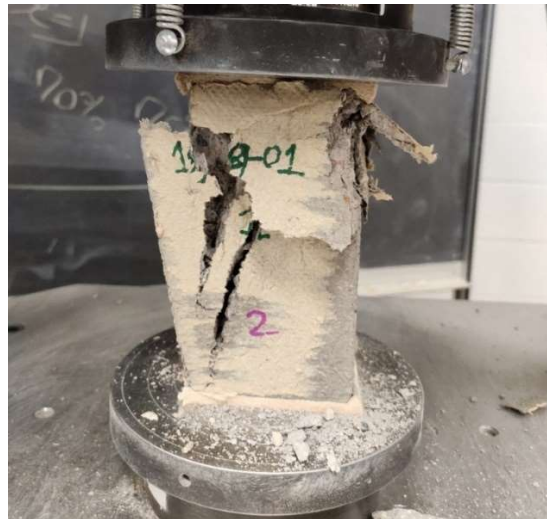


Figure 3.15: Absorptive Grout Prism Test Setup

3.6 Summary

This chapter included a description of different masonry prism configurations and the material properties, followed by the construction and testing of masonry prisms, and the companion specimens. The results of the experimental investigation are presented in Chapter 4.

CHAPTER 4: EXPERIMENTAL RESULTS AND ANALYSIS

This chapter presents the results of 126 masonry prism tests and associated companion specimens as were included in the experimental program. Table 4.1 shows the test schedule for the two construction phases along with the number of test specimens included in each phase (test series IDs are defined in Section 3.2). All companion specimens were tested in conjunction with the corresponding masonry prisms. The companion test results are presented and discussed first followed by the masonry prism test results. The representative crack patterns and failure modes of prisms within each test series as obtained from the data collected from the digital image correlation (DIC) system are then presented and discussed. The corresponding stress versus strain plots are also presented and discussed. The results obtained from the DIC system were also compared to those obtained from finite element modeling (FEM) to validate the effectiveness of the DIC technique. The collected data were analyzed to investigate the impact of CMU web height on the resulting masonry assemblage strength and failure modes of prisms.

Table 4.1: Test Schedule

Construction Phase	Test Date	Test Series	Age @ Test (Days)	Number of Specimens Tested in Each Phase				
				Masonry Prisms	Mortar Cubes	Grout Prisms	Grout Cylinders	
1	Dec. 14-18, 2020	A200H	28-32	28				
		A200G						
		C200H						
		C200G						
1	Jan. 08-14, 2021	B200H	28-34	21				
		B200G						
		C150G						
2	Feb. 05-11, 2021	A150H	28-34	28				
		A150G						
		B150H						
	2	Feb. 16-19, 2021	B150G	29-32	14		54	6
			C300H					
2	Feb. 22-23, 2021	A300H	28-29	14				
		B300H						
		C150H						

4.1 Companion Specimen Test Results

Each masonry prism consisted of CMUs, mortar, and, in certain cases, grout. The properties of these constituent materials needed to be determined to evaluate their influence on the masonry assemblage strength. The following subsections describe the test results of the companion specimens associated with different test series included in this experimental investigation. Absorption test results for the concrete masonry units are also presented. All companion specimens were tested in accordance with the relevant standards as discussed in Section 3.5.3.

4.1.1 Concrete Masonry Units

A total of six frog-ended concrete masonry units were randomly selected for each size included in the investigation and tested under compression in accordance with ASTM C140 (ASTM, 2020), as discussed in Section 3.5.3. The net effective area required in the calculation of the resulting compressive strength was calculated based on the as-measured dimensions of the CMUs as procured. These details are reported in Tables 4A-1 and 4A-2 as included in Appendix 4A.

Table 4.2 shows the average compressive strength of CMUs for all sizes including the resulting standard deviations and coefficients of variation (*COV*). All CMUs, irrespective of size, achieved a minimum nominal compressive strength of 15 MPa. There were no physical outliers, and no statistical outliers were identified using the procedures provided in ASTM E178 – *Standard Practice for Dealing with Outlying Observations* (ASTM, 2021) at the 95% confidence level. The results from the individual CMU compression tests are presented in Table 4A-3 as included in Appendix 4A.

Table 4.2: Compression Test Results for Concrete Masonry Units

Nominal CMU size (mm)	Average Compressive Strength (MPa)	Standard Deviation (MPa)	<i>COV</i> (%)
150	29.2	3.05	10.5
200	31.2	2.54	8.15
300	21.5	1.41	6.55

A total of six concrete masonry units of each size were also randomly selected for absorption testing. The submerged weight, saturated weight, and oven-dry weight of these selected CMUs were measured as per the procedures provided in ASTM C140 (ASTM, 2020) and are reported in Table 4A-4 as included in Appendix 4A. Table 4.3 shows the average results obtained from the absorption tests and the respective coefficients of variation (*COV*) for each CMU size. The results obtained from the absorption tests were within the range as specified in CSA A165.1-14 (CSA, 2014a).

Table 4.3: Absorption Test Results for Concrete Masonry Units

Nominal CMU size (mm)	Average Moisture Content (%)	<i>COV</i> (%)	Average Absorption (%)	<i>COV</i> (%)	Average Density (kg/m ³)	<i>COV</i> (%)
150	1.14	18.3	3.37	9.63	2260	0.70
200	1.09	17.2	4.46	15.3	2270	1.95
300	1.42	16.3	4.41	8.73	2250	1.09

4.1.2 Mortar Cubes

A total of 9 cubes per mortar batch, resulting in 90 mortar cubes from 10 batches, were tested under compression following the procedures outlined in Section 3.5.3. Table 4.4 shows the average compressive strength and coefficient of variation (*COV*) of the mortar cubes tested from each batch. Each mortar batch was used to construct no more than two test series of prisms (therefore, for 7 to 14 prisms). For example, mortar batch number 1 was used to construct all prisms in the A200H and A200G test series. The average compressive strength of the mortar cubes ranged from 8.98 to 22.7 MPa, which exceeded the minimum 28-day compressive strength of 8.5 MPa for Type S mortar cubes as explained in Section 3.3.2 and specified in CSA S304-14 (CSA, 2014b). There were no physical outliers, and no statistical outliers were identified within each mortar batch using the procedures specified in ASTM E178 – *Standard Practice for Dealing with Outlying Observations* (ASTM, 2021) at the 95% confidence level. The results from the individual mortar cube tests are reported in Table 4A-5 as included in Appendix 4A.

Table 4.4: Compression Test Results for Mortar Cubes

Batch Number	Prism Test Series	Average Compressive Strength (MPa)	COV (%)
1	A200H & A200G	16.3	16.9
2	C200H & C200G	8.98	11.0
3	B200H & B200G	13.1	22.5
4	C150G	13.8	15.5
5	A150H & A150G	18.7	13.2
6	B150H & B150G	22.7	13.3
7	A300H	15.9	7.16
8	C300H	19.0	14.1
9	B300H	12.7	13.6
10	C150H	16.7	5.05

The compressive strength of the mortar cubes varied from 8.98 to 22.7 MPa between batches. The mortar was manually mixed in the laboratory as described in Section 3.4.1; it is therefore very likely that the variation in material quantities and workmanship may have contributed to a variation in results between batches. Similarly, the consistency of mortar was varied between the batches by adding additional water as desired by the mason to construct different test series of prisms. This would have also contributed to the variation in the reported values. Previous researchers (Hamid et al., 1985; Khalaf, 1996) concluded that mortar strength has a negligible impact on assemblage strength for grouted prisms because of the continuity provided by the grout cores. Similarly, results reported in past studies (Chahine, 1989; Drysdale & Hamid, 1979; Khalaf, 1996) showed that assemblage strength for hollow prisms was not largely influenced by mortar strength. It can therefore be assumed that the assemblage strength of prisms constructed using each CMU size was not sensitive to differences in mortar compressive strength.

4.1.3 Non-Absorbent Grout Cylinders and Absorptive Grout Prisms

Both non-absorbent grout cylinders and absorptive grout prisms were tested in accordance with relevant standards, using the procedures outlined in Section 3.5.3, to establish the compressive strength of the grout used in prism construction.

Three non-absorbent grout cylinders and three absorptive grout prisms were tested from each grout batch to establish its compressive strength. Results from the absorptive grout prisms tests can provide an indication of the effect of reduction in water content of the grout mix due to the absorption by the concrete masonry units (Drysdale & Hamid, 2005). Table 4.5 shows the average compressive strength and coefficient of variation (*COV*) of both the non-absorbent grout cylinders and absorptive grout prisms resulting from each grout batch. Test results for both non-absorbent grout cylinders and absorptive grout prisms used in constructing 300 mm grouted prisms are not included given that the associated prisms were not tested as will be explained in Section 4.2. The average compressive strength of the non-absorbent grout cylinders and absorptive grout prisms ranged from 13.7 to 20.8 MPa and 13.6 to 22.8 MPa, respectively. These values exceeded the minimum 28-day compressive strength requirement of 12.5 MPa as specified in CSA A179 (CSA, 2014b). The variation in the reported results could be due to several factors such as different moisture content of aggregates for different batches, variation in material quantities, and workmanship. The average compressive strength of absorptive grout prisms was generally greater than that of corresponding non-absorbent grout cylinders. Water absorption by the CMUs used as a mould resulted in a reduced water-cement ratio which increased the measured compressive strength of these specimens in comparison to those obtained for the non-absorptive cylinders. No physical or statistical outliers were identified. The individual test results for these specimens are presented in Tables 4A-6 and 4A-7 as included in Appendix 4A.

Table 4.5: Compression Test Results for Non-Absorbent Grout Cylinders and Absorptive Grout Prisms

Batch Number	Prism Test Series	Non-Absorbent Grout Cylinders		Absorptive Grout Prisms	
		Average Compressive Strength (MPa)	<i>COV</i> (%)	Average Compressive Strength (MPa)	<i>COV</i> (%)
1	A200G	20.8	0.98	22.8	6.61
2	C200G	13.7	5.55	14.4	8.36
3	B200G	16.0	4.34	16.5	15.3
4	C150G	16.2	5.73	16.3	11.4
5	A150G	16.1	3.59	13.6	8.10
6	B150G	16.3	3.62	14.0	7.27

The average compressive strength of non-absorbent grout cylinders ranged from 16.1 to 16.3 MPa and 13.7 to 20.8 MPa for prisms constructed using 150 mm and 200 mm CMUs, respectively. Similarly, the average compressive strength of absorptive grout prisms ranged from 13.6 to 16.3 MPa and 14.4 to 22.8 MPa for prisms constructed using 150 mm and 200 mm CMUs, respectively. Previous researchers (Chahine, 1989; Drysdale & Hamid, 1979; Khalaf, 1996) showed that the measured strength of grout has little impact on masonry assemblage strength as long as it meets the minimum strength requirements. The assemblage strength of grouted prisms was therefore not thought to be sensitive to the difference in compressive strength between grout batches used in the current experimental investigation.

4.2 Masonry Prism Compression Test Results and Analysis

A total of eighteen unique test series were designed and constructed in this experimental study as described in Section 3.2. Only fifteen test series could be tested as the actual assemblage strength for the A300G, B300G, and C300G prisms were found to be higher than the predicted value during testing. Testing of these masonry prism specimens could not be completed using the actuators with a combined 2000 kN capacity as available in the laboratory despite several attempts. The procedures for the testing of masonry prisms are discussed in Section 3.5.2.

Table 4.6 shows the as-tested mean masonry assemblage strength (\bar{f}_m) and the corresponding coefficients of variation (COV) for prisms within each test series. A comparative analysis of these values are provided in subsequent sub-sections to evaluate the impact of CMU web height on the resulting masonry assemblage strength of both hollow and grouted prisms. The results from the individual masonry prism tests are presented in Table 4B-1 as included in Appendix 4B. The effective mortared areas, as discussed in Section 4.1.1, were used to calculate the masonry assemblage strength for hollow and grouted prisms constructed using each CMU size.

Table 4.6: Compression Test Results for Masonry Prisms

Test Series	\bar{f}_m (MPa)	<i>COV</i> (%)	Test Series	\bar{f}_m (MPa)	<i>COV</i> (%)
A150H	23.7	9.06	A150G	17.6	8.70
B150H	18.5	25.8	B150G	19.9	5.32
C150H	17.6	30.5	C150G	16.5	9.77
A200H	25.2	13.0	A200G	17.2	15.1
B200H	23.7	12.2	B200G	15.8	13.1
C200H	13.8	15.6	C200G	16.5	5.70
A300H	27.7	7.27	A300G		
B300H	28.6	3.82	B300G	N/A	N/A
C300H	24.5	7.78	C300G		

The following subsections include the detailed results and analysis of compression testing for all prisms. Results for prisms constructed with either of three different CMU sizes could not be compared directly since their height-to-thickness ratio (h/t) and compressive strength of the CMUs used to construct them differed. Direct comparisons were therefore limited to prisms constructed using CMUs with either of three web heights but of the same size.

4.2.1 Hollow Prisms

Figure 4.1 shows a comparison of the compression test results for hollow prisms constructed using 150 mm CMUs of three different web heights. The A150H prisms had the highest mean assemblage strength at 23.7 MPa with *COV* of 9.06%, while the C150H prisms had the lowest mean assemblage strength at 17.6 MPa with *COV* of 30.5%. This represented around a 26% reduction in the mean assemblage strength. Furthermore, the B150H prisms had a mean assemblage strength of 18.5 MPa with *COV* of 25.8% which represented a 22% reduction in comparison to those in A150H series. The mean assemblage strength of prisms was found to decrease with reduction in web height of CMUs used in prism construction. The difference in web heights appeared to affect the ability of face shells to resist the externally applied axial load, thereby affecting the overall resistance of the prisms. The *COV* varied largely between the different test series of prisms and was found to increase with decreasing web height of CMUs used in prism

construction. This was likely the result of unobserved cracking in some of the webs while knocking them out in the laboratory that caused a few prisms to fail prematurely when subject to loading.

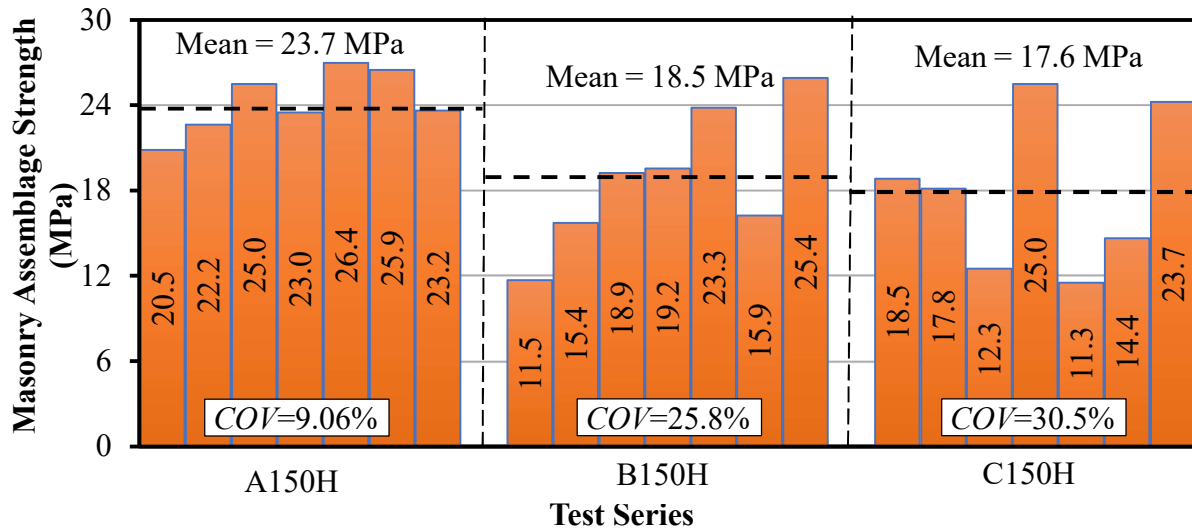


Figure 4.1: Assemblage Strength of Hollow Prisms Constructed with 150 mm CMUs

A one-way ANOVA test was conducted to evaluate whether the assemblage strength of hollow prisms constructed with 150 mm CMUs was significantly influenced by the CMU web height. The assemblage strength of hollow prisms constructed with 150 mm CMUs was found to be significantly influenced by the CMU web height at the 95% confidence level. A Tukey’s post-hoc test based on the assumption of homogeneity of variances was subsequently conducted to determine which two test series were significantly different. The mean assemblage strength of the C150H prisms was found to be significantly lower than those in A150H series at the 95% confidence level. This suggested that the use of 150 mm ASTM C90 (ASTM, 2011) knock-out units significantly lowered the resulting masonry assemblage strength of prisms in comparison with those constructed with standard full-height web units. In contrast, there was no statistically significant difference in the mean assemblage strength between the A150H and B150H prisms. This suggested that the use of 150 mm CSA A165.1 (CSA, 2014a) knock-out units resulted in statistically similar masonry assemblage strength as that of prisms constructed with standard full-height web units at the 95% confidence level. The associated statistical analysis results are presented in Tables 4B-2 and 4B-3 included in Appendix 4B.

Figure 4.2 shows a comparison of the compression test results for hollow prisms constructed using 200 mm CMUs of three different web heights. The A200H prisms had the highest mean assemblage strength at 25.2 MPa with *COV* of 13.0%, while the C200H prisms had the lowest mean assemblage strength at 13.8 MPa with *COV* of 15.6%: a 45% reduction in value in comparison with the A200H prisms. Moreover, the B200H prisms had a mean assemblage strength of 23.7 MPa with *COV* of 12.2% which represented only a 6% reduction in value in comparison to those in the A200H series. The mean assemblage strength of prisms was found to decrease with a reduction in CMU web height. The *COV* generally increased with decreasing CMU web height. This finding was similar to those hollow prisms constructed with 150 mm CMUs and was likely due to both CMU sizes having the same web thicknesses as reported in Table 4A-1 of Appendix 4A. Further, *COV*s were comparatively lower than for hollow prisms constructed with 150 mm CMUs, a finding resulting likely from the relative increase in lateral stability of prisms with a lower *h/t* ratio in comparison to those obtained for prisms constructed with 150 mm CMUs.

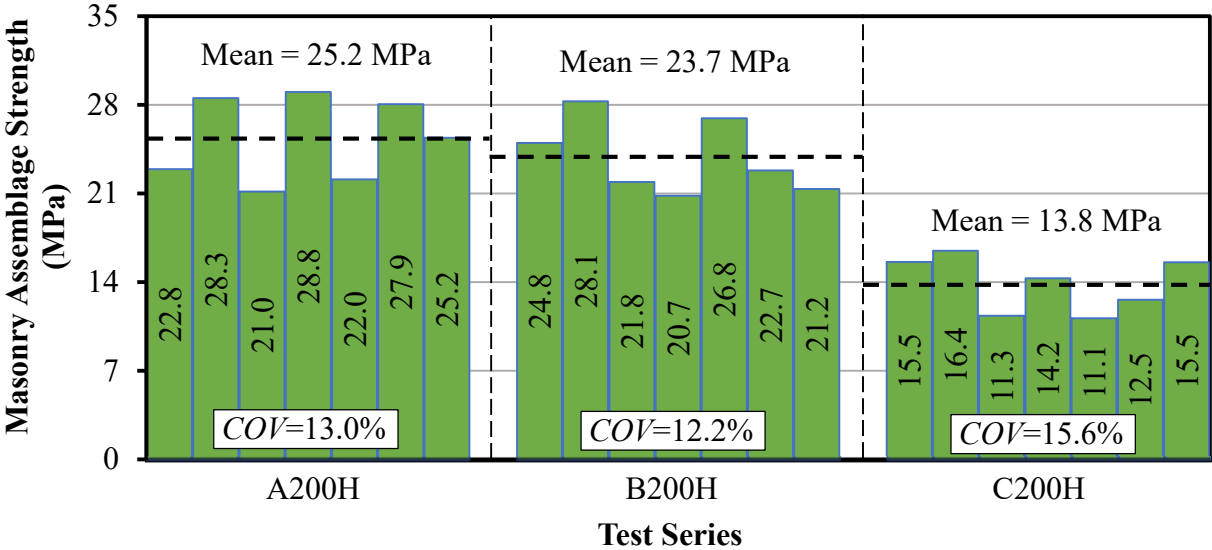


Figure 4.2: Assemblage Strength of Hollow Prisms Constructed with 200 mm CMUs

A one-way ANOVA test was conducted to evaluate whether the assemblage strength of hollow prisms constructed with 200 mm CMUs was significantly influenced by the CMU web height. Similar to prisms constructed with 150 mm CMUs, CMU web height had a statistically significant impact at the 95% confidence level on the resulting assemblage strength of hollow prisms. A Tukey’s post-hoc test based on the assumption of homogeneity of variances was then used to

determine which two test series were significantly different. The mean assemblage strength of the C200H prisms was found to be significantly lower than those in the A200H series at the 95% confidence level. This suggested that the use of 200 mm ASTM C90 (ASTM, 2011) knock-out units significantly lowered the resulting masonry assemblage strength in comparison with those constructed with standard full-height units. However, no statistically significant difference in mean assemblage strength existed between the A200H and B200H prisms, suggesting that the use of 200 mm CSA A165.1 (CSA, 2014a) knock-out units had no significant impact on the resulting masonry assemblage strength at the 95% confidence level in comparison with those constructed with standard full-height units. The associated statistical analysis results are presented in Tables 4B-2 and 4B-3 included in Appendix 4B.

Figure 4.3 shows a comparison of the compression test results for hollow prisms constructed using 300 mm CMUs of three different web heights. The compression test results of prisms were fairly similar across all three test series (A300H, B300H, and C300H). The B300H prisms had the highest mean assemblage strength at 28.6 MPa with *COV* of 3.82% while the C300H prisms had the lowest mean assemblage strength at 24.5 MPa with *COV* of 7.78%. This represented around a 14% reduction in the mean assemblage strength in comparison with the B300H prisms. Furthermore, the A300H prisms had a mean assemblage strength of 27.7 MPa with *COV* of 7.27% which represented a 3% reduction in value in comparison with those in the B300H series. Unlike hollow prisms constructed using either 150 or 200 mm CMUs, the mean assemblage strength of hollow prisms constructed using 300 mm CMUs did not exhibit a definitive trend with the reduction in CMU web height. The *COVs* were mostly similar across the three different test series. The thicker webs in 300 mm CMUs, 33 mm as compared to 28 mm in either 150 or 200 mm as reported in Table 4A-1, likely resisted the occurrence of any micro-cracks while knocking them out and so produced more consistent results. The *COVs* were also comparatively lower than for hollow prisms constructed with either 150 or 200 mm CMUs. The increased lateral stability in prisms due to further reduction in *h/t* ratio, as previously discussed, reduced the scatter in the test results.

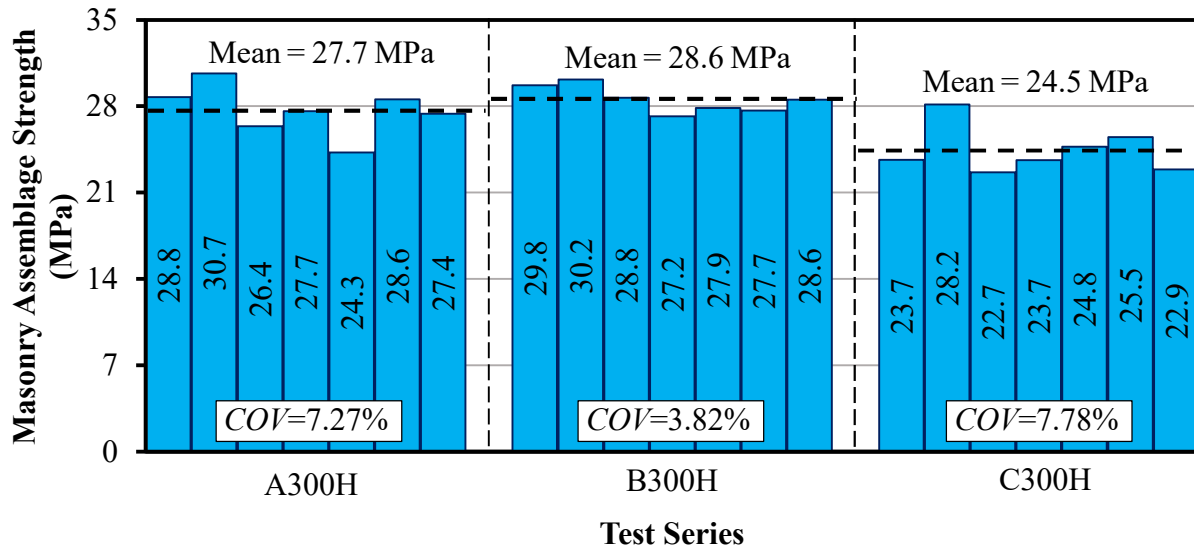


Figure 4.3: Assemblage Strength of Hollow Prisms Constructed with 300 mm CMUs

A one-way ANOVA test was conducted to evaluate whether the assemblage strength of hollow prisms constructed with 300 mm CMUs was significantly influenced by CMU web height. The CMU web height had a significant impact on the assemblage strength of hollow prisms constructed with 300 mm at the 95% confidence level. A Tukey’s post-hoc test based on the assumption of homogeneity of variances was then conducted to determine which two test series were significantly different. The analysis results were similar to those of hollow prisms constructed using either 150 or 200 mm CMUs. It was therefore concluded that the use of CSA A165.1 (CSA, 2014a) knock-out units did not significantly affect the resulting masonry assemblage strength, whereas the use of ASTM C90 (ASTM, 2011) knock-out units caused a significant reduction in the resulting masonry assemblage strength at the 95% confidence level in comparison with prisms constructed using standard full-height units. The associated statistical analysis results are presented in Tables 4B-2 and 4B-3 included in Appendix 4B.

Figure 4.4 shows a summary of the mean masonry assemblage strength for all hollow prisms. The assemblage strength of hollow prisms generally decreased with the reduction in the web height of CMUs used in prism construction, irrespective of the CMU size. No definitive overall trend existed across different CMU sizes. Results from statistical analyses showed that the use of ASTM C90 (ASTM, 2011) knock-out units in prism construction significantly lowered the resulting masonry assemblage strength of hollow prisms, whereas CSA A165.1 (CSA, 2014a) knock-out units can

be effectively used in hollow prism construction to obtain similar resulting masonry assemblage strength as those prisms constructed with standard full-height web units, irrespective of the CMU size. A regression analysis was conducted to establish a mathematical relationship between CMU web height and the resulting masonry assemblage strength for all CMU sizes. The results are presented in Figure 4B-1 as included in Appendix 4B. A low R^2 value, ranging from 0.315 to 0.791 for best fitting polynomial trend lines of order 2 as shown in Figure 4B-1, indicated that the variation in the resulting masonry assemblage strength of hollow prisms constructed with CMU of sizes 150, 200, and 300 mm was not effectively explained by the web height of CMUs considered in this study. An accurate mathematical relationship therefore could not be confidently established.

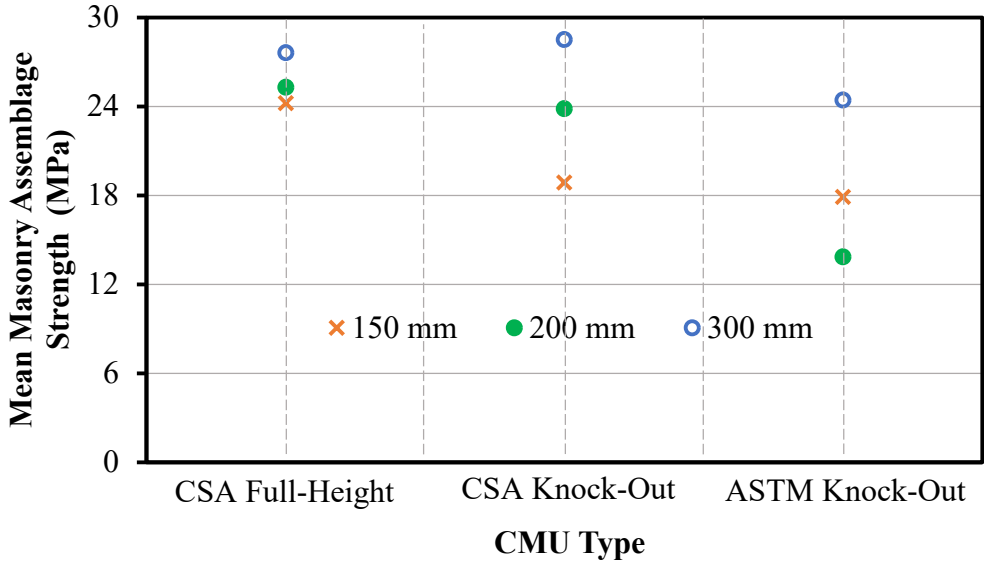


Figure 4.4: Summary of Assemblage Strength for Hollow Prisms

4.2.2 Grouted Prisms

Figure 4.5 shows a comparison of the compression test results for grouted prisms constructed using 150 mm CMUs of three different web heights. The B150G prisms had the highest mean assemblage strength at 19.9 MPa with *COV* of 5.32%, while the C150G prisms had the lowest mean assemblage strength at 16.5 MPa with *COV* of 9.77%: a 17% reduction in the mean masonry assemblage strength in comparison with the B150G prisms. Similarly, the A150G prisms had a mean assemblage strength of 17.6 MPa with *COV* of 8.70% which represented an 11% reduction in comparison to those in the B150G series and a 6 % increase in comparison to those in the C150G series. No definitive overall trend was obtained for the resulting masonry assemblage strength of

prisms across the three test series with the reduction in CMU web height. The mean assemblage strength of the A150G prisms, 17.6 MPa, was noticeably lower than for prisms in the A150H series, 23.7 MPa, as would be expected due to extra lateral pressure exerted by the grout on CMUs due to the difference in their elastic properties (discussed in Section 2.4.3). In contrast, the mean assemblage strength of grouted prisms constructed using either type of knock-out CMUs was mostly similar to that of the corresponding hollow prisms (B150H = 18.5 MPa and C150H = 17.6 MPa). The knock-out web geometry eliminated the possibility of void formation during grouting between the two ends of the frog-ended units within the middle course of prisms laid in running bond. This enhanced the stability of grouted prisms constructed using knock-out web CMUs and so resulted in relatively higher than expected strength. The *COVs* for grouted prisms across the three test series were mostly similar and lower than for corresponding test series of hollow prisms. This was due to the stability provided by the grout columns against the potential buckling of the prisms, thereby increasing the consistency and reducing the scatter of test results.

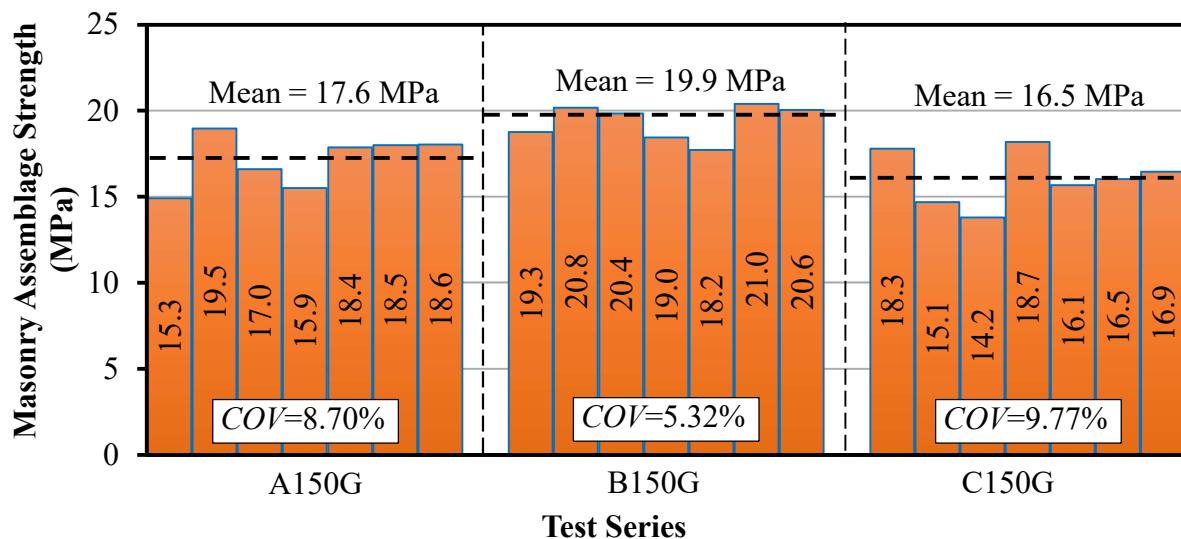


Figure 4.5: Assemblage Strength of Grouted Prisms Constructed with 150 mm CMUs

A one-way ANOVA test was conducted to evaluate whether the assemblage strength of grouted prisms constructed with 150 mm CMUs was significantly influenced by CMU web height. It was found that CMU web height had a significant impact on the masonry assemblage strength of grouted prisms constructed with 150 mm CMUs at the 95% confidence level. A Tukey’s post-hoc test based on the assumption of homogeneity of variances was then conducted to determine which

two test series were significantly different. No significant difference in mean masonry assemblage strength was found between the A150G and C150G prisms. The use of 150 mm ASTM C90 (ASTM, 2011) knock-out units in grouted prisms therefore resulted in statistically similar masonry assemblage strength to that of grouted prisms constructed with standard full-height web units at the 95% confidence level. Grout used to fill all the core space in the prism including the knockout zones provided structural integrity to prisms, thereby diminishing the effect of shorter web height of CMUs on resulting masonry assemblage strength of grouted prisms. In contrast, the mean masonry assemblage strength of the B150G prisms was significantly higher than those in the A150G series at the 95% confidence level. The reason for this behavior could not be identified. A reduction in CMU web height therefore did not reduce the resulting masonry assemblage strength for grouted prisms. The associated statistical analysis results are presented in Tables 4B-2 and 4B-3 included in Appendix 4B.

Figure 4.6 shows a comparison of the compression test results for grouted prisms constructed using 200 mm CMUs with three different web heights. As opposed to the results for grouted prisms constructed with 150 mm CMUs, the B200G prisms had the lowest mean masonry assemblage strength at 15.8 MPa ($COV = 13.1\%$), while the A200G prisms had the highest mean masonry assemblage strength of 17.2 MPa ($COV = 15.1\%$): a reduction of 8% in the mean assemblage strength in comparison with the A200G prisms. The C200G prisms had a mean masonry assemblage strength of 16.5 MPa ($COV = 5.70\%$) which represented only a 4% reduction in comparison to those in the A200G series. Similar to grouted prisms constructed with 150 mm CMUs, the mean assemblage strength of grouted prisms constructed with 200 mm CMUs did not exhibit a definitive overall trend with the reduction in CMU web height. The COV s were mostly similar to those obtained for the test series of corresponding hollow prisms. This showed that prisms with an h/t ratio equal to 3 produced consistent test results irrespective of whether they were grouted or left hollow, and was attributed to the higher stability provided by end platen restraint and overall flexural rigidity of prisms with a lower h/t ratio ($= 3$) in comparison to those constructed using 150 mm CMUs ($h/t = 4$). The COV s were generally higher than the grouted prisms constructed with 150 mm CMUs. The reason for this could not be identified.

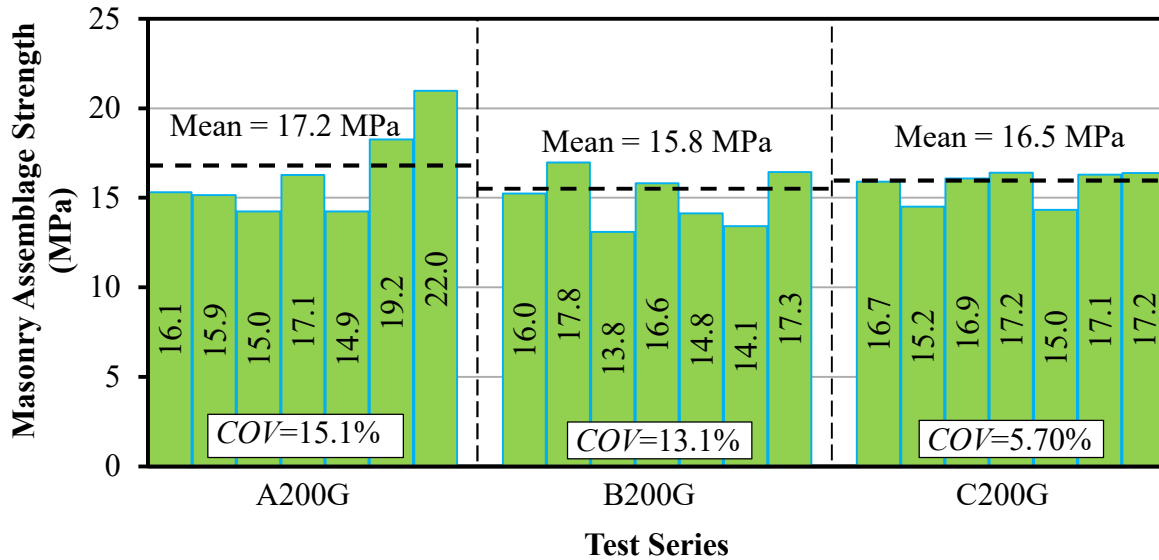


Figure 4.6: Assemblage Strength of Grouted Prisms Constructed with 200 mm CMUs

A one-way ANOVA test was conducted to evaluate whether the resulting masonry assemblage strength of grouted prisms constructed with 200 mm CMUs was significantly influenced by CMU web height. It was found that CMU web height had no significant impact on masonry assemblage strength at the 95% confidence level; therefore, it appears that any type of knock-out unit can effectively be used in grouted prism construction to obtain statistically similar masonry assemblage strength as that of grouted prisms constructed with standard full-height web CMUs. This finding is consistent with grouted prisms constructed using 150 mm CMUs where the reduction in CMU web height did not cause a statistically significant reduction in resulting assemblage strength. The associated statistical analysis results are presented in Table 4B-2 included in Appendix 4B.

Figure 4.7 shows a summary of the mean assemblage strength for all grouted prisms. The masonry assemblage strength for grouted prisms was not greatly influenced by the CMU web height for both CMU sizes. Grout filling all the core space in the prisms including the knockout zones thereby fulfilled the structural role of the web (NCMA, 2012). On the basis of these results, therefore, either CSA A165.1 (CSA, 2014a) knock-out units or ASTM C90 (ASTM, 2011) knock-out units can effectively be used in prism construction to obtain statistically similar masonry assemblage strengths as that of prisms constructed with standard full-height web units, irrespective of the CMU size.

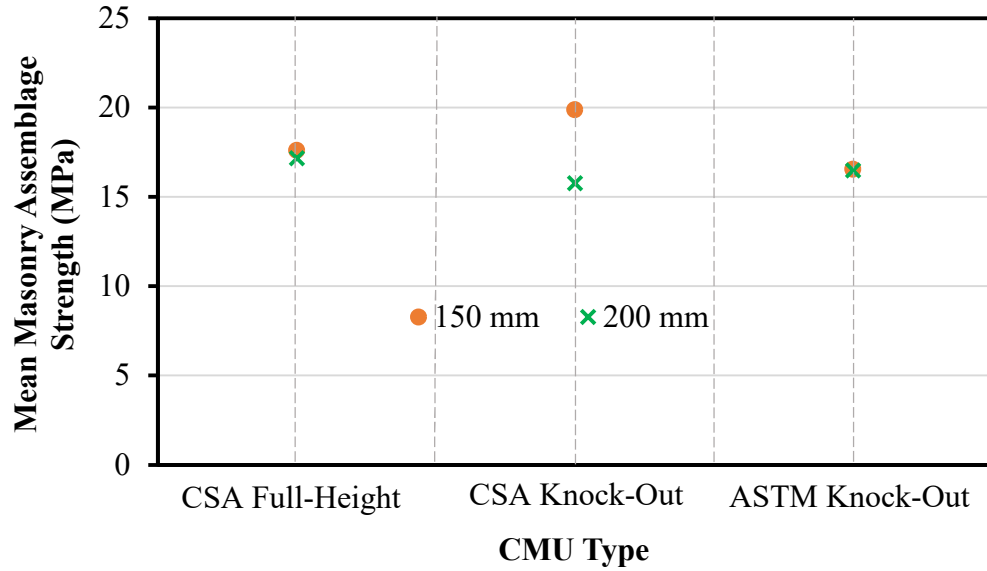


Figure 4.7: Summary of Assemblage Strength for Grouted Prisms

4.2.3 Comparison of Experimental Results with CSA S304-14

Table 4.7 shows the comparison of the experimental and minimum specified masonry compressive strength obtained using the test results and recommendations provided by CSA S304-14 (CSA, 2014b), respectively. Table 4B-4 included in Appendix 4B presents a detailed calculation of these specified masonry compressive strengths. Masonry prisms in different test series were constructed using CMUs of different sizes which resulted in varying h/t ratios across the prism test series. All experimentally obtained masonry assemblage strengths were therefore first normalized using the h/t correction factors as discussed in Section 2.4.4. This was done to eliminate the effect of end platen restraint on prisms, as discussed in Section 2.4.4, and ensured that the resulting normalized values are readily comparable to those specified by CSA S304-14 (CSA, 2014b). The h/t normalized masonry assemblage strengths were then used to establish the experimental specified masonry compressive strengths, f'_{m_expt} , for prisms within each test series as per Clause C.2.2 in CSA S304-14 (CSA, 2014b). The minimum specified masonry compressive strength, f'_{m_CSA} , was obtained using the unit strength approach as specified in Table 4 in CSA S304-14 (CSA, 2014b). Linear interpolation was used whenever required.

Table 4.7: Comparison Between Experimental and Minimum Specified Masonry Compressive Strength

Test Series	f'_{m_expt} (MPa)	f'_{m_CSA} (MPa)	$f'_{m_expt} \geq f'_{m_CSA}$?	Test Series	f'_{m_expt} (MPa)	f'_{m_CSA} (MPa)	$f'_{m_expt} \geq f'_{m_CSA}$?
A150H	19.3		Yes	A150G	15.1		
B150H	9.92	14.5	No	B150G	18.2	11.2	Yes
C150H	8.07		No	C150G	13.9		
A200H	17.5		Yes	A200G	12.9		
B200H	16.8	15.9	Yes	B200G	13.2	12.2	Yes
C200H	9.01		No	C200G	14.9		
A300H	20.3			A300G			
B300H	22.5	11.8	Yes	B300G		N/A	
C300H	17.7			C300G			

Table 4.7 shows that the f'_{m_expt} for hollow prisms constructed using regular stretcher units exceeded the minimum requirement specified by CSA S304-14 (CSA, 2014b) regardless of CMU size. This finding was expected as CSA S304-14 (CSA, 2014b) was developed using the experimental database resulting from a small pool of available literature on prism testing, with prisms predominantly constructed using 200 mm regular stretcher units. Hollow prisms constructed using CMUs with 120 mm tall webs also resulted in similar findings except for those prisms constructed using 150 mm CMUs. Prisms constructed with the smaller CMUs resulted in a lower f'_{m_expt} than the minimum value specified by CSA S304-14 (CSA, 2014b). This was likely the result of a higher COV of 25.8% as discussed in Section 4.2.1. The f'_{m_expt} for hollow prisms constructed using CMUs with 50 mm tall webs did not meet the minimum requirement specified by CSA S304-14 (CSA, 2014b) except for those prisms constructed using 300 mm CMUs. Prisms constructed with larger CMUs resulted in a value of f'_{m_expt} that exceeded f'_{m_CSA} , regardless of the web height of CMUs. This behavior was attributed to the higher lateral stability resulting from the enhancement in overall flexural rigidity of prisms with a lower h/t ratio ($=2$) in comparison to those constructed using smaller sized CMUs. The experimental specified masonry compressive

strength of all grouted prisms, irrespective of the CMU size and type, exceeded the minimum requirement specified by CSA S304-14 (CSA, 2014b).

The resulting masonry assemblage strength for hollow prisms was significantly influenced by web height for all CMU sizes, whereas CMU web height did not influence the masonry assemblage strength of grouted prisms based on the 95% confidence level as was chosen for this study. The use of CMUs with 50 mm tall webs in hollow prisms not only significantly lowered the resulting masonry assemblage strength in comparison with the prisms constructed using regular stretcher units, but also did not meet the minimum strength requirement specified by CSA S304-14 (CSA, 2014b). The following subsection will discuss the failure modes of prisms within different test series based on the data obtained from the DIC system.

4.3 DIC Results and Analysis

A total of five prisms from each test series were evaluated using the DIC system, as described in Section 3.5.1. This was done to investigate the impact of CMU web height on the resulting failure modes of both hollow and grouted masonry prisms subjected to concentric axial compression. Note, however, that this study focused on the relative values of deformation across different test series of prisms rather than the absolute values as obtained using the DIC system. Images captured by the stereo recording systems using the DIC technique, as explained in Section 3.5, were analyzed using the Vic-3D software (version 8, Correlated Solutions). Vic-3D (version 8, Correlated Solutions) is a commercial software that can be used to generate full-field deformation results, including, but not limited, to strain contour and stress versus strain plots, based on the principle of Digital Image Correlation. This section includes a discussion of the principal strain contour maps and axial stress versus principal strain plots generated from the data that were obtained using the DIC system.

4.3.1 Crack Patterns and Failure Modes

Principal strain contour maps on one of the exterior web face and face shell were generated using the Vic-3D software (version 8, Correlated Solutions) to investigate the impact of CMU web height on the crack patterns and resulting failure modes for both hollow and grouted prisms. Failure in masonry prisms is primarily governed by the tensile splitting of the webs as discussed in Section 2.6. This section therefore presents a discussion of failure modes of prisms based on the analysis

of maximum principal strain contour maps generated on one of the exterior web face of prisms. The maximum principal strain contour maps on the exterior web face for all of the individual prisms were obtained from the DIC analysis of the captured images and are shown in Figures 4C-1 to 4C-15 included in Appendix 4C. The maximum principal strain contour maps for prisms constructed using 200 mm CMUs are discussed first as this is the most commonly used CMU size in local masonry construction practice, followed by the discussion for prisms constructed using 150 and 300 mm CMUs. This section also includes an evaluation of the ratio of the applied load at the peak load and initial cracking stage to investigate the load resisting ability of prisms after the occurrence of initial cracking based on the maximum principal strain contour maps.

Figures 4.8 (a), (b), and (c) show the typical maximum principal strain contour maps on an exterior web face for representative hollow prisms from each of test series A200H, B200H, and C200H, respectively, at the initial cracking and peak load states. The variety of colors represent different ranges of maximum principal strain, ϵ_{max} , as shown in the associated legend. Cracks are associated with a high maximum principal strain concentration as represented by the regions of red, orange, and yellow in the given figures. The first vertical crack in the A200H prisms appeared at the bottom center of the exterior web within the middle block course. This crack then propagated in length towards the top and bottom courses and widened as the load increased (Figure 4.8 (a)). The observed cracking pattern was due to the somewhat uniform tensile stresses that developed at the center of the web, as previously discussed in Section 2.3 and shown in Figure 2.2, and was analogous to the mechanism of plates subjected to in-plane tension. Cracks in the B200H prisms initiated in a similar manner to those in the A200H series except that cracks generally propagated diagonally towards the top of the web within the middle block course (Figure 4.8 (b)): a mechanism analogous to beam subjected to non-uniform bending resulting in shear stress. Prisms in test series C200H exhibited initial cracking on the top surface of the web within the middle block course at the web-face shell junction (Figure 4.8 (c)): a mechanism analogous to that which would occur for a shallow fixed-fixed beam with negative bending moment at the supports. These cracks also appeared within top and bottom block courses as the load increased. The occurrence of vertical cracks shifted from the center of the web towards the web-face shell junction as the web height of CMUs decreased and was due to the stress concentration at the corners of knockout webs, caused by face shell bending, which increased with increasing knockout height. Crack patterns as

observed confirmed that the predominant mode of failure of hollow prisms constructed using 200 mm CMUs was tensile splitting of webs, although crack patterns varied with web height.

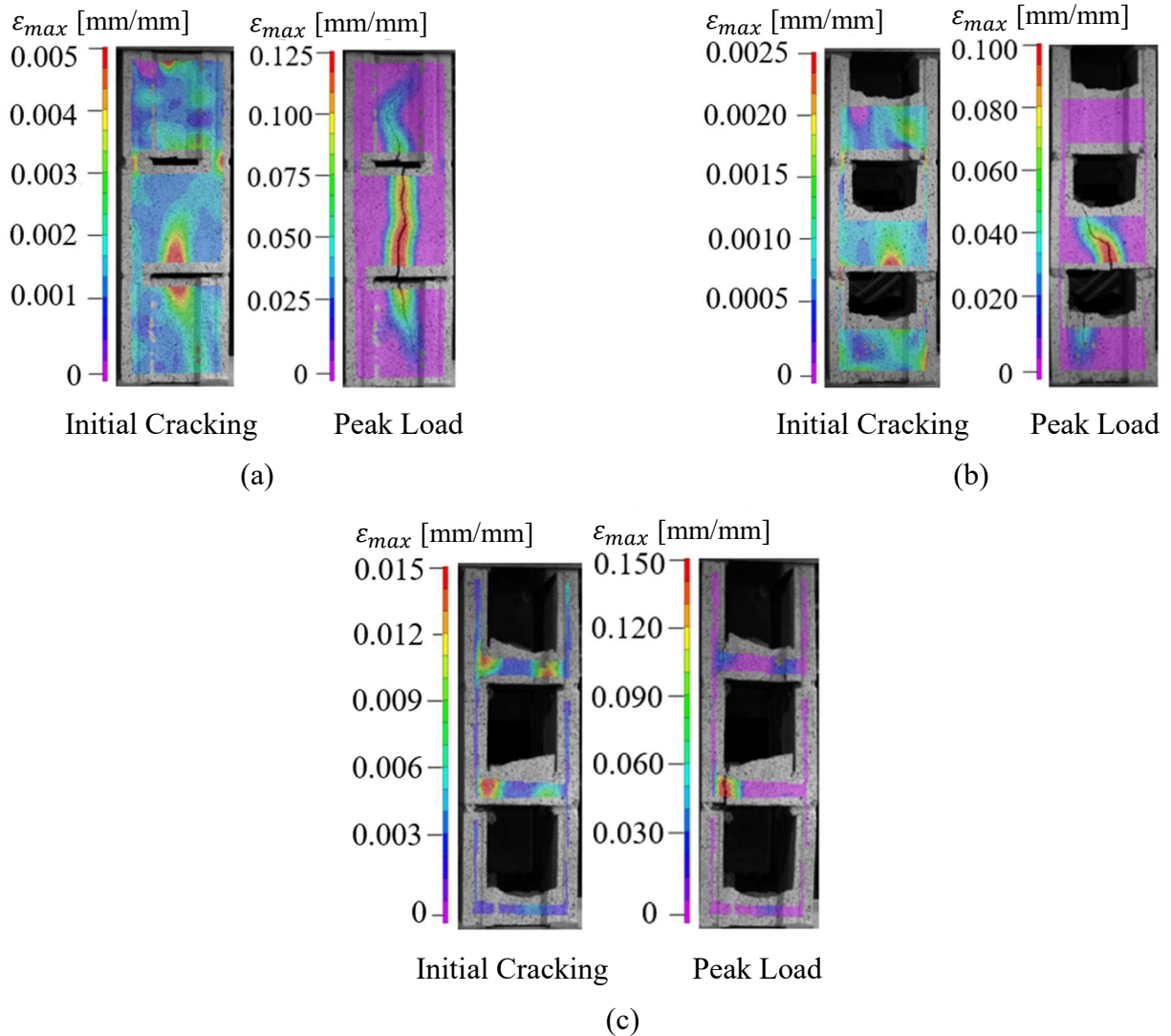


Figure 4.8: Typical Initial Cracking and Peak Load States for a Hollow Prism within Test Series: (a) A200H, (b) B200H, and (c) C200H

Figures 4.9 (a), (b), and (c) show the typical maximum principal strain, ϵ_{max} , contour maps on an exterior web for representative hollow prisms from each of test series A150H, B150H, and C150H, respectively, at the initial cracking and peak load states. Maximum principal strain contour maps for hollow prisms constructed with 150 mm CMUs mostly exhibited similar crack patterns to those constructed with 200 mm CMUs. Failure was therefore caused by the tensile splitting of the webs which started within the middle block course. This similarity was likely the result of prisms in both

groups having a height-to-thickness (h/t) ratio greater than 3 which is a minimum requirement in CSA S304-14 (CSA, 2014b) for prisms to exhibit the failure as would be expected in full-scale masonry walls.

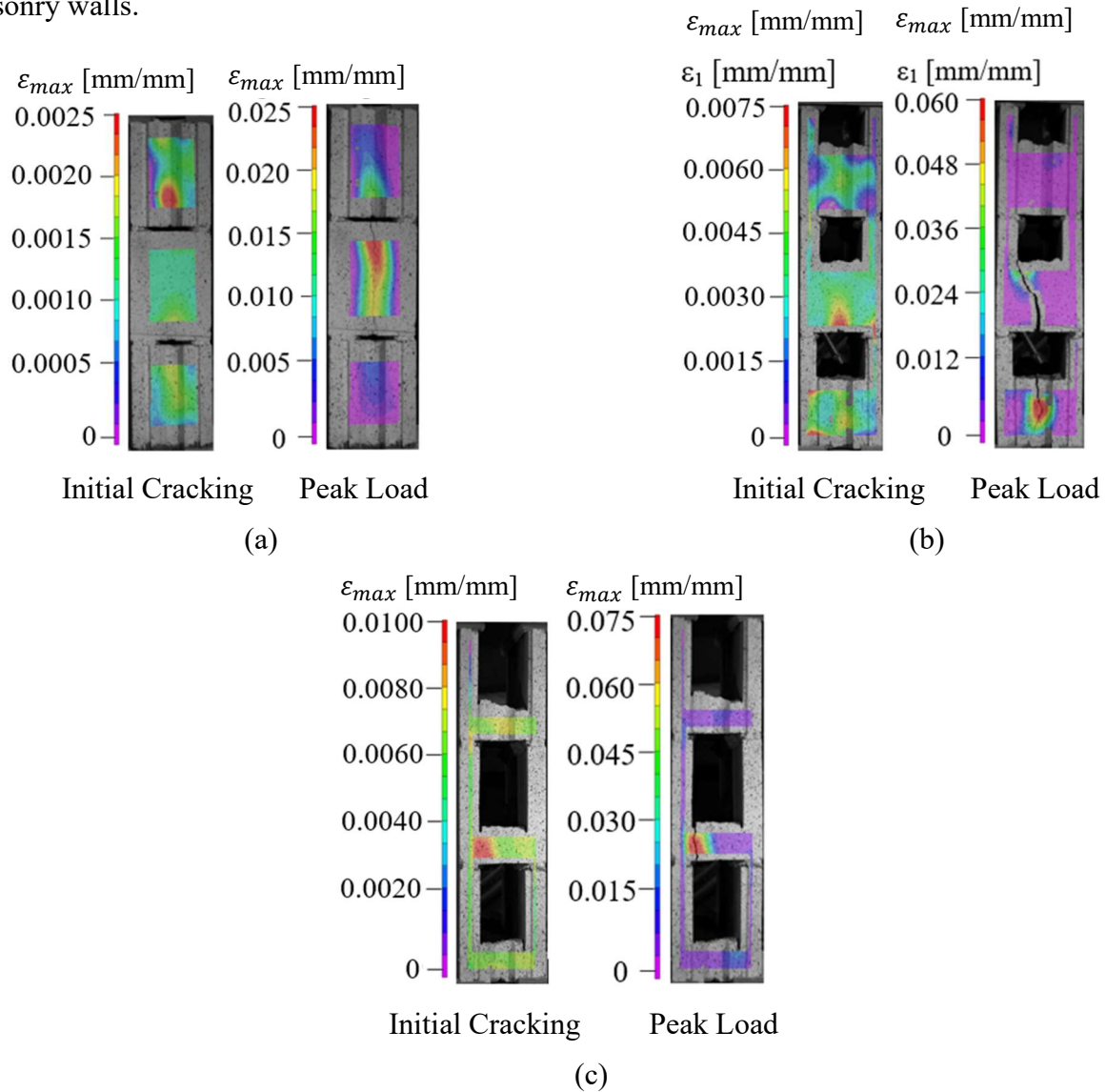


Figure 4.9: Typical Initial Cracking and Peak Load States for a Hollow Prism within Test Series: (a) A150H, (b) B150H, and (c) C150H

Figures 4.10 (a), (b), and (c) show the typical maximum principal strain, ϵ_{max} , contour maps on an exterior web face for representative hollow prisms from each of test series A300H, B300H, and C300H, respectively, at the initial cracking and peak load states. The hollow prisms constructed using 300 mm CMUs (h/t ratio = 2.03) experienced somewhat different crack patterns as compared to those constructed using either 150 or 200 mm CMUs. The A300H prisms (Figure 4.10 (a))

experienced diagonal cracks on their exterior webs similar to the B200H prisms. These cracks did not lengthen or widen as the load increased and resulted in a sudden failure. This behavior of prisms with a lower h/t ratio ($=2$), as compared to those with h/t ratio of either 3 or 4, was attributed to the influence of artificial confinement stresses resulting from the differences in stiffness between the CMU and steel platen at the top and bottom surfaces of the prism. Hollow prisms constructed with 300 mm CMUs with knockout webs (i.e., test series B300H & C300H as shown in Figures 4.10 (b) & (c), respectively) experienced narrow cracks at the web-face shell junction within the middle and top courses resulting in a sudden failure. The bottom course of all prisms remained reasonably intact.

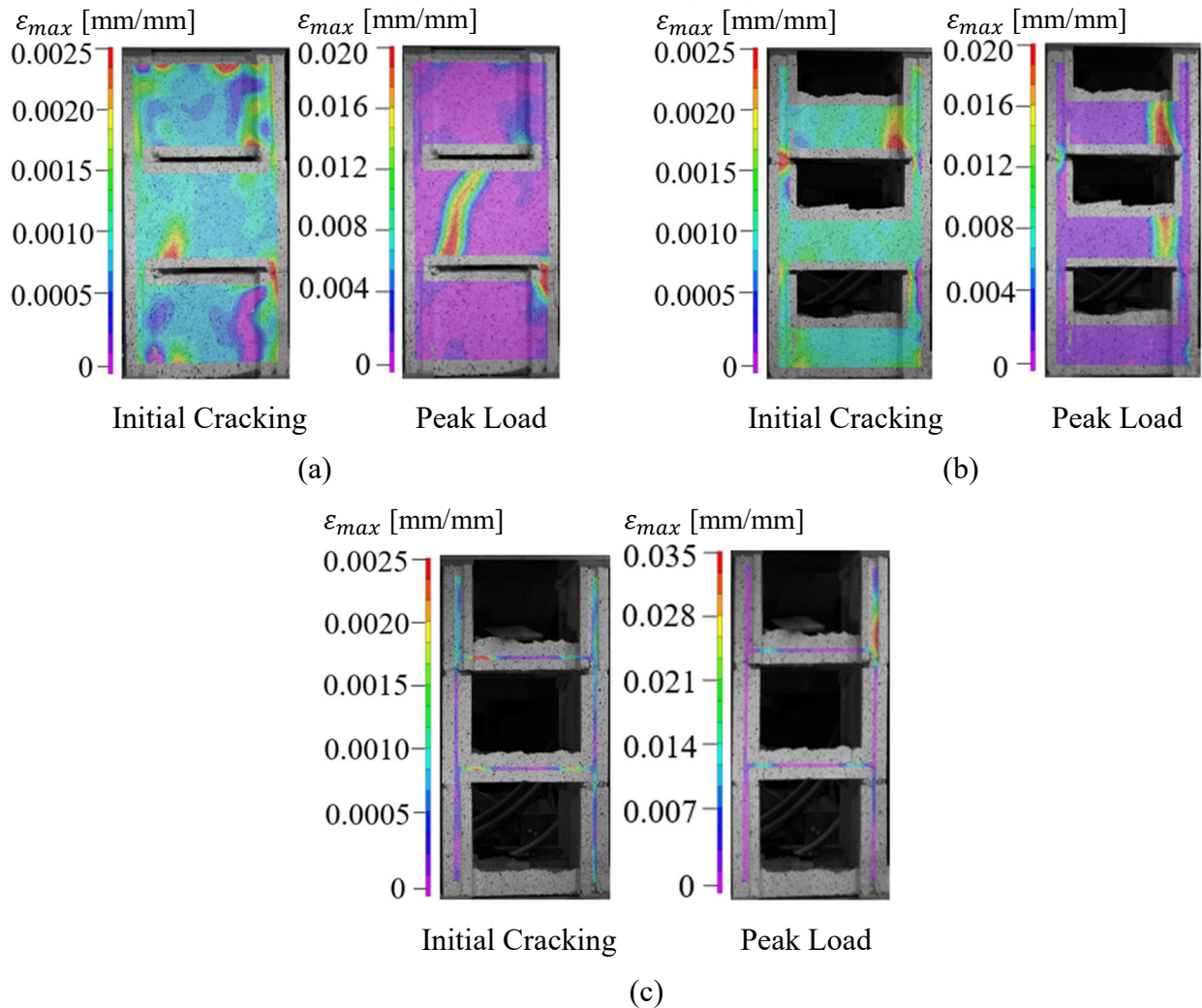


Figure 4.10: Typical Initial Cracking and Peak Load States for a Hollow Prism within Test Series: (a) A300H, (b) B300H, and (c) C300H

Figures 4.11 (a), (b), and (c) show the typical maximum principal strain, ε_{max} , contour maps on the exterior web face for representative grouted prisms from each of test series A200G, B200G, and C200G, respectively, at the initial cracking and peak load states. Cracks in prisms within test series A200G (Figure 4.11 (a)) mostly initiated and propagated in a similar fashion to those within test series A200H, analogous to a mechanism discussed in Section 2.3. In contrast, cracks in the B200G (Figure 4.11 (b)) and C200G prisms (Figure 4.11 (c)) initiated in knockout region along face of face shell and then propagated across the remaining web within the middle block course before extending to the top and bottom courses as the load increased. The grout in these prisms provided additional structural integrity resulting in grout-block interface being the only vulnerable location. In contrast with the observations made for hollow prisms, crack widths in all grouted prisms did not appear to increase with increasing applied load. This resulted in a sudden failure of grouted prisms and was potentially due to: the additional pressure exerted by the grout on the CMUs due to the difference in their elastic properties, the enhanced structural stability provided by the grout column against the potential buckling of the prisms, and sharing of the applied load between the grout and CMU that reduced the stress concentration on the exterior webs in comparison with corresponding hollow prisms.

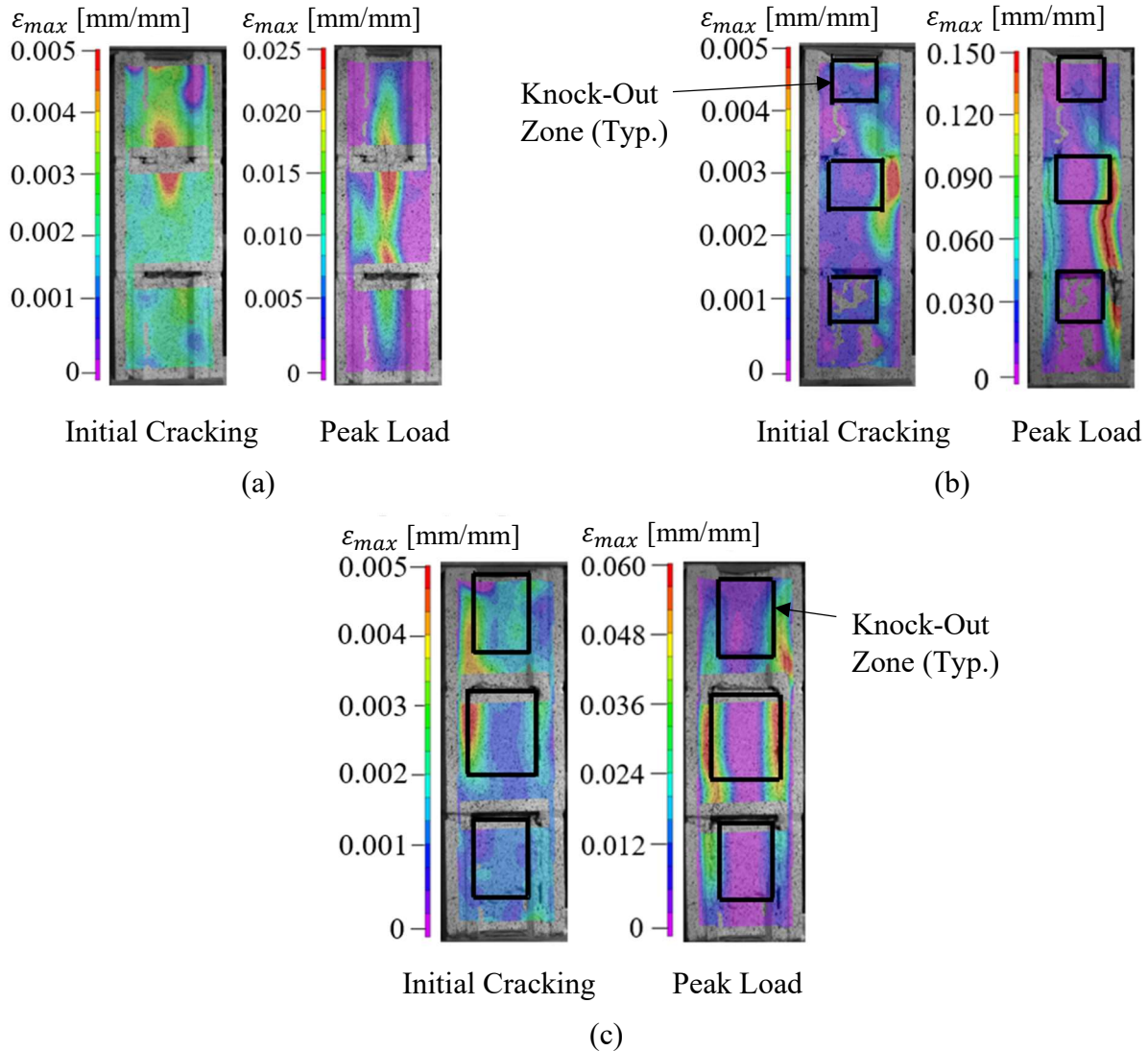


Figure 4.11: Typical Initial Cracking and Peak Load States for a Grouted Prism within Test Series: (a) A200G, (b) B200G, and (c) C200G

Figures 4.12 (a), (b), and (c) show the typical maximum principal strain, ϵ_{max} , contour maps on an exterior web face for representative grouted prisms from each of test series A150G, B150G, and C150G, respectively, at the initial cracking and peak load states. The crack patterns for grouted prisms constructed with 150 mm CMUs were similar to those experienced by grouted prisms constructed with 200 mm CMUs. The explanations related to the difference in the cracking patterns in prisms across test series A150G, B150G, and C150G are same as those previously discussed for grouted prisms constructed with 200 mm CMUs.

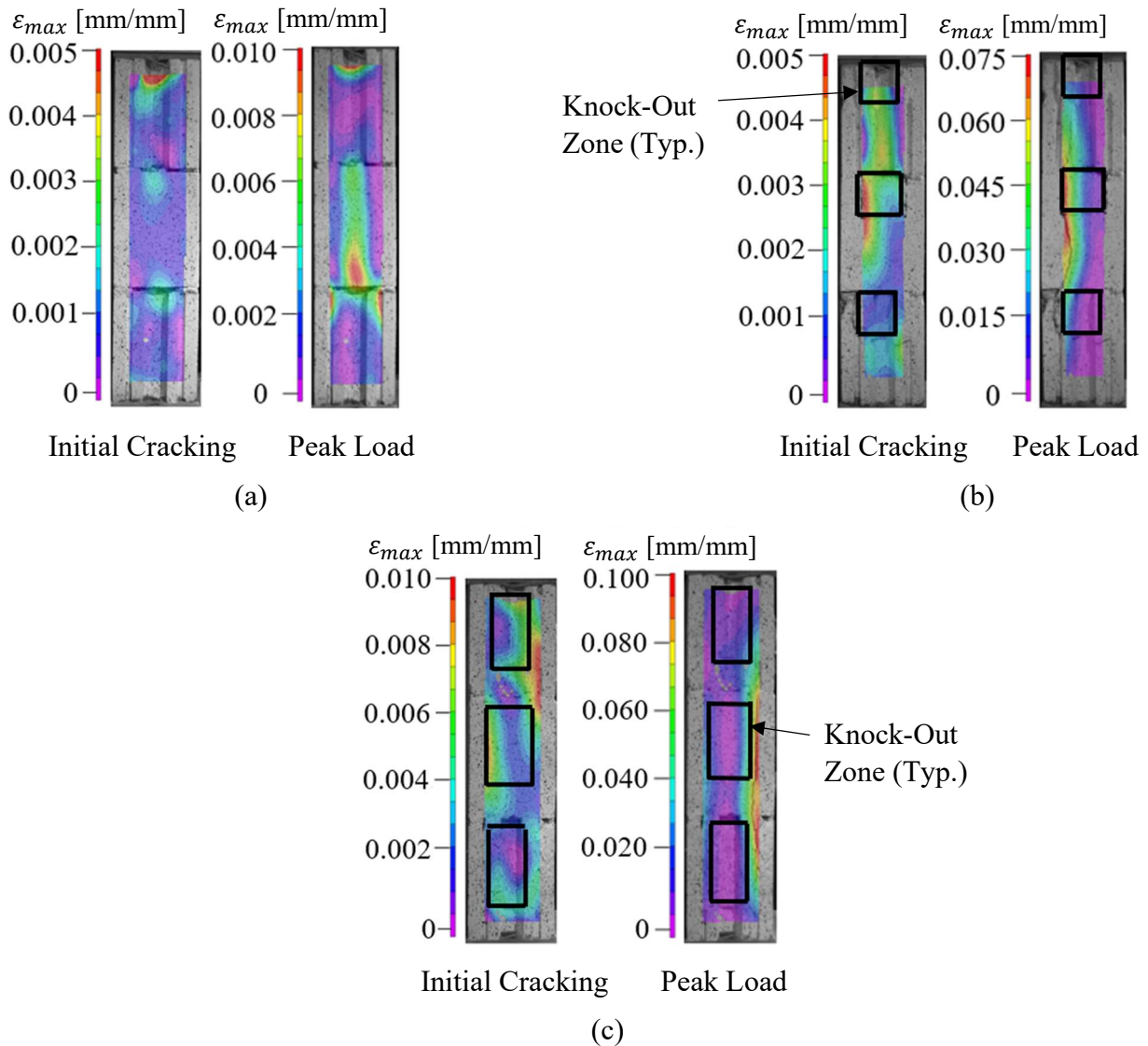


Figure 4.12: Typical Initial Cracking and Peak Load States for a Grouted Prism within Test Series: (a) A150G, (b) B150G, and (c) C150G

The maximum principal strain contour maps were further evaluated to identify the location of initial cracking within an exterior web face and corresponding level of applied load, and the subsequent crack propagation until failure. Table 4.8 shows the average resulting masonry assemblage strength, \bar{f}_m ; the average applied load at initial cracking, P_{cr} , stage; the average peak load, P_{max} , at failure; and the ratio P_{max}/P_{cr} for prisms in each test series. The initial cracking load for each prism was established based on the initial appearance of a high maximum principal strain, ϵ_{max} , concentration in the strain contour maps generated by the DIC system rather than by visual observations made during testing. The peak load was the maximum load resisted by each prism

before failure. The P_{max}/P_{cr} ratio represents the load resisting ability of the prism after the occurrence of initial cracking. This ratio increased with increasing web height of CMUs for both hollow and grouted prisms constructed with 200 mm CMUs. A proportional relationship therefore existed. The P_{max}/P_{cr} ratios for grouted prism series were lower than those for the corresponding hollow prisms series constructed with 200 mm CMUs except for the C200G prisms which resulted in a higher P_{max}/P_{cr} ratio in comparison to those in the C200H series. The grouted prisms constructed with 200 mm CMUs generally exhibited a more sudden failure after the appearance of initial cracking in comparison to the corresponding hollow prisms due to the additional pressure exerted by the grout column on the CMUs as a result of difference in the Poisson's ratio of the CMUs and grout as was discussed in the Section 2.3. The P_{max} and P_{cr} results for all of the individual prisms are reported in Table 4C-1 as included in Appendix 4C.

Table 4.8: Initial Cracking and Peak Load for Prisms within Different Test Series

Test Series	\bar{f}_m (MPa)	COV (%)	P_{cr} (kN)	COV (%)	P_{max} (kN)	COV (%)	P_{max}/P_{cr}
A150H	23.7	9.06	276	19.0	511	11.1	1.85
B150H	18.5	25.8	270	26.0	350	22.6	1.30
C150H	17.6	30.5	282	30.1	366	33.0	1.30
A200H	25.2	13.0	336	15.9	678	14.8	2.02
B200H	23.7	12.2	362	14.4	598	10.9	1.65
C200H	13.8	15.6	291	20.0	339	15.0	1.17
A300H	27.7	7.27	659	17.4	857	9.33	1.30
B300H	28.6	3.82	599	11.6	890	4.50	1.49
C300H	24.5	7.78	369	20.5	768	8.40	2.08
A150G	17.6	8.70	649	23.5	900	11.3	1.39
B150G	19.9	5.32	748	8.56	1030	5.36	1.38
C150G	16.5	9.77	642	20.2	872	9.89	1.36
A200G	17.2	15.1	686	17.3	1110	5.81	1.62
B200G	15.8	13.1	747	17.1	1080	10.4	1.45
C200G	16.5	5.70	863	8.79	1130	8.13	1.31

Table 4.8 shows that the P_{max}/P_{cr} ratio for both hollow and grouted prisms constructed with 150 mm CMUs mostly exhibited similar trends to that of prisms constructed with 200 mm CMUs and was likely the result of similar crack patterns and failure modes as previously discussed. Table 4.8 also shows that the P_{max}/P_{cr} ratio for hollow prisms constructed with 300 mm CMUs increased with a reduction in web height. No identifiable trend was found across different CMU sizes.

The analysis of maximum principal strain contour maps on the exterior web face of prisms revealed that the crack patterns and the resulting failure modes of both hollow and grouted prisms mostly varied with CMU web height for all CMU sizes. However, tensile splitting as observed on the exterior web generally governed the failure in all prisms regardless of the CMU web height, size, or the presence of grout. The ratio of the recorded peak and cracking load, P_{max}/P_{cr} , revealed that the load resisting capacity of both hollow and grouted prisms after the occurrence of initial cracking was primarily influenced by the web height of CMUs used in prism construction and varied across the CMU sizes.

4.3.2 Stress versus Strain Characteristics

Axial stress versus principal strain plots on one exterior web face and face shell were also generated using the data obtained from the analysis of DIC images in Vic-3D software (version 8, Correlated Solutions) to investigate the impact of CMU web height on the resulting failure modes for both hollow and grouted prisms. Full-field analysis of the captured images of masonry prisms in Vic-3D software (version 8, Correlated Solutions) generated the maximum, ϵ_{max} , and minimum, ϵ_{min} , principal strains on one exterior web face and face shell of prisms. Axially applied load at different stages was divided by the net cross-sectional area of the prism to obtain the corresponding axial stress values. These values were plotted against the ϵ_{max} , and ϵ_{min} , obtained as previously discussed, to generate the corresponding axial stress versus principal strain plots for each prism. Figures 4C-16 to 4C-30 as included in Appendix 4C shows the axial stress versus principal strain plots for all of the individual prisms, whereas the following paragraphs present a discussion of the typical axial stress versus principal strain plot for prisms within each test series. Plots for prisms constructed using 200 mm CMUs are discussed first as this is the most commonly used CMU size in local masonry construction practice, followed by the discussion for prisms constructed using 150 and 300 mm CMUs, respectively.

Figures 4.13 (a) and (b) show typical axial stress versus principal strain plots for one exterior web and face shell, respectively, for a representative hollow prism within each of the three test series A200H, B200H, and C200H. The minimum principal strain, ϵ_{min} , was always compressive and so was plotted along the negative horizontal axis while the maximum principal strain, ϵ_{max} , was tensile in all instances and was plotted along the positive horizontal axis. Figures 4.13 shows that the minimum principal strain on the face shell had the comparatively highest magnitude of all four strains until the prism approached failure, at which point there was an abrupt increase in maximum principal strain within the exterior web face. Compression of mortar within the bed joints, given that it is softer than the CMUs, contributed to the higher value of minimum principal strain on the face shell. The sudden increase in maximum principal strain within the exterior web face was attributed to extensive vertical cracks that developed on the web face as the prism approached failure (as observed in the corresponding maximum principal strain contour map included in Section 4.3.1). This sudden change in slope represented the transition between the uncracked and cracked behavior of the prism. The form of the curves observed in Figures 4.13 (a) and (b) suggest that the failure mode of hollow prisms constructed using 200 mm CMUs was due to the tensile splitting of the webs, irrespective of CMU web height. No cracking was observed to have occurred on the face shells.

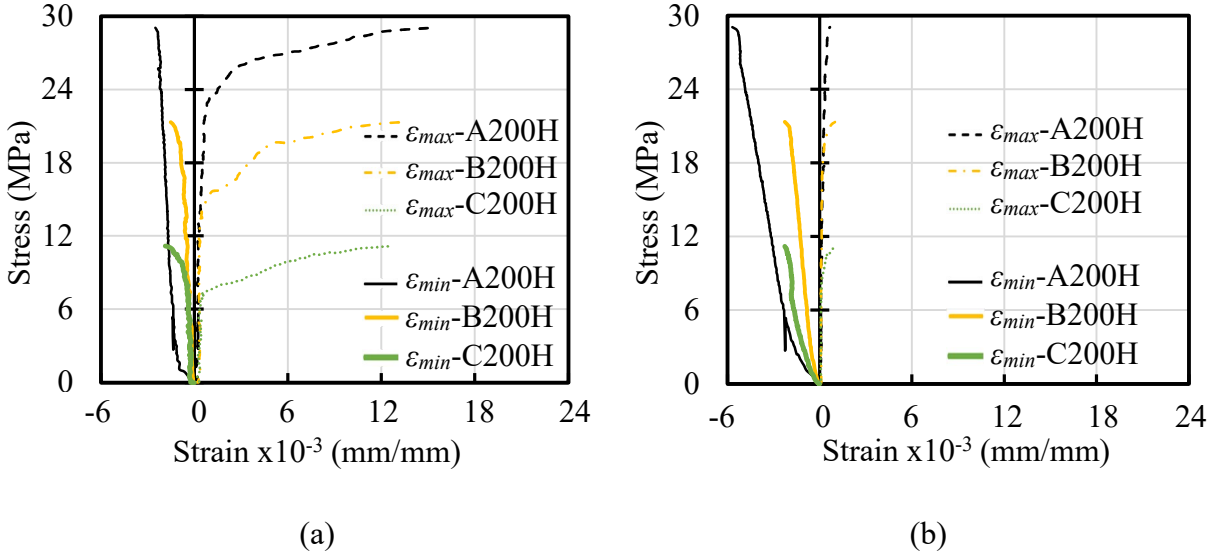


Figure 4.13: Typical Axial Stress versus Principal Strain Plot for Prisms within Test Series A200H, B200H, and C200H on: (a) Exterior Web Face, and (b) Face Shell

Axial stress versus principal strain plots for hollow prisms constructed with 150 mm CMUs were generated only for the exterior web face since the face shells of these prisms were too fragile to paint with a roller brush. Figure 4.14 shows that axial stress versus principal strain plots on the exterior web face for hollow prisms constructed with 150 mm CMUs were mostly similar to those constructed with 200 mm CMUs. Prisms within test series A150H, B150H, and C150H also failed due to the occurrence of vertical cracks on webs. This similarity was likely the result of h/t ratio being greater than 3.0 for both the prism groups constructed with 150 and 200 mm CMUs as explained in Section 4.3.1.

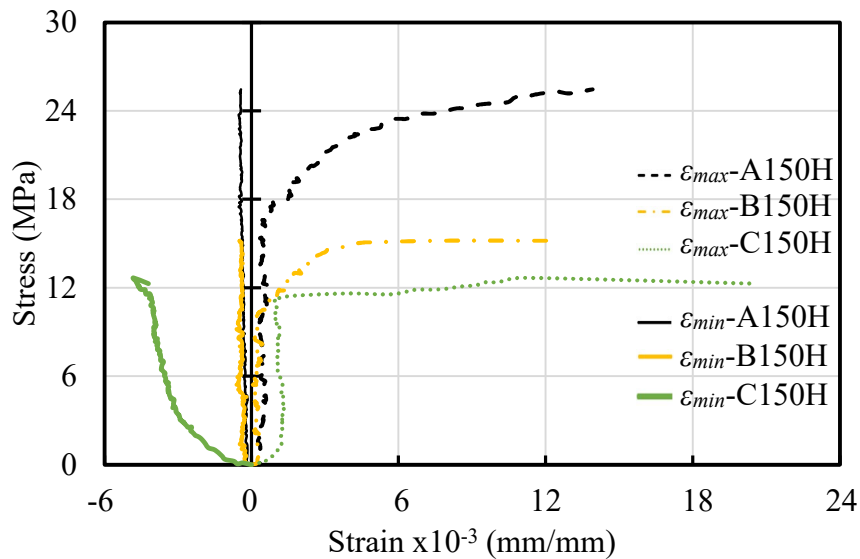


Figure 4.14: Typical Axial Stress versus Principal Strain Plot for Prisms within Test Series A150H, B150H, and C150H on the Exterior Web Face

Figures 4.15 (a) and (b) show typical axial stress versus principal strain plots for one exterior web and face shell, respectively, for a representative hollow prism within each of the three test series (A300H, B300H, and C300H). Hollow prisms constructed with 300 mm CMUs were found to have a somewhat different form of their axial stress versus principal strain curves in comparison to those constructed with either 150 or 200 mm CMUs. The minimum principal strain, ϵ_{min} , on the exterior web face and face shell had a comparatively higher magnitude than maximum principal strains throughout loading that increased gradually until failure occurred. There was also a small increase in maximum principal strain, ϵ_{max} , within the exterior web face as the prism approached failure, and was due to the appearance of small vertical cracks on the exterior web face (as observed

in the corresponding maximum principal strain contour maps included in the Section 4.3.1). The forms of the curves, as discussed previously, supported the findings from the corresponding maximum principal strain contour map that the vertical cracks which appeared on the exterior web face did not lengthen or widen as much as they did in prisms constructed with either 150 or 200 mm CMUs. This behavior was attributed to the influence of artificial confinement stresses resulting from the differences in stiffness between the CMU and steel platen at the top and bottom surfaces of prism with a lower h/t ratio ($=2$) in comparison to those constructed using CMUs of smaller sizes.

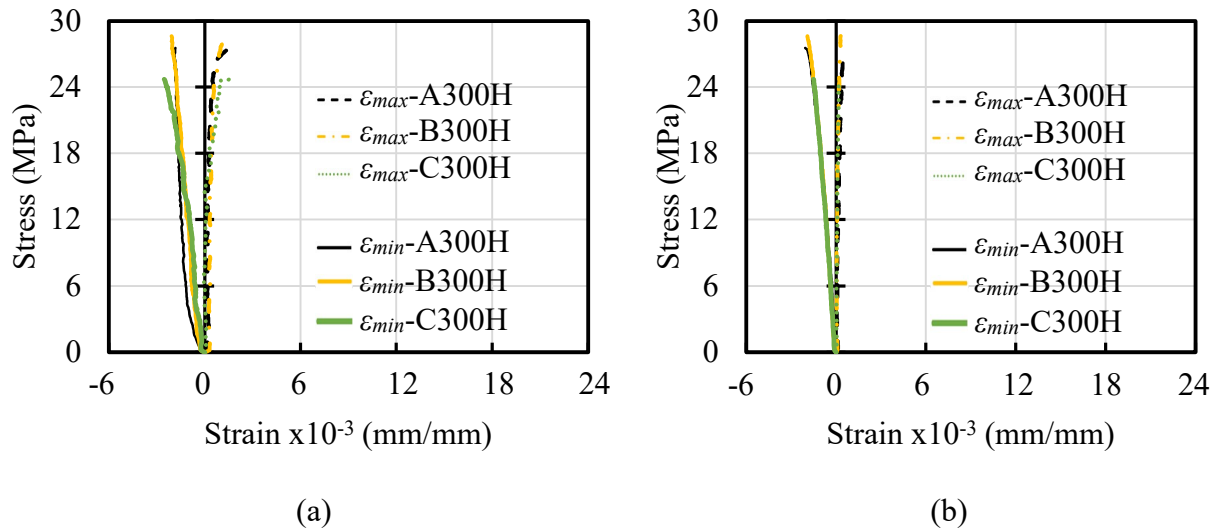


Figure 4.15: Typical Axial Stress versus Principal Strain Plot for Prisms within Test Series A300H, B300H, and C300H on: (a) Exterior Web Face, and (b) Face Shell

Figures 4.16 (a) and (b) show typical axial stress versus principal strain plots on one exterior web face and face shell, respectively, for representative grouted prisms from each of the test series A200G, B200G, and C200G. Figures 4.16 shows that the minimum principal strains, ϵ_{min} , on the exterior web face and face shell increased gradually until the prism approached failure, at which point there was a sudden increase in the maximum principal strain, ϵ_{max} , on the web face. This was due to the appearance of vertical tensile cracks on the exterior web face prior to failure (as observed in the corresponding maximum principal strain contour maps included in the Section 4.3.1). The forms of the curves for grouted prism constructed with 200 mm CMUs were similar to those of corresponding hollow prisms and so suggested the occurrence of tensile cracks on the exterior webs.

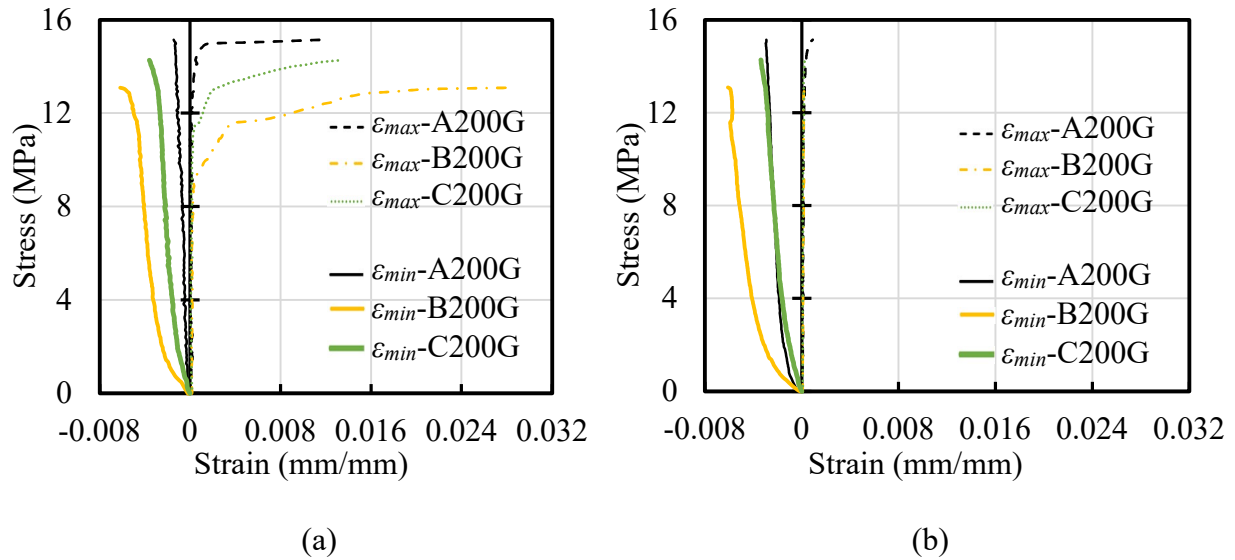


Figure 4.16: Typical Axial Stress versus Principal Strain Plot for Prisms within Test Series A200G, B200G, and C200G on: (a) Exterior Web Face, and (b) Face Shell

Figures 4.17 (a) and (b) show typical axial stress versus principal strain plots on one exterior web face and face shell, respectively, for representative grouted prisms from each of the test series A150G, B150G, and C150G. Axial stress versus principal strain curves in both the figures were mostly similar to those for grouted prisms constructed with 200 mm CMUs. The explanations attributed to the various axial stress versus principal strain curves as included in Figures 4.17 (a) and (b) are therefore the same as those previously discussed for grouted prisms constructed with 200 mm CMUs. Failure was therefore found to be governed by vertical tensile cracking on the exterior webs. This finding is in good agreement with those obtained from the corresponding maximum principal strain contour maps. Similar behavior was also observed for the corresponding hollow prism test series.

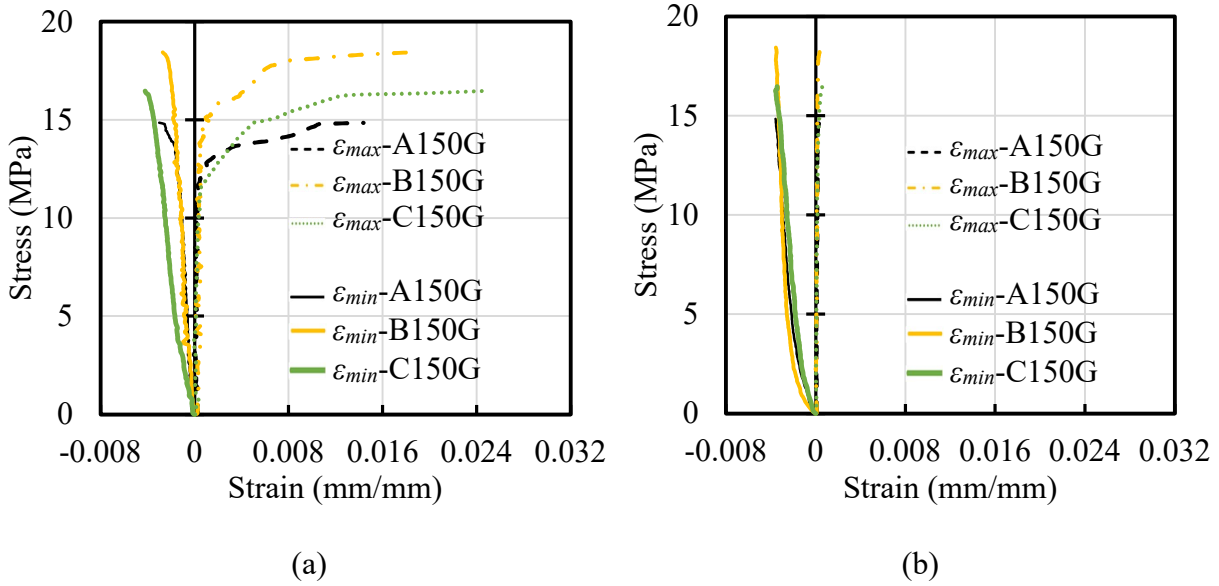


Figure 4.17: Typical Axial Stress versus Principal Strain Plot for Prisms within Test Series A150G, B150G, and C150G on: (a) Exterior Web Face, and (b) Face Shell

Axial stress versus principal strain plots on one exterior web face and face shell, shown in Figures 4.13 to 4.17, showed that the tensile splitting of the webs primarily governed the failure in both hollow and grouted prisms loaded under concentric compression, irrespective of the web height or size of CMUs. This finding is similar to those as discussed in Section 2.6. A good agreement in findings obtained from the maximum principal strain contour maps and axial stress versus principal strain plots suggested that the axial stress versus principal strain plots generated from the DIC results effectively captured the mechanical behavior of masonry prisms subjected to concentric axial load.

4.4 FEM Analysis and Results

A finite element modeling (FEM) approach was adopted to obtain detailed stress distributions on an exterior web face of prisms and evaluate their potential failure modes. The impact of CMU web height on the peak load, P_{max} , was not included as it would have involved a complex analysis that required a complete set of material properties such as: Young's modulus of elasticity and ultimate tensile strength, which were not measured in this study. Three prism models representing each of three test series A200H, B200H, and C200H were considered. Only hollow prism test series were included as there has been no consensus on the failure modes for the grouted prisms as was

discussed in Section 2.6. The analysis was also limited to prisms constructed using 200 mm CMUs as this is the most commonly used size in Canadian masonry construction practice. The geometry of CMUs used in developing the full-scale prism models was defined using the standard dimensions from the product specification provided by the manufacturer. The geometry of all modeled prisms was similar to the actual prisms that were tested in the laboratory and represented standard masonry construction practice in Canada. The three model types had the same CMU and mortar strength as reported in Table 4.9; thus the CMU web height was the only parameter affecting the analysis results.

A linear three-dimensional elastic finite element model was developed using ANSYS Workbench (ANSYS Inc., Release 18.1) as this model is the simplest way to capture the behavior of brittle materials using tensile strength, σ_t , as a rupture criterion. Non-linear modeling was not considered as it is highly complex and involves a tabular input of the material properties of all constituent materials that were not measured during the experimental investigation. Tetrahedral elements with 4 nodes, and so 4 sides, were used to develop the full-scale model that represented a three-course tall prism. This element type can fit better in the model to represent the complex geometry of the resulting prism (i.e., rounded corners and tapered CMU components as shown in Figure 4.18). A mesh with elements that included 15 mm long sides was used for CMUs, whereas the mortar was meshed with elements that had 5 mm long sides. The size of the mesh was determined using an iterative process where the mesh size was reduced until the difference between the consecutive analysis results was less than one percent. Perfect bond was assumed at the interfaces between CMUs and the mortar. A total of 20 different contact surfaces between the CMU and mortar layer for each prism model were automatically defined by the software. The models were developed using the boundary and loading conditions similar to those under actual laboratory testing conditions. This was achieved by restraining the displacements of the face shells in all three directions within the bottom course and by applying the axial load on both of the face shells within the top course.

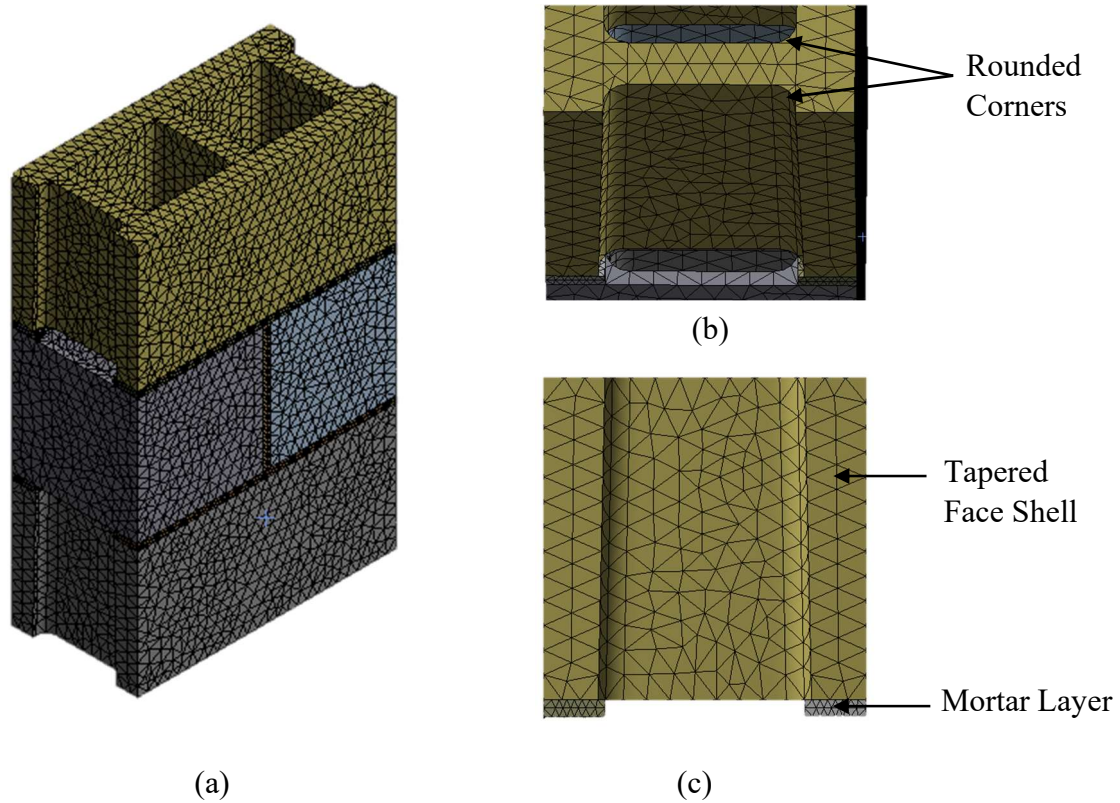


Figure 4.18: Geometry of Finite Element Prism Model: (a) Typical Masonry Prism Model, (b) Rounded Geometry at the Corners, and (c) Tapered Face Shell Geometry

Table 4.9 shows the material properties that were used to develop the finite element models. The densities of the CMUs and mortar were obtained from the CMU absorption test results and the volume proportion used for mortar preparation, respectively, as reported in Sections 4.1.1 and 3.4.1. The deformation characteristics of the CMUs and mortar cubes were not measured experimentally; as a result the as-tested value of Young’s Modulus of Elasticity for the constituent materials could not be established. The values for Young’s Modulus of Elasticity, Poisson’s ratio, compressive strength, and tensile strength were therefore obtained from the data reported in the literature (Santos et al., 2017). The same material properties were assigned to all prism models.

Table 4.9: Mechanical Properties of Materials Used for Finite Element Modeling

	Density (kg/m ³)	Young's Modulus of Elasticity (MPa)	Poisson's Ratio	Compressive Strength (MPa)	Tensile Strength (MPa)
CMU	2270	35500	0.20	35.4	3.23
Mortar	1230	9290	0.25	11.8	1.97

Each prism model was loaded to the average P_{max} for the corresponding test series as obtained from laboratory testing. The desired outputs were selected (i.e., maximum, σ_{max} , and minimum, σ_{min} , principal stresses) and the analysis was conducted. Only the maximum principal stress distributions are presented in this study as failure in hollow masonry prisms was mainly governed by the tensile splitting of the webs as discussed in Section 4.3. Figure 4.19 shows the maximum principal stress, σ_{max} , distribution resulting from the FEM analysis for prisms within test series A200H (Figure 4.19 (a)), B200H (Figure 4.19 (b)), and C200H (Figure 4.19 (c)). The variety of colors represents different ranges of σ_{max} as shown in the associated legend. The tensile strength, σ_t , of CMUs was manually set on the legend to separate the red color from orange so that any material that is colored red indicated failure. Similarly, the orange color indicated that the material was approaching failure. Prism models were loaded well above the tensile strength of the CMU so that a distinctive failure was obtained in the webs within each block course. This was possible due to the use of linear elastic model which allows for stress results beyond the tensile strength.

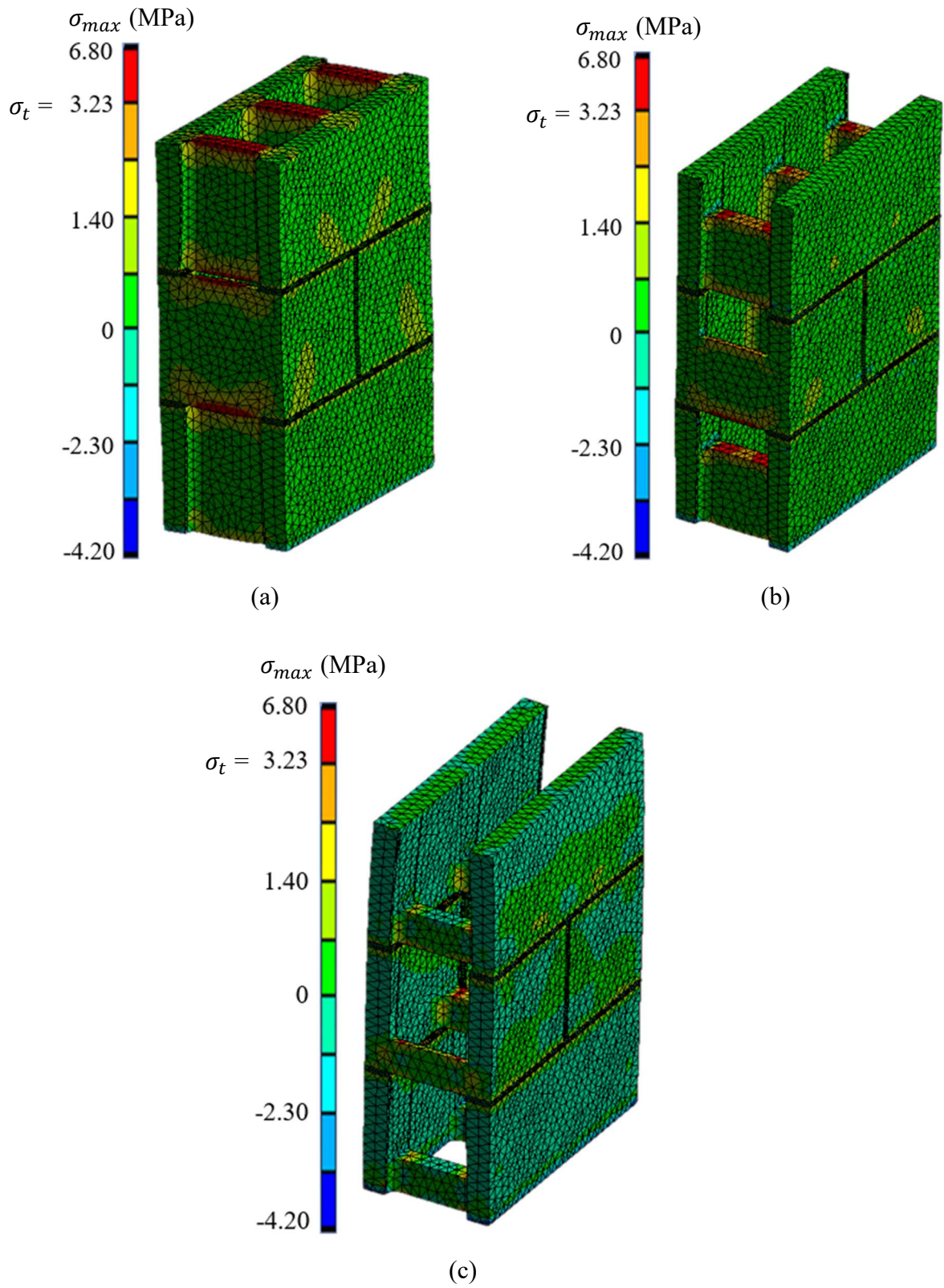
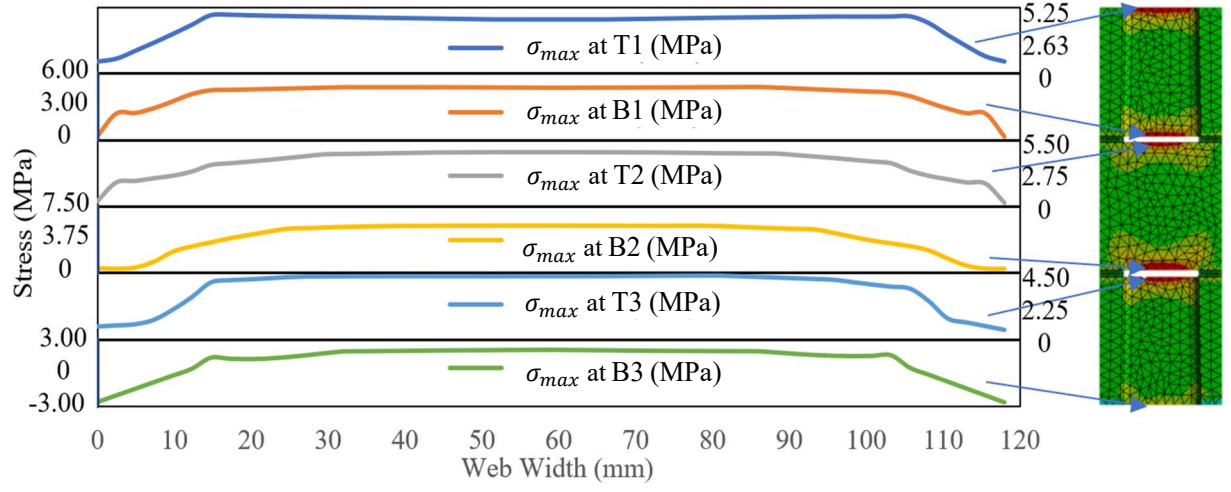


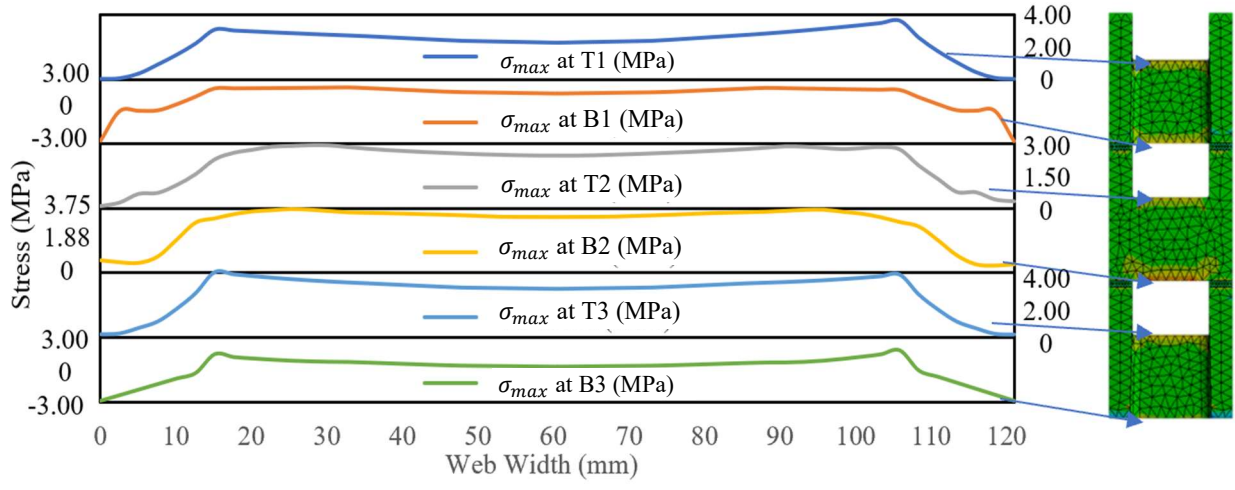
Figure 4.19: Maximum Principal Stress Contour Map for Prisms within Test Series: (a) A200H, (b) B200H, and (c) C200H

The maximum principal stress, σ_{max} , distribution was obtained along the top and bottom of the exterior webs to investigate the potential impact of CMU web height on the resulting failure modes. The top and bottom web surfaces of the CMU in each of the three block courses were provided with a unique identification. The first term in the identification denotes the top or bottom surface in the web (T - top and B - bottom); and the second term represents the block course (1 - top, 2 - middle, and 3 - bottom). For example, T1 represents the top surface of the exterior web within the top block course. Complete FEM results are presented in Tables 4D-1 to 4D-3 as included in Appendix 4D.

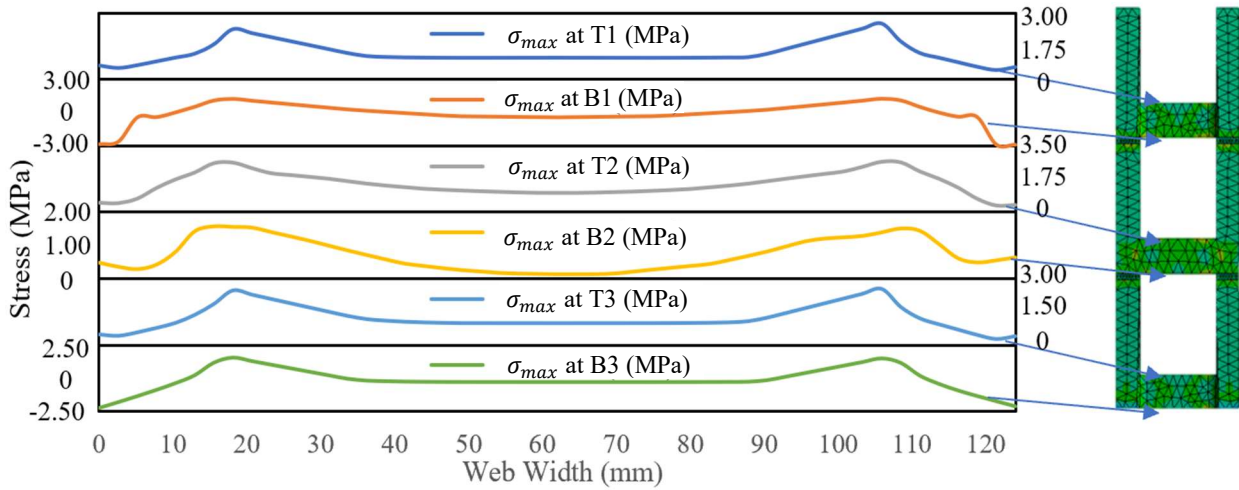
Figures 4.20 (a), (b), and (c) show the plots of maximum principal stress distribution along the top and bottom surface of the web within each block course for the A200H, B200H, and C200H test series, respectively. Figures were plotted to different scales to properly capture the forms of maximum principal stress distribution at the top and bottom web surfaces rather than to emphasize the magnitudes of stress as these are different for different prism models. The locations of possible cracks were identified by the concentration of maximum principal stress in the plots. Figure 4.20 (a) shows that the maximum principal stress was generally uniform and exhibited its maximum value at the center of the webs within the top and bottom surfaces for prisms in the A200H test series. This form of the curves indicated that cracks were most likely to appear vertically at the center of the web along the prism height and ultimately caused their failure. Figure 4.20 (b) shows that, for prisms in test series B200H, the maximum principal stress was distributed non-uniformly, with its highest magnitude being at different locations within a region between the center of the web and web-face shell junction for different block courses. The form of the curves therefore indicated the possibility of diagonal crack formation on the exterior webs between the center of the web and the web-face shell junction for prisms in test series B200H. Figure 4.20 (c) shows that, for prisms in test series C200H, the maximum principal stress attained its peak value in a region near the web face shell junction at the top and bottom surfaces of web within all block courses. This indicated that prisms in test series C200H were most likely to exhibit vertical tensile cracks near web-face shell junctions. The FEM analysis results for prisms included in each of three test series A200H, B200H, and C200H appeared to agree with the findings obtained from previously discussed DIC system results.



(a)



(b)



(c)

Figure 4.20: Maximum Principal Stress Distribution along the Top and Bottom Web Surfaces for Prisms within Test Series: (a) A200H. (b) B200H, and (c) C200H

4.5 Practical Implications

The practical purpose of this study was to establish whether or not it would be feasible to provide Canadian masonry designers and CMU manufacturers with options to reduce web height of CMUs without significantly compromising the structural response of the resulting masonry members. This will also help to establish similarities in masonry products and research collaboration between the U.S and Canada. The results showed that CMU web height had little impact on the resulting masonry assemblage strength of grouted prisms, whereas the masonry assemblage strength of hollow prisms varied significantly with the CMU web height for all CMU sizes investigated. The practical implications discussed in the following paragraphs are based on the initial results from the small number of three-course tall concrete masonry assemblages subjected to concentric axial loading. Future testing of full-scale masonry assemblages under different loading conditions would be helpful to validate these practical implications.

CMUs with deeper knock-out webs, approaching the minimum normalized web area as included in ASTM C90-11 (ASTM, 2011), can be used in grouted masonry construction without significantly compromising the structural performance of masonry elements. This is due to the grout filling all core space including the knock-out zones as discussed in Section 4.2.2. Production and installation of CMUs with deeper knock-out webs on a large scale will help to reduce unit self-weight, and worker fatigue and injuries; therefore, would increase construction productivity. The use of CMUs with deeper knock-out webs will result in larger and continuous cell areas thereby facilitating grout placement in partially grouted and reinforced masonry construction. The provisions for minimum geometric requirements for webs of CMUs as included in ASTM C90-11 (ASTM, 2011) can possibly be adopted in Canada for grouted masonry construction practice.

Knock-out web CMUs that conform to CSA A165.1-14 (CSA, 2014a) and typically being used in Canadian construction practice can be used in hollow prisms to obtain similar masonry assemblage strength as that of prisms constructed using standard full-height web CMUs. If abundantly available at the construction site, these knock-out units can be used together with regular stretcher units to construct hollow masonry members with little impact on their structural performance. The use of CMUs with 50 mm tall webs, conforming to the provisions in ASTM C90-11 (ASTM, 2011), in hollow prisms mostly did not result in satisfactory structural performance of hollow masonry assemblages. CMUs with knock-out webs deeper than typically being used in Canadian

construction practice, with a normalized web area approaching the minimum requirements as included in ASTM C90-11 (ASTM, 2011), do not appear to be suitable for use in hollow masonry construction to obtain the design strength for masonry elements as specified in Clause 5.1 of CSA S304-14 (CSA, 2014b). The design strength used in calculating the member resistance in this clause is based on the structural response of CMUs with full-height webs and does not consider knock-out web units.

4.6 Summary

The masonry assemblage strength and failure modes of 126 prisms within 18 test series subjected to concentric axial compression were analyzed to investigate the impact of concrete masonry unit (CMU) web height on the structural performance of masonry assemblages. The use of knock-out web CMUs resulted in lower masonry assemblage strength of hollow prisms, irrespective of CMU size, as compared to those constructed using full-height web CMUs. The masonry assemblage strength of hollow prisms generally decreased with the reduction in CMU web height, but no definitive overall trend existed across different CMU sizes. An accurate mathematical relationship therefore could not be confidently established between the hollow masonry assemblage strength and CMU web height across all CMU sizes. A statistical review of the test data revealed that the CMU web height significantly influenced the masonry assemblage strength of hollow prisms, irrespective of CMU size. The masonry assemblage strength for hollow prisms constructed with either regular stretcher units or knock-out units conforming to CSA A165.1 (CSA, 2014a) were statistically similar at the 95% confidence level. In contrast, the assemblage strength of hollow prisms constructed using CMUs with 50 mm tall knock-out webs, approaching the minimum geometric requirements for webs as included in ASTM C90-11 (ASTM, 2011), was found to be significantly weaker than those constructed using regular stretcher units conforming to CSA A165.1 (CSA, 2014a). The assemblage strength of grouted prisms was, however, found to be insensitive to CMU web height. A comparison of as-tested specified masonry compressive strengths to the minimum requirements specified by CSA S304-14 (CSA, 2014b) revealed that the use of CMUs with 50 mm tall webs in hollow prisms resulted in a lower specified masonry compressive strength which did not meet the minimum value calculated using unit strength approach as prescribed by CSA S304-14 (CSA, 2014b).

Crack patterns and the resulting failure modes of prisms within different test series were investigated using the digital image correlation (DIC) system. The cracking patterns for both hollow and grouted prisms varied with CMU web height. Hollow prisms constructed with CSA A165 (CSA, 2014a) regular stretcher units generally exhibited cracks at the center of the web within the middle block course which propagated in length towards the top and bottom courses and widened as the prism approached failure. The observed cracking patterns were similar to the findings reported in previous studies (Hamid & Drysdale, 1979; Hegemier et al., 1978; Wong & Drysdale, 1985) and was analogous to a mechanism of plates subjected to in-plane tension. The corresponding grouted prisms exhibited similar cracking patterns but narrower cracks, resulting in a sudden failure. Hollow prisms constructed using knock-out web CMUs exhibited different cracking patterns than previously described, with cracks shifting from the center of the web to the web-face shell junction as the CMU web height decreased from 120 mm to 50 mm. This was due to a stress concentration at the corners of knock-out webs, caused by face shell bending, which increased with increasing knock-out height as discussed in Section 4.4. All grouted prisms constructed using knock-out web CMUs, irrespective of web height, exhibited cracking at the web-face shell junctions. Finite element modeling of the selected test series of prisms was also conducted to obtain the maximum principal stress distribution at the top and bottom surfaces of the exterior webs within each block course and so to predict the potential failure modes. Crack patterns evaluated from the analysis of the images captured using the DIC system showed good agreement with those predicted using FEM approach. The DIC system appeared to effectively capture the true cracking patterns and resulting failure modes of prisms within different test series as included in this investigation.

CHAPTER 5: CONCLUSIONS AND RECOMMENDATIONS

5.1 Overview

One hundred and twenty-six masonry prisms were constructed and tested in accordance with the relevant CSA standards to evaluate the impact of CMU web height on the resulting masonry assemblage strength and failure modes. Prisms were divided into 18 unique test series with seven replicates of each needed to identify any significant differences in masonry assemblage strength between any two prism test series at a minimum 95% confidence level. The parameters varied in the experimental investigation were: CMU web height (190 mm tall full-height, 120 mm tall knock-out, and 50 mm tall knock-out), CMU size (150, 200, and 300 mm), and the presence of grout. All prisms were constructed using 15 MPa units with CMUs of each size procured from the same batch of material. All knock-out web and half units were produced in the laboratory from standard stretcher units to ensure similar material properties. Companion specimens were cast and tested along with the prisms to establish the properties of constituent materials.

The prisms were tested under concentric axial compression with a DIC system installed to capture images of one front and side face of the prisms throughout testing. The applied load and images of each prism face were recorded at a frequency of 1 Hz until failure using a computer-controlled data acquisition system and DIC system, respectively. Load data were used to establish the resulting masonry assemblage strength of prisms within different test series in accordance with CSA S304-14. The resulting masonry assemblage strength of prisms was then used to evaluate the impact of CMU web height on prism strength. The images of prisms captured using the DIC setup were used to generate strain contour maps and stress versus strain plots. The impact of CMU web height on the failure mode of masonry prisms was then evaluated using these DIC results. The practical implications of using different types of knock-out CMUs, as included in this investigation, were then established based on the analysis of test results.

The following section presents a summary of the conclusions that are based on the testing and analysis as previously discussed.

5.2 Conclusions

The following are the conclusions of this study grouped in accordance with the specific objectives as stated in Section 1.2.

5.2.1 Influence of CMU Web Height on the Resulting Masonry Assemblage Strength

Prisms constructed using CMUs with three different web heights were tested to evaluate the influence of CMU web heights on the resulting masonry assemblage strength. Both grouted and hollow prisms were included in this investigation.

- The average masonry assemblage strength of hollow prisms decreased with decreasing web height of CMUs, irrespective of the size of CMUs used in prism construction. The reduction in the web height of CMUs appeared to reduce the ability of face shells to resist the externally applied load, which ultimately affected the resistance of hollow masonry assemblages.
- The average masonry assemblage strength of grouted prisms was generally similar for prisms constructed with CMUs of different web heights for all CMU sizes. The continuity provided by the grout, which filled all core space including the knock-out zones, fulfilled the structural role of the webs in prisms constructed using knock-out web CMUs. This resulted in prisms constructed with knock-out web CMUs to have similar strength as those constructed with full-height web CMUs.

5.2.2 Determining Statistical Difference in Masonry Assemblage Strength Between Prisms Constructed Using CMUs with Web Height Conforming to CSA A165.1 and ASTM C90

One-way ANOVA test and Post-Hoc analyses were used to identify any statistically significant differences in masonry assemblage strength between prisms constructed using CMUs of different web heights at a 95% confidence level.

- The use of knock-out units conforming to CSA A165.1-14 in constructing hollow prisms resulted in a statistically similar masonry assemblage strength as that of hollow prisms constructed with full-height web units regardless of CMU size. In contrast, the use of knock-out units conforming to minimum allowable web areas prescribed in ASTM C90-11 resulted in significantly lower masonry assemblage strength for hollow prisms as

compared to those constructed with full-height web units, irrespective of the CMU size. Further, the resulting masonry assemblage strength of hollow prisms constructed with knock-out units conforming to minimum web areas in ASTM C90-11 generally did not meet the minimum strength requirement specified by CSA S304-14.

- The use of knock-out units conforming to either CSA A165.1-14 or ASTM C90-11 in constructing grouted prisms resulted in statistically similar masonry assemblage strength to that of grouted prisms constructed with CMUs that included full-height webs regardless of CMU size. The use of either type of knock-out CMUs in grouted prism construction therefore had little impact on the resulting masonry assemblage strength.

5.2.3 Influence of CMU Web Height on the Failure Mode of Masonry Prisms

Data obtained from the analysis of images captured using the DIC system were used to generate principal strain contour maps and axial stress versus principal strain plots on one of the exterior web face and face shell of prisms. The evaluation of these plots revealed that the tensile splitting of the webs typically caused the failure in both hollow and grouted prisms regardless of CMU web height and size. Cracking patterns were evaluated using the principal strain contour maps; however, these varied with the web height of CMUs for both hollow and grouted prisms.

- Hollow prisms constructed using CMUs with full-height, 120, and 50 mm tall webs exhibited vertical cracks at the center of the exterior web face, diagonal cracks in a region between the center and the web-face shell junction, and vertical cracks at the junction of web and face shell, respectively. The shifting of vertical cracks from the center of the web to the web-face shell junction in hollow prisms, as observed in one of the exterior web face, was due to the stress concentration at the corners of knockout webs resulting from the bending of the face shells, which increased with increasing knockout height.
- Grouted prisms constructed using CMUs with full-height webs exhibited similar cracking as in corresponding hollow prisms, whereas the use of either type of knock-out web unit resulted in cracks along the web-face shell junction. The cracks in grouted prisms were, however, narrower than in hollow prisms and resulted in a sudden failure. This was due to the improved stability of grouted prisms as the applied load was shared between the CMU and grout.

- The evaluation of axial stress versus strain plots showed a sudden increase in maximum principal strain on the exterior web face for all hollow and grouted prisms as they approached failure, irrespective of the web height and size of CMUs. This shows that both hollow and grouted prisms experienced tensile splitting of the webs at failure. Good agreement was shown between the principal strain contour maps and axial stress versus principal strain plots. This suggested that the DIC technique could be effectively used in obtaining stress versus strain plots on the masonry prisms to capture their actual mechanical behavior during loading.

5.2.4 Comparison of Failure Modes Predicted Using the Finite Element Modeling Approach to Those Evaluated Using the Results Obtained from the DIC System

Stress distribution plots at the top and bottom of the exterior webs within each block course of prisms from the selected test series were generated using a finite element modeling approach. The concentration of maximum principal stresses found in these plots allowed for a prediction of the location of potential cracking. Crack patterns predicted using the FEM approach and those evaluated using the results obtained from the DIC system were compared to determine whether any considerable differences existed.

- Hollow prisms constructed using 200 mm full-height web CMUs were hypothesized to experience vertical cracks in the middle of the exterior webs based on the FEM analysis. The evaluation of the principal strain contour maps of these prisms generated from the DIC results revealed vertical cracks at the middle of the exterior webs which propagated along the prism height as failure approached. Cracking patterns predicted using the results from FEM analysis matched with those evaluated using the results from the DIC system.
- Based on FEM analysis results, cracks were predicted to occur in a region between the center of the web and web-face shell junction for hollow prisms constructed using 200 mm CMUs with 120 mm tall knock-out webs. The evaluation of the principal strain contour maps of these prisms generated from the analysis of the DIC images revealed diagonal cracks occurring in a region between the center of the web and web-face shell junction of the exterior webs. Cracking patterns predicted using analytical means were similar to those evaluated using the results obtained from the DIC system.

- FEM analysis results revealed that the cracks were predicted to occur at the web-face shell junctions of the exterior web in hollow prisms constructed using 200 mm CMUs with 50 mm tall knock-out webs. The evaluation of the principal strain contour maps of these prisms generated from the analysis of the DIC images revealed the occurrence of vertical cracks at the web-face shell junctions of the exterior webs. Cracking patterns predicted using the results from FEM analysis were in good agreement to those evaluated experimentally using the DIC system.

5.3 Recommendations for Future Research

The scope of this study was limited based on practical and financial considerations. Meaningful information was obtained from this study but further investigations, as recommended in the following paragraphs, would supplement the findings from this study.

1. This study evaluated the impact of web height of CMUs on the resulting masonry assemblage strength and failure mode of prisms based on three different web heights: full-height which represented regular stretcher units, 120 mm tall webs which represented typical knock-out units used in Canada, and 50 mm tall webs that approached the minimum normalized web area of $45,140 \text{ mm}^2/\text{m}^2$ as included in ASTM C90-11. The normalized web area of CMUs can be varied in several possible ways: either by changing the web height, web thickness, the number of webs, or any combination of these three options. Experimental investigations involving prism testing that include CMUs with different web thicknesses and/or number of webs are therefore recommended. The results from the current and recommended studies then can be collectively used to evaluate the overall impact of the normalized web area of CMUs on the structural performance of masonry prisms. The provisions for minimum geometric requirements of the webs in CMUs as included in ASTM C90-11 can then be confidently adopted in Canada with or without any changes based on the overall assessment of results from both studies.
2. All masonry prisms included in this investigation were one block-wide, three-courses tall, and tested under concentric axial loading. A parametric investigation involving taller prisms or wallettes subjected to different load types would be helpful to assess the validity of the results from this study in terms of its application in general masonry construction.

REFERENCES

- ANSYS, Inc. (1970). “ANSYS Workbench.” Accessed on July 21, 2021, <<https://www.ansys.com/products/ansys-workbench>>.
- Anton, D., Rosecrance, J.C., Gerr, F., Merlino, L.A., and Cook, T.M. (2005). “Effect of Concrete Block Weight and Wall Height on Electromyographic Activity and Heart Rate of Masons.” *Ergonomics*, Vol. 48, Issue 10, pp. 1314–1330.
- ASTM International. (2021). “ASTM E178-21: Standard Practice for Dealing with Outlying Observations.” ASTM Standards, West Conshohocken, PA, USA.
- ASTM International. (2020). “ASTM C140-20: Standard Test Method for Sampling and Testing Concrete Masonry Units and Related Units.” ASTM Standards, West Conshohocken, PA, USA.
- ASTM International. (2018). “ASTM C1019-18: Standard Test Method for Sampling and Testing Grout.” ASTM Standards, West Conshohocken, PA, USA.
- ASTM International. (2011). “ASTM C90-11 (R2016): Standard Specification for Loadbearing Concrete Masonry Units.” ASTM Standards, West Conshohocken, PA, USA.
- Boult B.F. (1979). “Concrete Masonry Prism Testing.” *ACI Journal*, Vol. 76, Issue 4, pp. 513-536.
- Canadian Standards Association. (2014a). “CSA A165.1-14: Concrete Masonry Units.” CSA, Rexdale, Ontario, Canada.
- Canadian Standards Association. (2014b). “CSA S304-14 (R2019): Design of Masonry Structures.” CSA, Rexdale, Ontario, Canada.
- Canadian Standards Association. (2014c). “CSA-A179-14: Mortar and Grout for Unit Masonry.” CSA, Rexdale, Ontario, Canada.
- Canadian Standards Association. (2008). “CAN/CSA A3004-C2: Test Method for Determination of Compressive Strengths.” CSA, Rexdale, Ontario, Canada.
- Chahine, G.N. (1989). “Behaviour Characteristics of Face Shell Mortared Block Masonry under Axial Compression.” M.Eng. Thesis, McMaster University, Hamilton, ON, Canada.

Cintron, R., Saouma, V. (2008). "Strain Measurements with Digital Image Correlation System Vic-2D (CU-NEES-08-06)." The George E. Brown, Jr. Network for Earthquake Engineering Simulation.

Correlated Solutions, Inc. (1998). "Vic 3D." Accessed on October 03, 2020, <<https://www.correlatedsolutions.com/vic-3d/>>.

Drysdale, R.G., Hamid, A.A. (2005). "Masonry Structures: Behavior and Design." Canada Masonry Design Centre, Mississauga, ON, Canada.

Drysdale, R.G., Hamid, A.A. (1979). "Behavior of Concrete Block Masonry Under Axial Compression." *ACI Journal*, Vol. 76, Issue 6, pp. 707-722.

Duncan, L. J. (2008). "Effect of Block Face Shell Geometry and Grouting on the Compressive Strength of Concrete Block Masonry." M.Sc. Thesis, University of Windsor, Windsor, ON, Canada.

Faber, G.S., Kingma, I., Kuijer, P.P.F.M., van der Molen, H.F., Hoozemans, M.J.M., Frings-Dresen, M.H.W., and van Dieën, J.H. (2009). "Working Height, Block Mass, and One- vs. Two-Handed Block Handling: The Contribution to Low Back and Shoulder Loading During Masonry Work." *Ergonomics*, Vol. 52, Issue 9, pp. 1104–1118.

Fahmy, E. H., & Ghoneim, T. G. M. (1995). "Behaviour of Concrete Block Masonry Prisms under Axial Compression." *Canadian Journal of Civil Engineering*, Vol. 22, No. 5, pp. 898–915.

Ganesan, T. P., & Ramamurthy, K. (1992). "Behavior of Concrete Hollow-Block Masonry Prisms under Axial Compression." *Journal of Structural Engineering*, Vol. 118, No. 7, pp. 1751–1769.

Gayed, M., Korany, Y. (2011). "Concrete Masonry Compressive Strength Using the Unit Strength Method." Masonry Chair Report No. 102-2011, University of Alberta, Edmonton, AB, Canada.

Hamid, A. A., Abboud, B. E., & Harris, H. G. (1985). "Direct Modeling of Concrete Block Masonry Under Axial Compression." *Masonry: Research, Application, and Problems*, ASTM STP 871, pp. 151-166.

Hamid, A. A., & Chukwunenye, A. O. (1986). "Compression Behavior of Concrete Masonry Prisms." *Journal of Structural Engineering*, Vol. 112, No. 3, pp. 605–613.

- Hamid, A. A., & Drysdale, R. G. (1979). "Suggested Failure Criteria for Grouted Concrete Masonry Under Axial Compression." *ACI Journal*, Vol. 76, Issue 10, pp. 1047-1062.
- Hegemier, Krishnamoorthy, G., Nunn, R., & Moortly, T. (1978). "Prism Tests for the Compression Strength of Concrete Masonry." *Proceedings of the North American Masonry Conference*, Boulder, Colorado.
- Hoozemans, M.J.M., Kingma, I., Vries, W.H.K. de, and Van, J.H. (2008). "Effect of Lifting Height and Load Mass on Low Back Loading." *Ergonomics*, Vol. 51, Issue 7, pp. 1053–1063.
- Kaaki, T. (2013). "Behavior and Strength of Masonry Prisms Loaded in Compression." M.A.Sc. Thesis, Dalhousie University, Halifax, Nova Scotia, Canada.
- Köksal, H. O., Karakoç, C., & Yildirim, H. (2005). "Compression Behavior and Failure Mechanisms of Concrete Masonry Prisms." *Journal of Materials in Civil Engineering*, Vol. 17, No. 1, pp. 107–115.
- Khalaf, F.M. (1996). "Factors Influencing Compressive Strength of Concrete Masonry Prisms." *Magazine of Concrete Research*, Vol. 48, No. 175, pp. 95-101.
- Lang, N. R., & Thompson, J. J. (2014). "Recent Changes to ASTM Specification C90 and Impact on Concrete Masonry Unit Technology." *Masonry*, ASTM STP 1577, pp. 123–137.
- Maurenbrecher, A. H. P. (1986). "Compressive Strength of Hollow Concrete Masonry." *Proceedings of the 4th Canadian Masonry Symposium*, Fredericton, New Brunswick, Vol. 2, No. 1405, pp. 997-1009.
- Maurenbrecher, A.H.P. (1980). "Effect of Test Procedures on Compressive Strength of Masonry Prisms." *Second Canadian Masonry Symposium*, Vol. 2, No. 922, pp. 119–132.
- Mohamad, G., Fonseca, F. S., Vermeltfoort, A. T., Martens, D. R. W., & Lourenço, P. B. (2017). "Strength Behavior and Failure Mode of Hollow Concrete Masonry Constructed with Mortars of Different Strengths." *Construction and Building Materials*, Vol. 134, pp. 489–496.
- National Concrete Masonry Association. (2012). "ASTM Specifications for Concrete Masonry Units." TEK 01-01F, NCMA, Herndon, VA.

Ramamurthy, K. (1995). "Behaviour of Grouted Concrete Hollow Block Masonry Prisms." Magazine of Concrete Research, Vol. 47, No. 173, pp. 345–354.

Reu, P. (2014). "All About Speckles: Speckle Size Measurement." Experimental Techniques, Vol. 38, Issue 6, pp. 1-2.

Ross, M., Korany, Y. (2012). "Concrete Masonry Compressive Strength Using the Unit Strength Method for Grouted Masonry." Masonry Chair Report No. 105-2012, University of Alberta, Edmonton, AB, Canada.

Santos, C. F. R., Alvarenga, R. C. S. S., Ribeiro, J. C. L., Castro, L. O., Silva, R. M., Santos, A. A. R., & Nalon, G. H. (2017). "Numerical and Experimental Evaluation of Masonry Prisms by Finite Element Method." IBRACON Structures and Materials Journal, Vol. 10, No. 2, pp. 477-508.

Wong, H., & Drysdale, R. (1985). "Compression Characteristics of Concrete Block Masonry Prisms." Masonry: Research, Application, and Problems, ASTM STP 871, pp. 167–177.

APPENDICES

APPENDIX 3A: DETERMINATION OF THE NUMBER OF REPLICATE MASONRY PRISMS

This appendix presents the calculation of the required number of replicate prisms to identify a statistically significant difference in the compression test results between two sample populations at a minimum of 95% confidence level. Table 3A-1 presents the average masonry assemblage strength, \bar{f}_m , and associated coefficient of variation (*COV*) for hollow and grouted prisms that were obtained from a test dataset reported in the available literature (Gayed & Korany, 2011; Ross Korany, 2012), as discussed in Section 2.5. These data were used to calculate the required number of replicates. All data were collected for three-block tall, and one-block long prisms constructed using standard 200 mm CMUs so that the only parameter that varied between two sample populations was the presence of grout. The standard deviation for each sample population was calculated manually using the reported \bar{f}_m and *COV* values.

Table 3A-1: Reported Data for Determining the Required Number of Replicates

	Three-Course Tall Hollow Prisms	Three-Course Tall Grouted Prisms
Number of Reported Prisms	402	327
Mean Assemblage Strength (MPa)	15.3	14.2
Coefficient of Variation (%)	6.02	6.88
Standard Deviation (MPa)	0.924	0.973

An equal variance independent t-test was used as a statistical tool to determine the required number of replicate specimens. Equations 3A-1 and 3A-2 were used to calculate the *t-value* and degrees of freedom, respectively, required to establish this number.

$$t - \text{Value} = \frac{f'_{mH} - f'_{mG}}{\sqrt{\frac{(n_H - 1) \cdot s_H^2 + (n_G - 1) \cdot s_G^2}{n_H + n_G - 2}} \cdot \sqrt{\left(\frac{1}{n_H} + \frac{1}{n_G}\right)}} \quad \text{Equation 3A-1}$$

And,

$$\text{Degrees of Freedom (DOF)} = n_H + n_G - 2 \quad \text{Equation 3A-2}$$

Where:

f'_{mH} and f'_{mG} = Mean masonry assemblage strength for hollow and grouted prisms, respectively.

s_H and s_G = Standard deviation for the masonry assemblage strength of hollow and grouted prisms, respectively.

n_H and n_G = Number of hollow and grouted masonry prism replicates, respectively.

Table 3A-2 shows the *t-value* calculated for a different number of replicate specimens using Equation 3A-1 and the corresponding confidence level obtained from the standard t-table. A 96% confidence level was obtained from a two-tailed student “t” table for a *t-value* of 2.35 with 12 degrees of freedom. Seven replicate specimens were therefore determined to be sufficient to identify a statistically significant difference between two sample populations at a minimum of 95% confidence level with a power of approximately 58%.

Table 3A-2: t-Value and Confidence Level Based on the Number of Replicate Specimens

n_H or n_G	<i>DOF</i>	<i>t-Value</i>	Confidence Level %
5	8	1.98	91.4
6	10	2.17	94.3
7	12	2.35	96.0
8	14	2.51	97.3
9	16	2.66	98.2

APPENDIX 4A: COMPANION SPECIMEN TEST RESULTS

This appendix includes the as-measured minimum CMU dimensions, the resulting net effective areas of both hollow and grouted prisms, and the individual test results of CMUs, mortar cubes, non-absorbent grout cylinders, and absorptive grout prisms.

Table 4A-1 shows the as-measured minimum web, t_{min_w} , and face shell, $t_{min_{fs}}$, thicknesses for all CMU sizes used in the experimental investigation. A digital caliper was used to measure these dimensions for 5 sample units with specimen numbers, n , ranging from #1 to 5 from each CMU size. The measurements of each CMU were based on the average of 3 readings (1 to 3).

Table 4A-2 shows as-calculated effective areas needed to establish the resulting compressive strength of CMUs and masonry assemblages. The determination of the effective mortared area for face shell bedded prisms has been a source of confusion for both designers and researchers. Some researchers have used the net unit area to calculate the masonry assemblage strength while others have used an area based on the minimum thickness of the unit's face shells (Chahine, 1989). The actual mortar bedded area for standard 200 mm hollow masonry constructed in running bond with face shell mortar bedding is around 20% greater than the area based on the minimum face shell thickness (Maurenbrecher, 1986). However, there is no consensus as this value tends to vary with CMU size. An effective mortared area based on the as-measured minimum face shell thickness was therefore used to maintain consistency in assemblage strengths for all hollow prisms. Similarly, the net and gross area of the respective CMU were used to calculate its compressive strength and the masonry assemblage strength for grouted prisms, respectively.

Tables 4A-3 and 4A-4 present the compression and absorption test results, respectively, for CMUs used in prism construction. The results are reported for each CMU size. Table 4A-5 shows the compressive strength of the mortar cubes resulting from all mortar batches used in prism construction. Each mortar cube was provided with a unique identification mark of the form $x-y$, x corresponding to the batch number, while y represents the specimen number. Tables 4A-6 and 4A-7 present the compressive strength of the non-absorbent grout cylinders and absorptive grout prisms, respectively, tested in conjunction with the prisms. The identification marks for non-absorbent grout cylinders and absorptive grout prisms are similar to that of the mortar cubes.

Table 4A-1: As-Measured Minimum CMU Dimensions

Nominal CMU Size (mm)	<i>n</i>	Minimum Web Thickness, t_{min_w} (mm)				Minimum Face Shell Thickness, $t_{min_{fs}}$ (mm)					
		Readings (R)			\bar{R}	Mean t_{min_w}	Readings (R)			\bar{R}	Mean $t_{min_{fs}}$
		1	2	3			1	2	3		
150	#1	27.2	27.1	27.9	27.4		27.9	27.6	27.6	27.7	
	#2	27.9	28.3	28.2	28.1		27.3	27.3	27.4	27.4	
	#3	27.2	28.4	28.2	27.9	27.8	27.5	27.6	27.4	27.5	27.4
	#4	27.1	28.3	28.3	27.9		26.8	27.1	27.8	27.2	
	#5	27.8	27.7	27.6	27.7		27.4	27.3	27.5	27.4	
200	#1	28.3	28.1	27.3	27.9		33.8	33.9	33.8	33.9	
	#2	27.7	28.3	27.7	27.9		33.9	33.7	33.6	33.7	
	#3	27.8	28.2	27.6	27.9	28.0	34.0	33.6	33.9	33.8	33.8
	#4	28.6	28.5	27.2	28.1		34.0	33.5	34.0	33.8	
	#5	28.0	28.5	28.0	28.1		33.5	33.9	33.8	33.7	
300	#1	33.7	33.1	33.9	33.5		40.5	41.1	39.9	40.5	
	#2	33.7	32.6	32.7	33.0		40.3	39.4	39.3	39.7	
	#3	33.0	33.0	33.8	33.2	33.1	38.8	39.1	40.3	39.4	40.1
	#4	32.2	32.6	33.6	32.8		41.4	40.7	39.0	40.4	
	#5	33.3	32.7	32.9	32.9		40.9	42.0	38.7	40.5	

Table 4A-2: As-Calculated Effective Areas

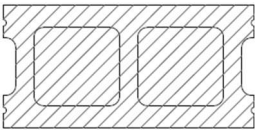
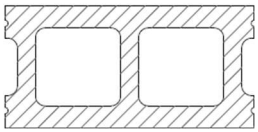
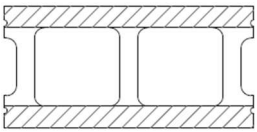
Nominal CMU Size (mm)	Gross Unit Area (mm ²)	Net Unit Area (mm ²)	Face Shell Bedded Area (mm ²)
			
150	53100	31100	21800
200	70600	38500	26500
300	106000	53200	31200

Table 4A-3: CMU Compression Test Results

Nominal CMU Size (mm)	Compressive Strength (MPa)						Mean (MPa)
	#1	#2	#3	#4	#5	#6	
150	25.1	30.2	26.2	32.2	32.5	28.9	29.2
200	32.7	34.0	26.8	32.7	30.1	31.2	31.2
300	23.9	22.4	20.5	20.9	21.4	19.9	21.5

Table 4A-4: CMU Absorption Test Results

Nominal CMU Size (mm)	<i>n</i>	Received Weight (kg)	Saturated Weight (kg)	Immersed Weight (kg)	Oven-Dry Weight (kg)	Moisture Content (%)	Absorption (%)	Density (kg/m ³)
150	#1	13.3	13.6	7.80	13.2	1.09	3.27	2270
	#2	13.3	13.6	7.80	13.1	1.36	3.63	2260
	#3	13.3	13.6	7.80	13.2	0.890	2.92	2280
	#4	13.2	13.5	7.71	13.0	1.37	3.30	2260
	#5	13.1	13.4	7.64	13.0	0.930	3.81	2230
	#6	13.3	13.6	7.76	13.2	1.18	3.28	2260
Mean		13.3	13.6	7.75	13.1	1.14	3.37	2260
200	#1	17.7	18.1	10.7	17.5	0.780	3.49	2340
	#2	16.7	17.3	9.96	16.5	0.960	4.95	2240
	#3	17.2	17.7	10.3	17.0	1.20	4.41	2280
	#4	16.7	17.2	9.89	16.5	1.23	3.98	2260
	#5	16.5	17.2	9.82	16.3	1.25	5.42	2210
	#6	16.7	17.3	9.98	16.5	1.10	4.52	2260
Mean		16.9	17.5	10.1	16.7	1.09	4.46	2270
300	#1	23.8	24.5	14.1	23.5	1.20	4.15	2260
	#2	24.6	25.3	14.6	24.3	1.24	4.01	2280
	#3	24.4	25.1	14.4	24.1	1.26	4.24	2240
	#4	23.8	24.6	14.0	23.4	1.60	4.94	2220
	#5	23.8	24.5	14.0	23.4	1.77	4.84	2220
	#6	24.7	25.4	14.7	25.3	1.47	4.29	2270
Mean		24.2	24.9	14.3	24.0	1.42	4.41	2250

Table 4A-5: Mortar Cube Compression Test Results

Batch No.	Prism Test Series	<i>n</i>	Age @ Test (Days)	Compressive Strength (MPa)	Batch No.	Prism Test Series	<i>n</i>	Age @ Test (Days)	Compressive Strength (MPa)
1	A200H & A200G	1-1	28	15.6	4	C150G	4-1	31	10.5
		1-2	29	19.0			4-2	31	13.5
		1-3	29	18.9			4-3	31	10.2
		1-4	30	12.4			4-4	33	13.9
		1-5	30	13.8			4-5	33	14.4
		1-6	31	14.3			4-6	33	15.5
		1-7	31	14.4			4-7	33	16.0
		1-8	32	18.7			4-8	33	15.6
		1-9	32	19.7			4-9	33	14.7
Mean				16.3	Mean				13.8
2	C200H & C200G	2-1	28	9.72	5	A150H & A150G	5-1	28	22.2
		2-2	28	9.93			5-2	28	20.1
		2-3	29	9.93			5-3	29	20.0
		2-4	30	7.77			5-4	29	19.6
		2-5	30	7.78			5-5	29	21.2
		2-6	31	7.61			5-6	30	15.1
		2-7	31	9.22			5-7	30	16.7
		2-8	32	9.70			5-8	31	16.9
		2-9	32	9.18			5-9	31	16.4
Mean				8.98	Mean				18.7
3	B200H & B200G	3-1	28	9.35	6	B150H & B150G	6-1	28	27.0
		3-2	28	10.0			6-2	28	24.1
		3-3	31	9.47			6-3	28	25.4
		3-4	31	11.4			6-4	29	25.7
		3-5	32	15.5			6-5	29	22.8
		3-6	32	14.9			6-6	30	19.3
		3-7	33	16.0			6-7	30	19.1
		3-8	33	15.5			6-8	31	21.2
		3-9	34	15.8			6-9	31	19.7
Mean				13.1	Mean				22.7

Table 4A-5 Cont'd: Mortar Cube Compression Test Results

Batch No.	Prism Test Series	<i>n</i>	Age @ Test (Days)	Compressive Strength (MPa)	Batch No.	Prism Test Series	<i>n</i>	Age @ Test (Days)	Compressive Strength (MPa)
7	A300H	7-1	29	14.0	9	B300H	9-1	28	12.0
		7-2	29	14.4			9-2	28	12.0
		7-3	29	14.9			9-3	28	10.1
		7-4	32	16.3			9-4	28	10.4
		7-5	32	16.8			9-5	28	14.9
		7-6	32	16.4			9-6	29	13.4
		7-7	32	16.4			9-7	29	14.8
		7-8	32	17.0			9-8	29	13.5
		7-9	32	16.7			9-9	29	13.4
Mean				15.9	Mean				12.7
8	C300H	8-1	29	13.6	10	C150H	10-1	28	16.5
		8-2	29	17.0			10-2	28	16.8
		8-3	32	17.0			10-3	28	17.1
		8-4	32	19.5			10-4	28	16.9
		8-5	32	19.3			10-5	29	16.2
		8-6	32	19.9			10-6	29	15.6
		8-7	32	21.7			10-7	29	18.1
		8-8	32	21.9			10-8	29	17.7
		8-9	32	20.7			10-9	29	15.6
Mean				19.0	Mean				16.7

Table 4A-6: Non-Absorbent Grout Cylinder Test Results

Batch No.	Prism Test Series	<i>n</i>	Age @ Test (Days)	Compressive Strength (MPa)	Batch No.	Prism Test Series	<i>n</i>	Age @ Test (Days)	Compressive Strength (MPa)
1	A200G	1-1	28	20.7	4	C150G	4-1	28	15.1
		1-2	30	20.6			4-2	30	16.6
		1-3	31	21.0			4-3	30	16.9
Mean				20.8	Mean				16.2
2	C200G	2-1	28	13.9	5	A150G	5-1	28	15.8
		2-2	30	12.9			5-2	30	15.8
		2-3	31	14.4			5-3	30	16.8
Mean				13.7	Mean				16.1
3	B200G	3-1	28	16.4	6	B150G	6-1	28	16.6
		3-2	30	15.2			6-2	30	15.6
		3-3	31	16.3			6-3	30	16.6
Mean				16.0	Mean				16.3

Table 4A-7: Absorptive Grout Prism Test Results

Batch No.	Prism Test Series	<i>n</i>	Age @ Test (Days)	Compressive Strength (MPa)	Batch No.	Prism Test Series	<i>n</i>	Age @ Test (Days)	Compressive Strength (MPa)
1	A200G	1-1	28	21.6	4	C150G	4-1	28	15.9
		1-2	30	22.3			4-2	30	14.6
		1-3	31	24.5			4-3	30	18.3
Mean				22.8	Mean				16.3
2	C200G	2-1	28	15.8	5	A150G	5-1	28	12.5
		2-2	30	14.0			5-2	30	14.7
		2-3	31	13.4			5-3	30	13.7
Mean				14.4	Mean				13.6
3	B200G	3-1	28	17.7	6	B150G	6-1	28	13.6
		3-2	30	13.6			6-2	30	15.2
		3-3	31	18.2			6-3	30	13.3
Mean				16.5	Mean				14.0

APPENDIX 4B: MASONRY PRISM COMPRESSION TEST RESULTS

Table 4B-1 reports the as-tested masonry assemblage strengths for all individual hollow and grouted prisms. The mean assemblage strength, \bar{f}_m , and respective *COV*s for prisms within each test series are also presented. The maximum load recorded for each prism during testing was divided by its effective mortared area to obtain the masonry assemblage strength. This effective mortared area for hollow (face shell bedded area) and grouted (gross unit area) prism test series are reported in Table 4A-2. Similarly, Tables 4B-2 and 4B-3 show the results obtained from one-way ANOVA and post-hoc tests, respectively. The confidence level for these tests was selected as 95%, which is considered accurate for engineering purposes. Any *p*-values less than 0.05 are therefore statistically significant.

Figure 4B-1 shows the regression analysis plots with web heights on the x-axis and masonry assemblage strength on the y-axis associated with hollow prisms constructed using three CMU sizes. A best fitting polynomial trend line of order 2 was plotted for each CMU size to establish the mathematical relationship between the CMU web height and resulting masonry assemblage strength. The R^2 values and polynomial equations for each trend line are also presented.

Table 4B-4 presents the detailed calculation related to the as-tested and minimum specified masonry compressive strength obtained using the experimental results and recommendations provided by CSA S304-14 (CSA, 2014b), respectively. Masonry prisms constructed using 150, 200, and 300 mm CMUs resulted in *h/t* ratio of 4.21, 3.11, and 2.04, respectively. The corresponding *h/t* correction factors were calculated using the table presented in Section 2.4.4 and were found to be 0.96, 0.91, and 0.8, respectively. The as-tested masonry assemblage strengths presented in Table 4B-1, as included in Appendix 4B, were multiplied by the corresponding *h/t* correction factors to obtain the masonry assemblage strength as would be expected from the full-scale wall. This ensured that the specified masonry compressive strength obtained from the experimental results, f'_{m_expt} , could be readily compared to the minimum value specified by CSA S304-14 (CSA, 2014b), f'_{m_CSA} . The *h/t* normalized mean assemblage strength and *COV* for prisms within each test series were then used to calculate the corresponding f'_{m_expt} following the procedures specified in Clause C.2.2 in CSA S304-14 (CSA, 2014b). The f'_{m_expt} for each prism test series were compared to the f'_{m_CSA} , which was calculated using the unit strength approach as

specified in Table 4 in CSA S304-14 (CSA, 2014b), and the related discussion was presented in Section 4.2.3.

Table 4B-1: As-Tested Masonry Assemblage Strength for Prisms

Test Series	Assemblage Strength (MPa)							\bar{f}_m (MPa)	COV (%)
	#1	#2	#3	#4	#5	#6	#7		
A150H	20.5	22.2	25.0	23.0	26.4	25.9	23.2	23.7	9.06
B150H	11.5	15.4	18.9	19.2	23.3	15.9	25.4	18.5	25.8
C150H	18.5	17.8	12.3	25.0	11.3	14.4	23.7	17.6	30.5
A200H	22.8	28.3	21.0	28.8	22.0	27.9	25.2	25.2	13.0
B200H	24.8	28.1	21.8	20.7	26.8	22.7	21.2	23.7	12.2
C200H	15.5	16.4	11.3	14.2	11.1	12.5	15.5	13.8	15.6
A300H	28.8	30.7	26.4	27.7	24.3	28.6	27.4	27.7	7.27
B300H	29.8	30.2	28.8	27.2	27.9	27.7	28.6	28.6	3.82
C300H	23.7	28.2	22.7	23.7	24.8	25.5	22.9	24.5	7.78
A150G	15.3	19.5	17.1	15.9	18.4	18.5	18.6	17.6	8.70
B150G	19.3	20.8	20.4	19.0	18.2	21.0	20.6	19.9	5.32
C150G	18.3	15.1	14.2	18.7	16.1	16.5	16.9	16.5	9.77
A200G	16.1	15.9	15.0	17.1	14.9	19.2	22.0	17.2	15.1
B200G	16.0	17.8	13.8	16.6	14.8	14.1	17.3	15.8	10.0
C200G	16.7	15.2	16.9	17.2	15.0	17.1	17.2	16.5	5.70

Table 4B-2: One-Way ANOVA Results

Test Series	Source of Variation	Sum of Squares	Degree of freedom	Mean Square	<i>F</i> -Value	<i>P</i> -Value
A150H	Between Groups ¹	155	2	77.6	4.14	0.033*
B150H						
C150H	Within Groups ²	337	18	18.7		
A200H	Between Groups ¹	537	2	269	34.1	< 0.001*
B200H						
C200H	Within Groups ²	142	18	7.88		
A300H	Between Groups ¹	65.0	2	32.5	11.0	< 0.001*
B300H						
C300H	Within Groups ²	53.3	18	2.96		
A150G	Between Groups ¹	40.9	2	20.4	10.1	0.001*
B150G						
C150G	Within Groups ²	36.5	18	2.03		
A200G	Between Groups ¹	6.83	2	3.42	1.02	0.38
B200G						
C200G	Within Groups ²	60.5	18	3.36		

¹ Source of variation between two test series.

² Source of variation within each test series.

* Represents significant *P*-values (i.e., less than 0.05).

Table 4B-3: Post-Hoc Analysis Results

Description	Test Series	<i>P</i> -Value	
Hollow Prisms Constructed With 150 mm CMUs	A150H	B150H	0.088
		C150H	0.039*
	B150H	A150H	0.088
		C150H	0.911
Hollow Prisms Constructed With 200 mm CMUs	A200H	B150H	0.612
		C150H	< 0.001*
	B200H	A150H	0.612
		C150H	< 0.001*
Hollow Prisms Constructed With 300 mm CMUs	A300H	B150H	0.610
		C150H	0.007*
	B300H	A150H	0.610
		C150H	0.001*
Grouted Prisms Constructed With 150 mm CMUs	A150G	B150G	0.020*
		C150G	0.360
	B150G	A150G	0.020*
		C150G	0.001*
	C150G	A150G	0.360
		B150G	0.001*

* Represents significant *P*-values (i.e., less than 0.05).

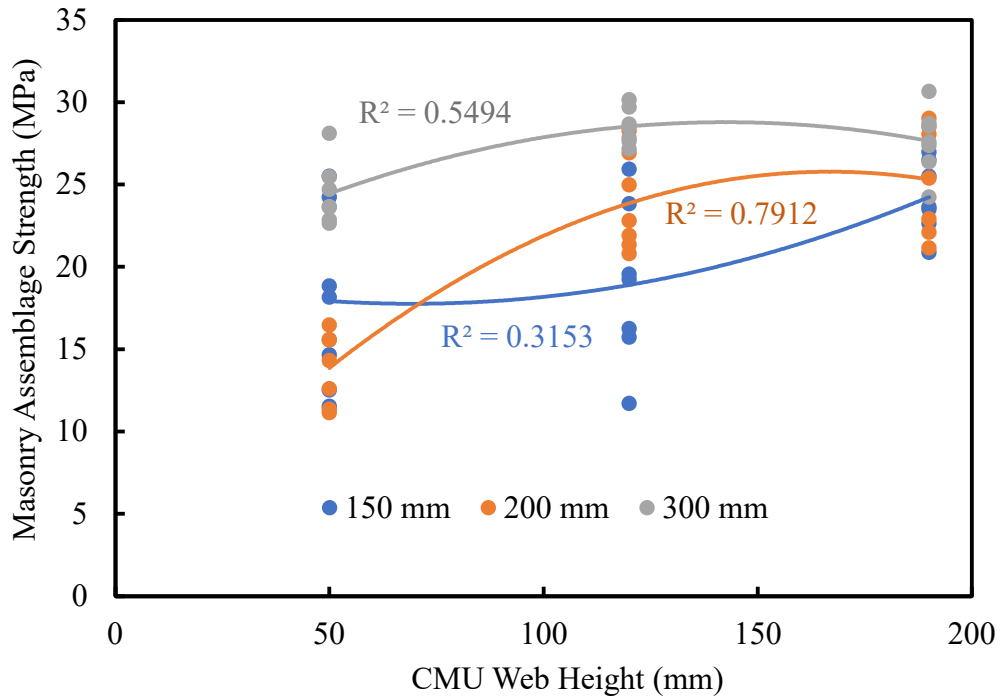


Figure 4B-1: Regression Analysis Plots for Hollow Masonry Prisms

Polynomial functions:

For CMUs of size,

150 mm: $y = 0.0004x^2 - 0.062x + 19.9$

Equation 4B-1

200 mm: $y = -0.0009x^2 + 0.291x + 1.48$

Equation 4B-2

300 mm: $y = -0.0005x^2 + 0.145x + 18.5$

Equation 4B-3

Table 4B-4: Calculation Results for Experimental and Minimum Specified Masonry Compressive Strength

Test Series	$\frac{h}{t}$ Normalized \bar{f}_m (MPa)	SD (MPa)	f'_{m_expt} (MPa)	f'_{block} (MPa)	Mortar Type (S/N)	Grouted/ Hollow	f'_{m_CSA} (MPa)	$f'_{m_expt} \geq f'_{m_CSA}?$
A150H	22.8	2.15	19.3					Yes
B150H	9.92	4.78	9.92			Hollow	14.5	No
C150H	8.07	5.35	8.07					No
A150G	17.6	1.53	15.1	23.4				
B150G	19.9	1.06	18.2			Grouted	11.2	Yes
C150G	16.5	1.62	13.9					
A200H	22.9	3.27	17.5					Yes
B200H	21.6	2.89	16.8		S	Hollow	15.9	Yes
C200H	12.5	2.15	9.01					No
A200G	17.2	2.59	12.9	26.4				
B200G	15.8	1.58	13.2			Grouted	12.2	Yes
C200G	16.5	0.940	14.9					
A300H	23.6	2.02	20.3					
B300H	24.3	1.09	22.5	18.0		Hollow	11.8	Yes
C300H	20.8	1.91	17.7					
A300G	N/A							
B300G								
C300G								

APPENDIX 4C: DIC SYSTEM RESULTS

Strain Contour Maps

Figures 4C-1 to 4C-15 show maximum principal strain, ε_{max} , contour maps on the exterior web face of prisms as obtained from the analysis of DIC images. Representative crack patterns for prism within each test series was discussed in Section 4.3.1 based on these maximum principal contour maps. The maximum principal strain contour map for prism A150G-5 could not be obtained due to problematic load input that caused the prism to fail instantaneously. Table 4C-1 presents the cracking load, P_{cr} , and maximum load, P_{max} , for all of the individual prisms obtained with the help of maximum principal strain contour maps as explained in Section 4.3.1. The load resisting ability of prisms within each test series after the appearance of cracking is discussed in Section 4.3.1 based on the resulting P_{max}/P_{cr} ratios.

Stress versus Strain Characteristics

Figures 4C-16 to 4C-30 show the axial stress versus principal strain plots within the exterior web face and face shell plane of prisms as obtained from the analysis of DIC images. Both maximum principal strain, ε_{max} , and minimum principal strain, ε_{min} , are included within each plot. The discussion on the mechanical behavior of prisms within each test series based on these plots is included in Section 4.3.2. Axial stress versus principal strain plot for prism A150G-5 could not be obtained due to problematic load input that caused the prism to fail instantaneously.

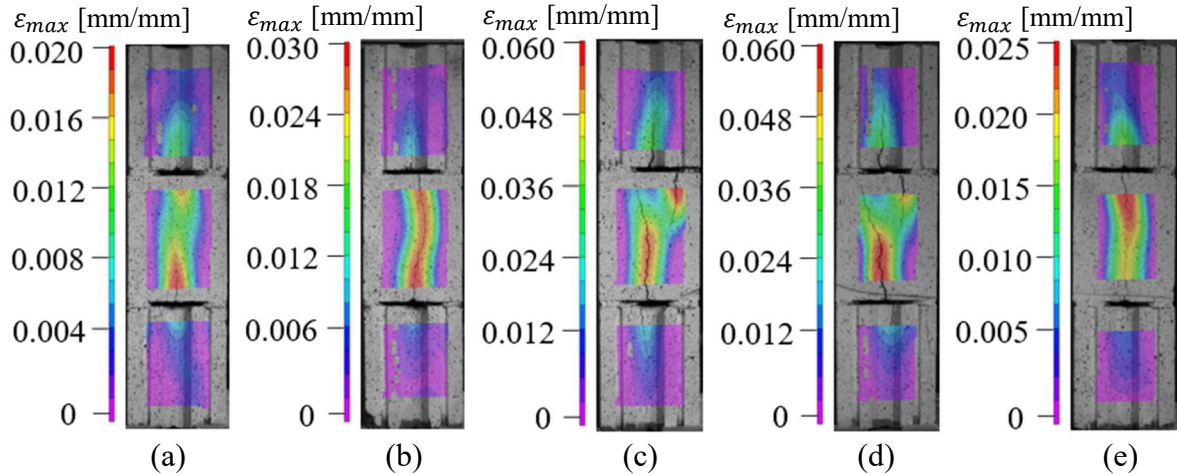


Figure 4C-1: Maximum Principal Strain Contour Map at Peak Load on Web Face for Prisms: (a) A150H-1, (b) A150H-2, (c) A150H-3, (d) A150H-4, and (e) A150H-5

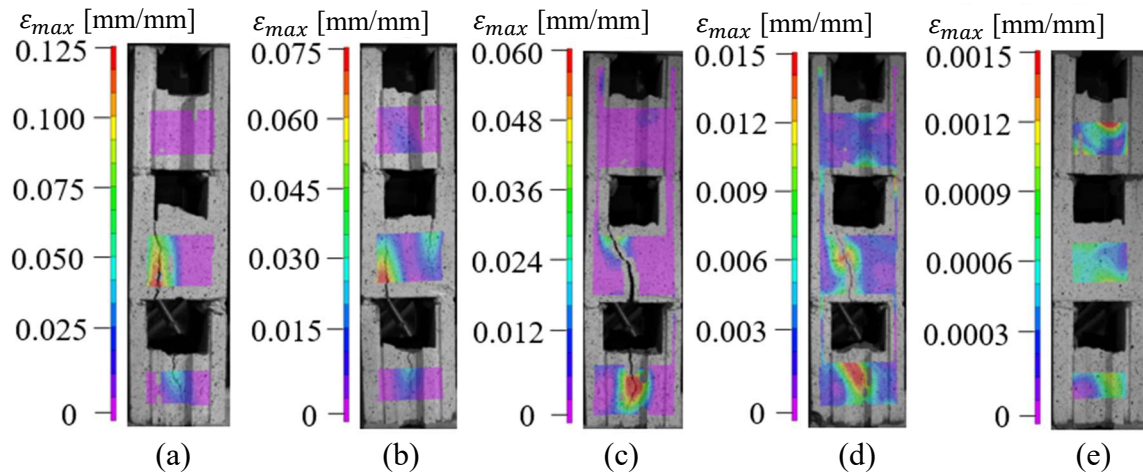


Figure 4C-2: Maximum Principal Strain Contour Map at Peak Load on Web Face for Prisms: (a) B150H-1, (b) B150H-2, (c) B150H-3, (d) B150H-4, and (e) B150H-5

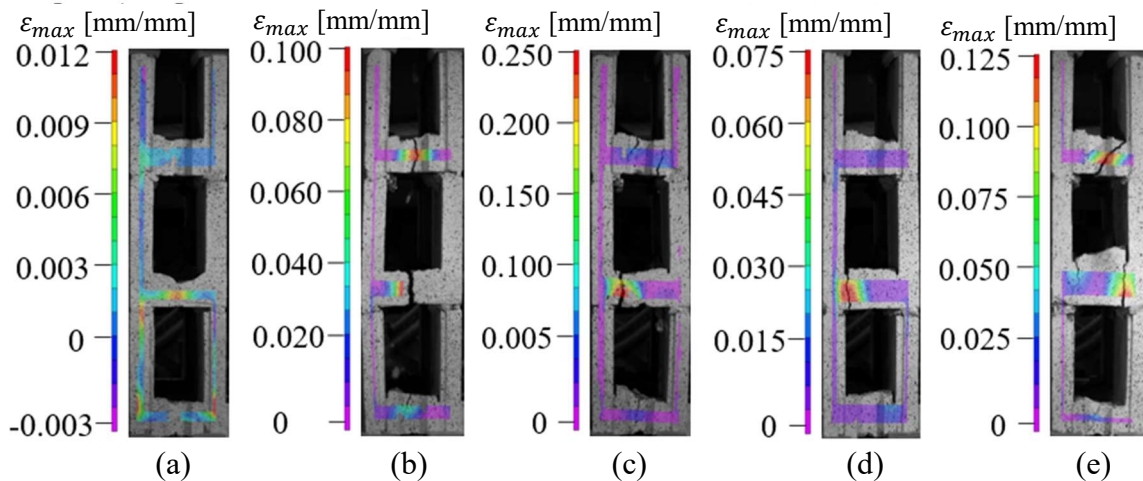


Figure 4C-3: Maximum Principal Strain Contour Map at Peak Load on Web Face for Prisms: (a) C150H-1, (b) C150H-2, (c) C150H-3, (d) C150H-4, and (e) C150H-5

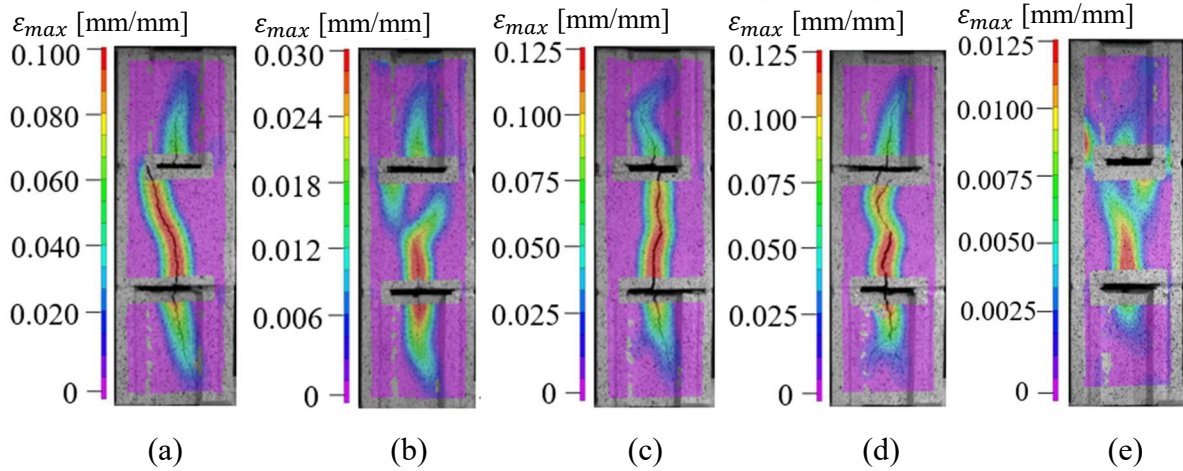


Figure 4C-3: Maximum Principal Strain Contour Map at Peak Load on Web Face for Prisms: (a) A200H-1, (b) A200H-2, (c) A200H-3, (d) A200H-4, and (e) A200H-5

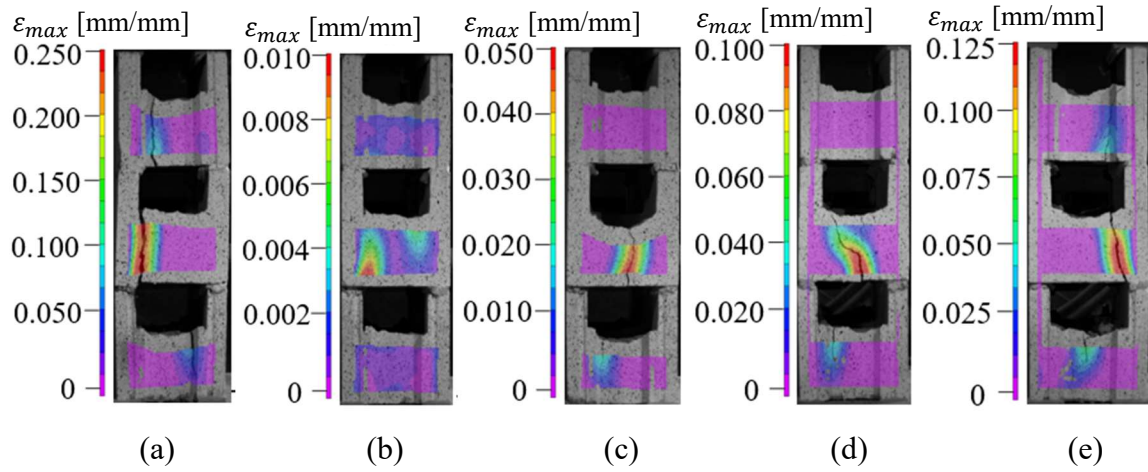


Figure 4C-5: Maximum Principal Strain Contour Map at Peak Load on Web Face for Prisms: (a) B200H-1, (b) B200H-2, (c) B200H-3, (d) B200H-4, and (e) B200H-5

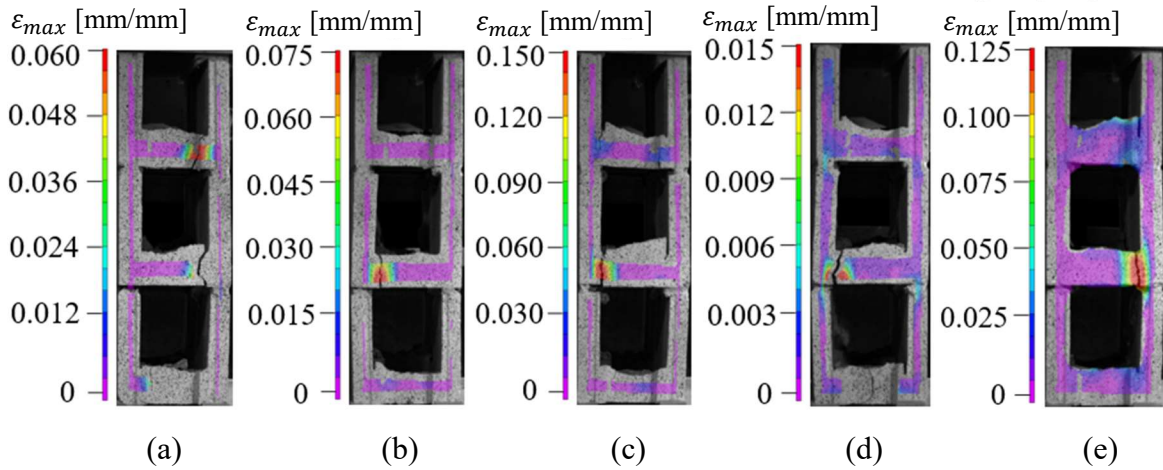


Figure 4C-6: Maximum Principal Strain Contour Map at Peak Load on Web Face for Prisms: (a) C200H-1, (b) C200H-2, (c) C200H-3, (d) C200H-4, and (e) C200H-5

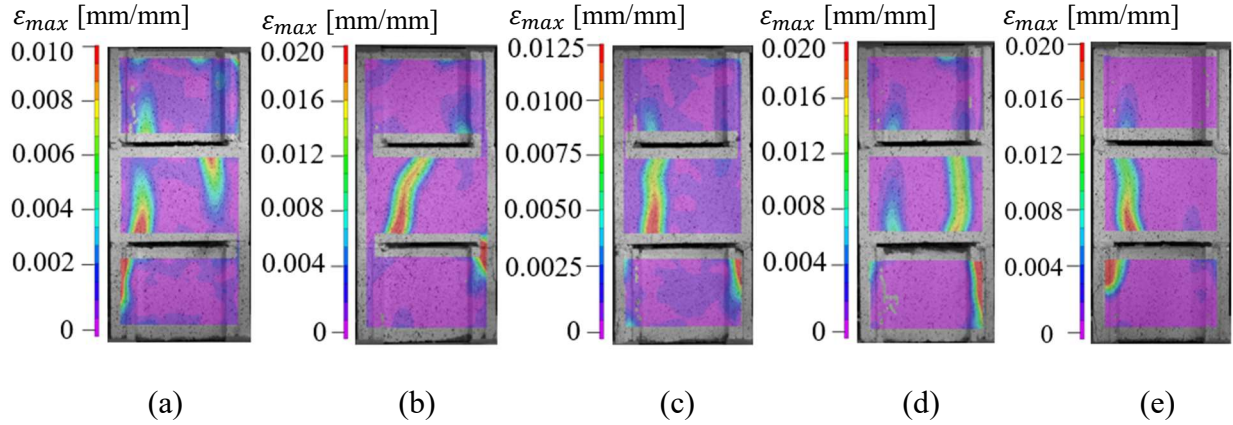


Figure 4C-7: Maximum Principal Strain Contour Map at Peak Load on Web Face for Prisms: (a) A300H-1, (b) A300H-2, (c) A300H-3, (d) A300H-4, and (e) A300H-5

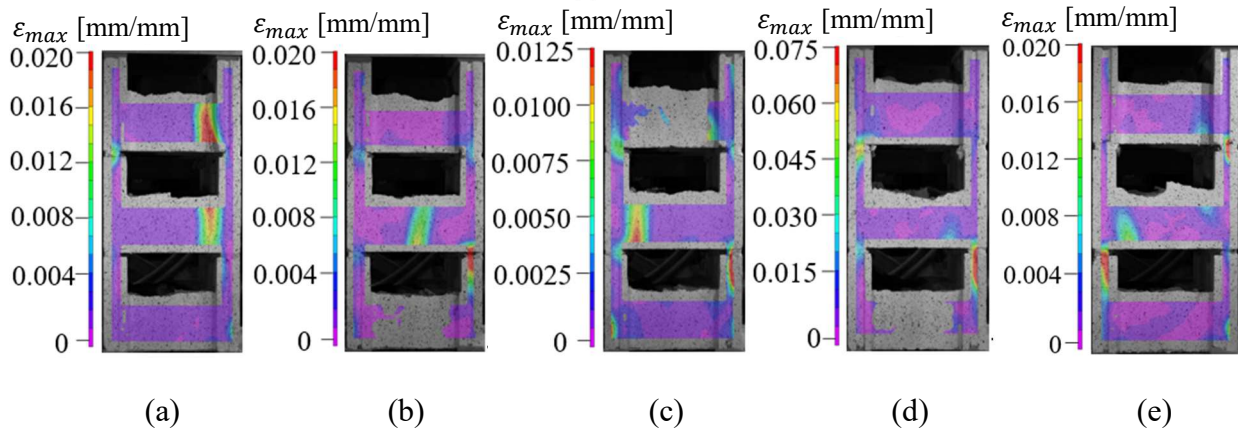


Figure 4C-8: Maximum Principal Strain Contour Map at Peak Load on Web Face for Prisms: (a) B300H-1, (b) B300H-2, (c) B300H-3, (d) B300H-4, and (e) B300H-5

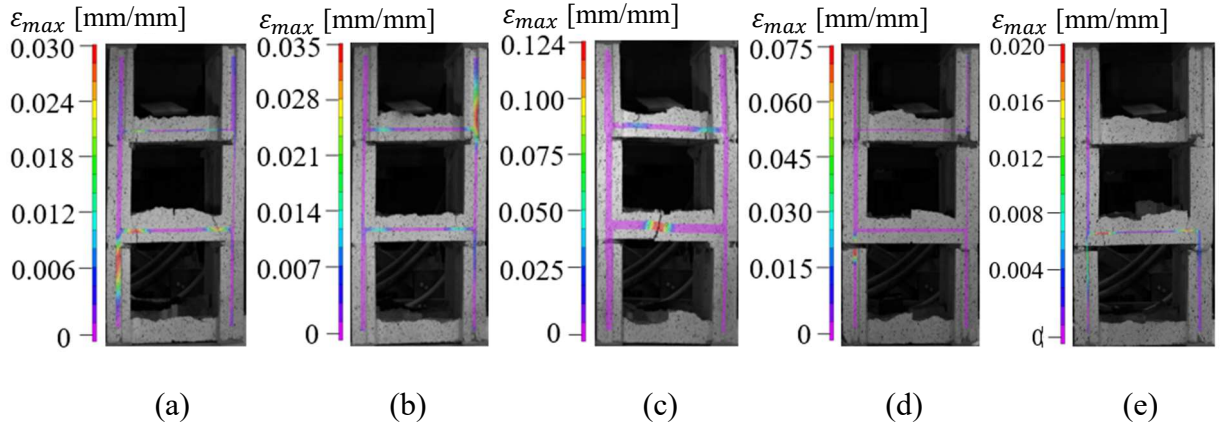


Figure 4C-9: Maximum Principal Strain Contour Map at Peak Load on Web Face for Prisms: (a) C300H-1, (b) C300H-2, (c) C300H-3, (d) C300H-4, and (e) C300H-5

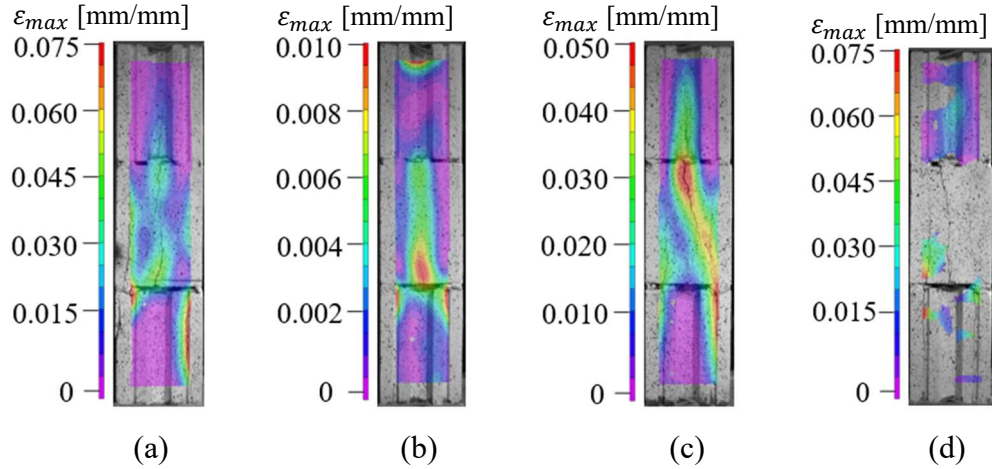


Figure 4C-10: Maximum Principal Strain Contour Map at Peak Load on Web Face for Prisms: (a) A150G-1, (b) A150G-2, (c) A150G-3, (d) A150G-4, and (e) A150G-5

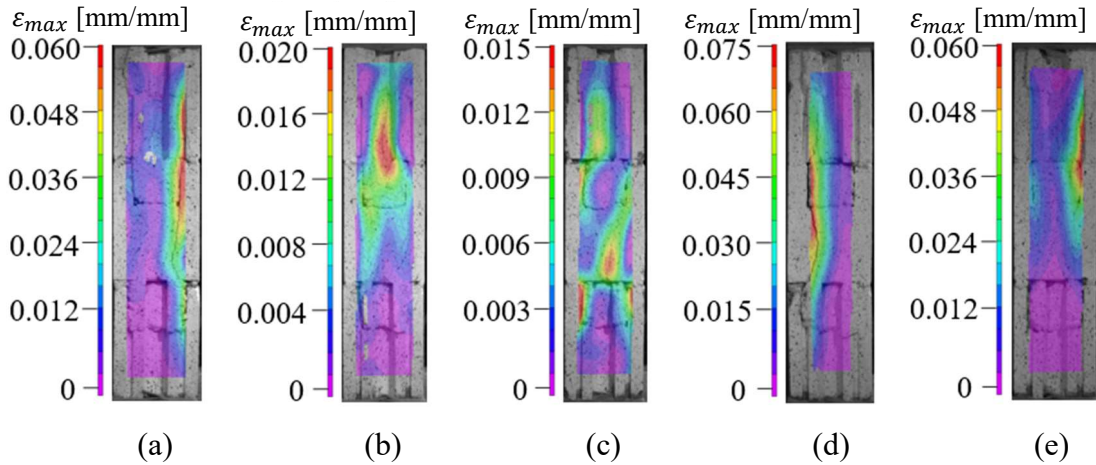


Figure 4C-11: Maximum Principal Strain Contour Map at Peak Load on Web Face for Prisms: (a) B150G-1, (b) B150G-2, (c) B150G-3, (d) B150G-4, and (e) B150G-5

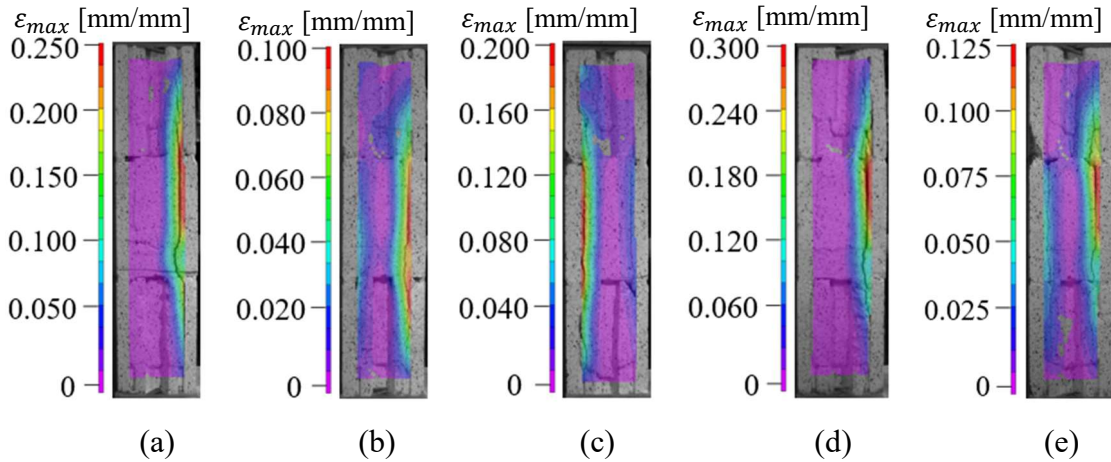


Figure 4C-12: Maximum Principal Strain Contour Map at Peak Load on Web Face for Prisms: (a) C150G-1, (b) C150G-2, (c) C150G-3, (d) C150G-4, and (e) C150G-5

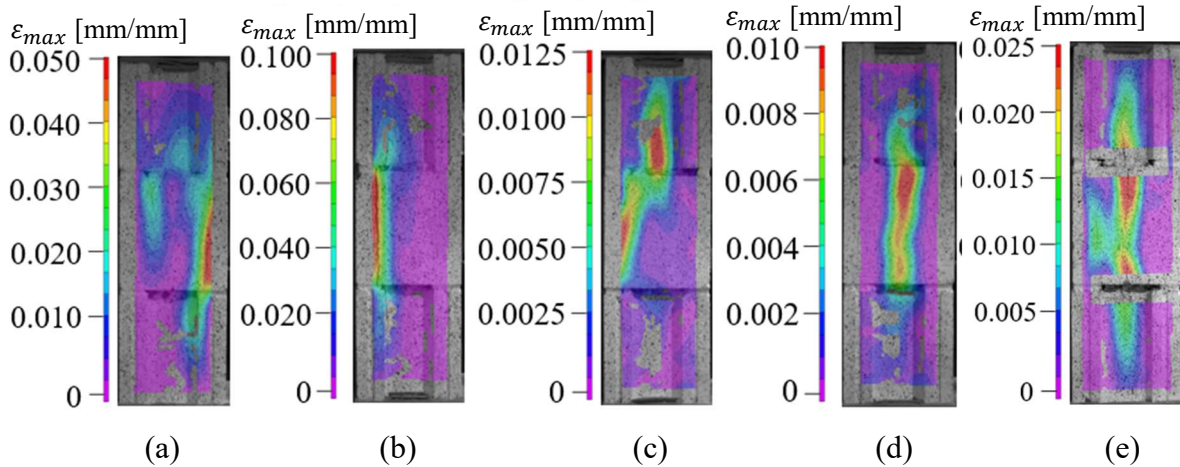


Figure 4C-13: Maximum Principal Strain Contour Map at Peak Load on Web Face for Prisms: (a) A200G-1, (b) A200G-2, (c) A200G-3, (d) A200G-4, and (e) A200G-5

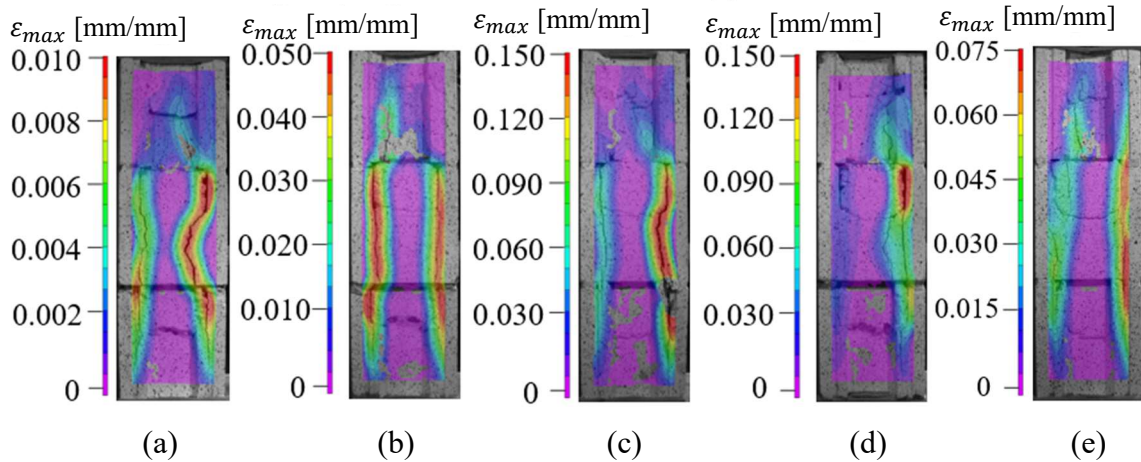


Figure 4C-14: Maximum Principal Strain Contour Map at Peak Load on Web Face for Prisms: (a) B200G-1, (b) B200G-2, (c) B200G-3, (d) B200G-4, and (e) B200G-5

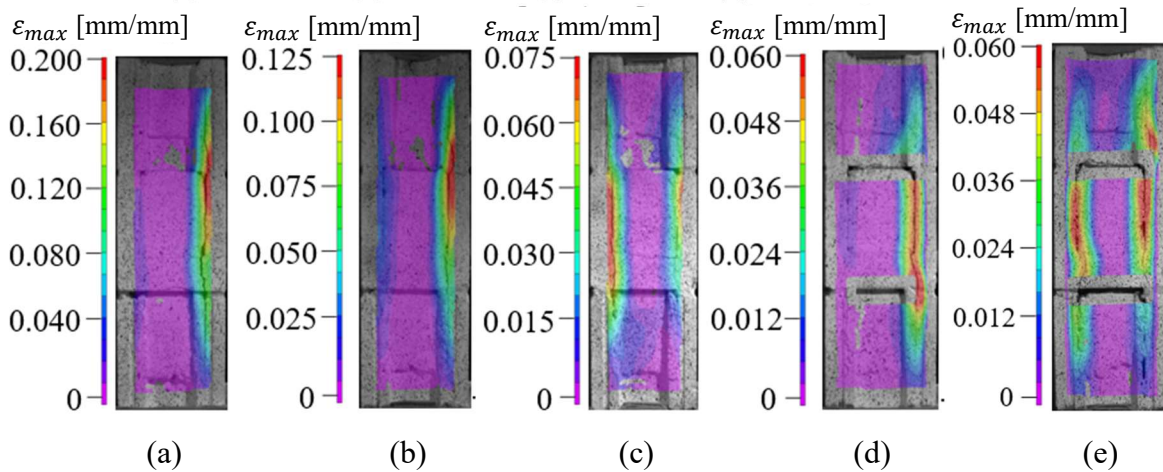
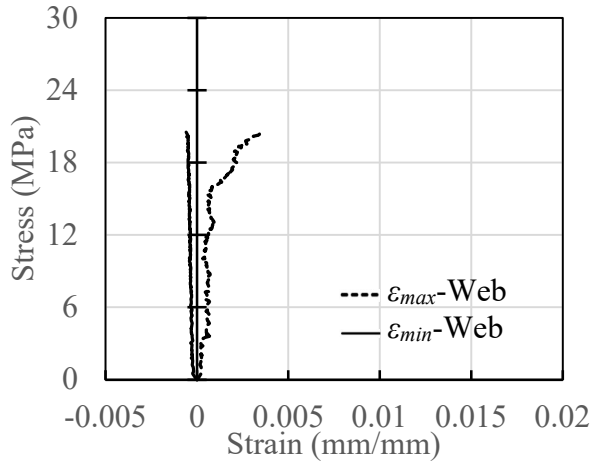


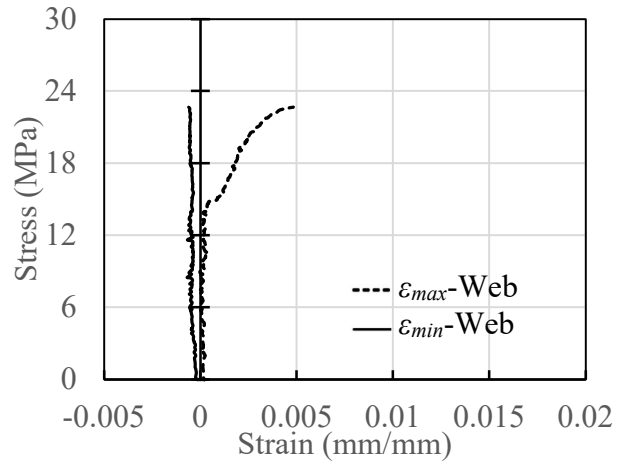
Figure 4C-15: Maximum Principal Strain Contour Map at Peak Load on Web Face for Prisms: (a) C200G-1, (b) C200G-2, (c) C200G-3, (d) C200G-4, and (e) C200G-5

Table 4C-1: Summary of Initial Cracking and Peak Load

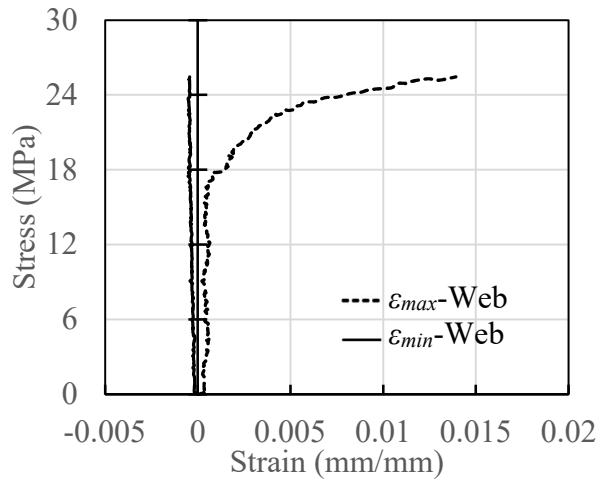
Test Series	Initial Cracking Load, P_{cr}					Mean (kN)	COV (%)	Peak Load, P_{max}					Mean (kN)	COV (%)
	(kN)							(kN)						
	#1	#2	#3	#4	#5			#1	#2	#3	#4	#5		
A150H	218	239	323	262	338	276	19.0	439	485	545	501	586	511	11.1
B150H	199	241	275	364	N/A	270	26.0	250	325	407	419	N/A	350	22.6
C150H	267	253	245	429	214	282	30.1	404	373	263	545	246	366	33.0
A200H	311	308	429	302	330	336	15.9	745	556	766	581	739	678	14.8
B200H	376	421	278	373	364	362	14.4	578	543	708	599	561	598	10.9
C200H	291	328	192	306	337	291	20.0	300	377	294	317	408	339	15.0
A300H	732	803	619	636	504	659	17.4	897	957	823	862	744	857	9.33
B300H	678	576	635	495	610	599	11.6	929	926	896	839	861	890	4.50
C300H	256	468	360	373	386	369	20.5	744	876	708	740	773	768	8.40
A150G	490	823	726	558	N/A	649	23.5	811	1040	901	845	N/A	900	11.3
B150G	742	774	663	837	724	748	8.56	1030	1090	1080	1010	959	1030	5.36
C150G	669	831	490	663	557	642	20.2	748	987	853	874	900	872	9.89
A200G	630	738	870	595	595	686	17.3	1140	1120	1040	1200	1060	1110	5.81
B200G	679	845	685	612	916	747	17.1	970	1170	1030	989	1220	1080	10.4
C200G	864	883	964	853	752	863	8.79	1180	1010	1190	1220	1060	1130	8.13



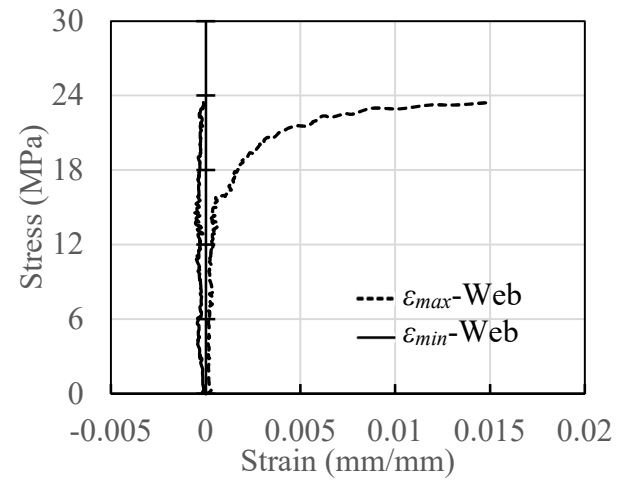
(a)



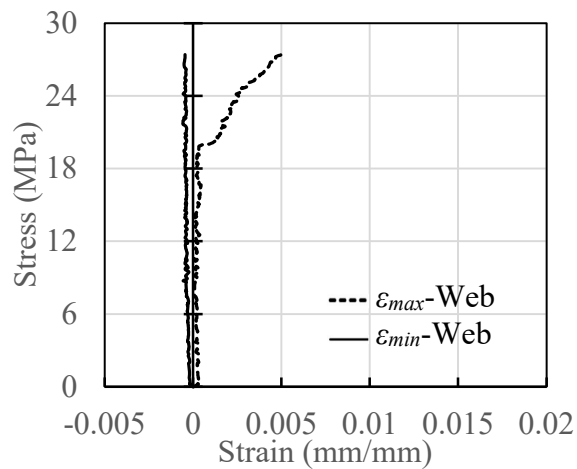
(b)



(c)

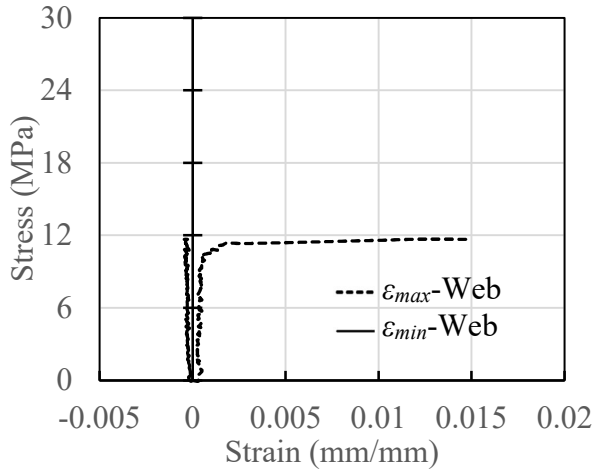


(d)

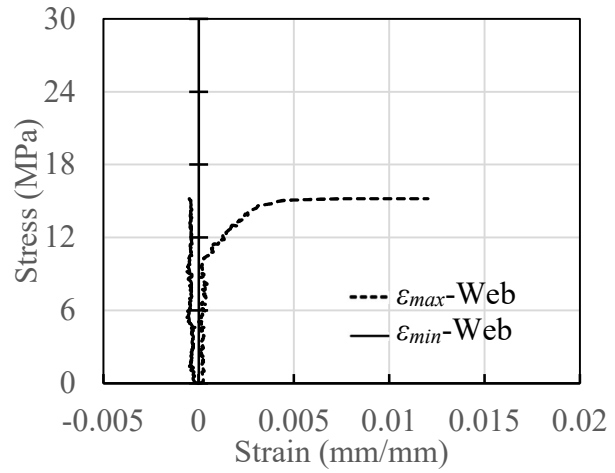


(e)

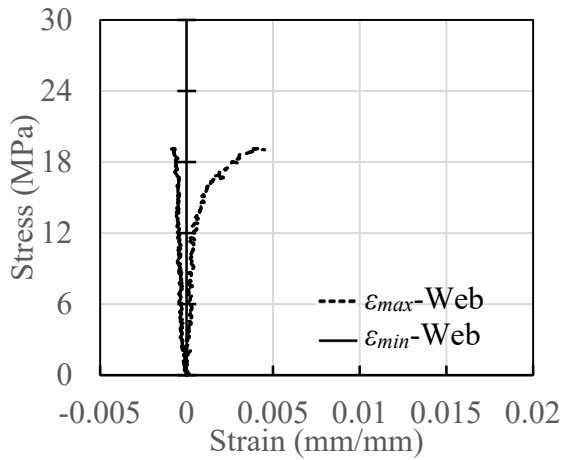
Figure 4C-16: Axial Stress versus Principal Strain Plot for Prisms: (a) A150H-1, (b) A150H-2, (c) A150H-3, (d) A150H-4, and (e) A150H-5



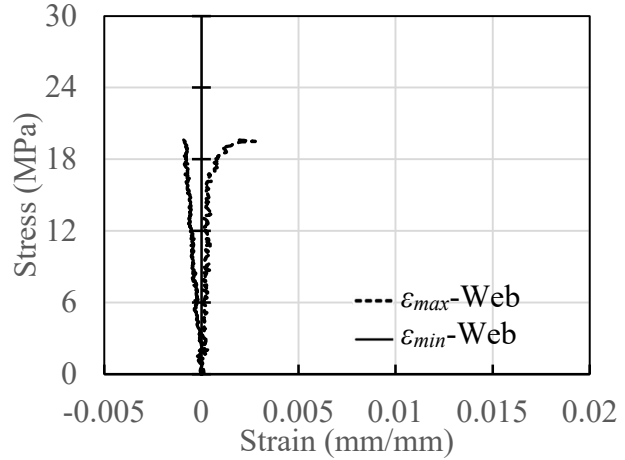
(a)



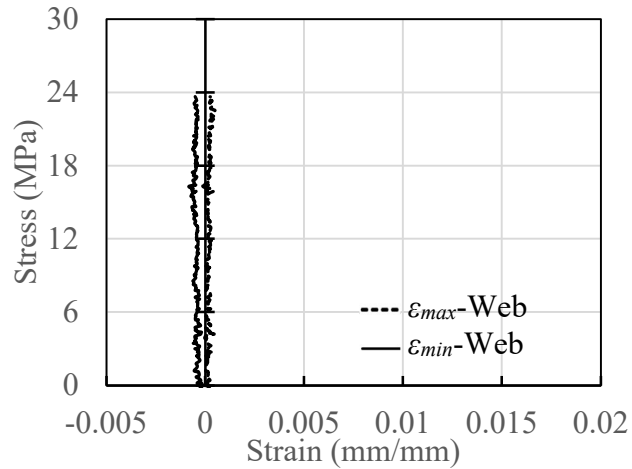
(b)



(c)

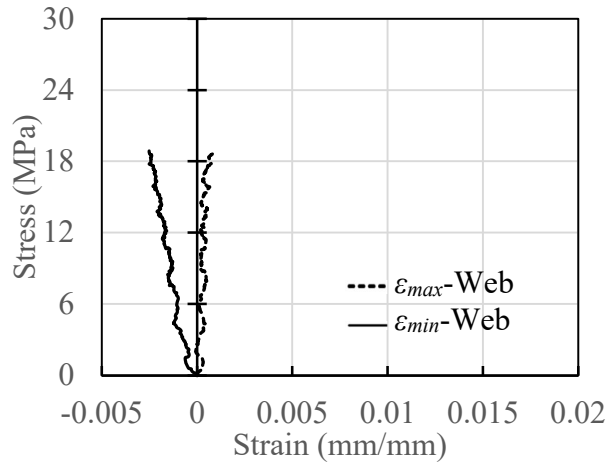


(d)

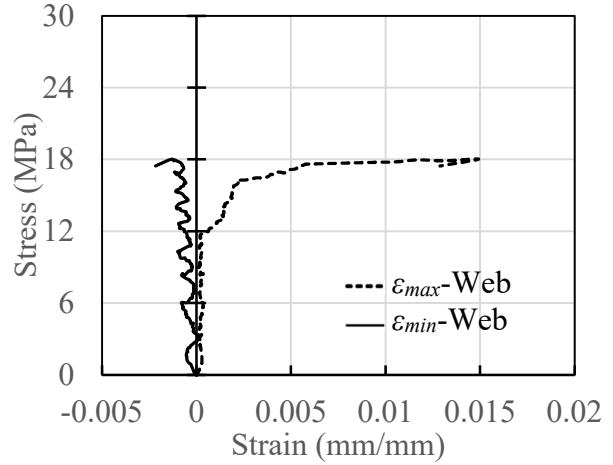


(e)

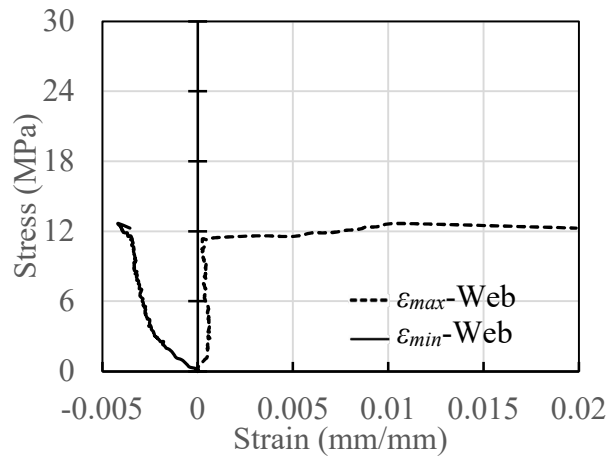
Figure 4C-17: Axial Stress versus Principal Strain Plot for Prisms: (a) B150H-1, (b) B150H-2, (c) B150H-3, (d) B150H-4, and (e) B150H-5



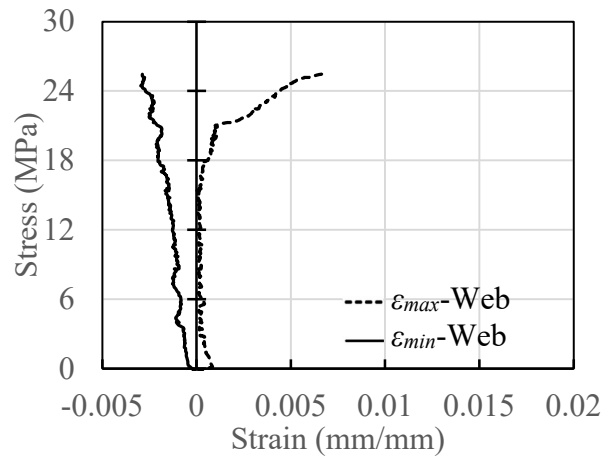
(a)



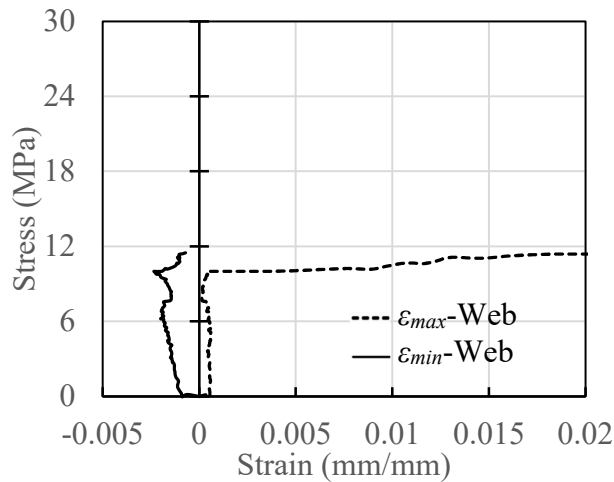
(b)



(c)



(d)



(e)

Figure 4C-18: Axial Stress versus Principal Strain Plot for Prisms: (a) C150H-1, (b) C150H-2, (c) C150H-3, (d) C150H-4, and (e) C150H-5

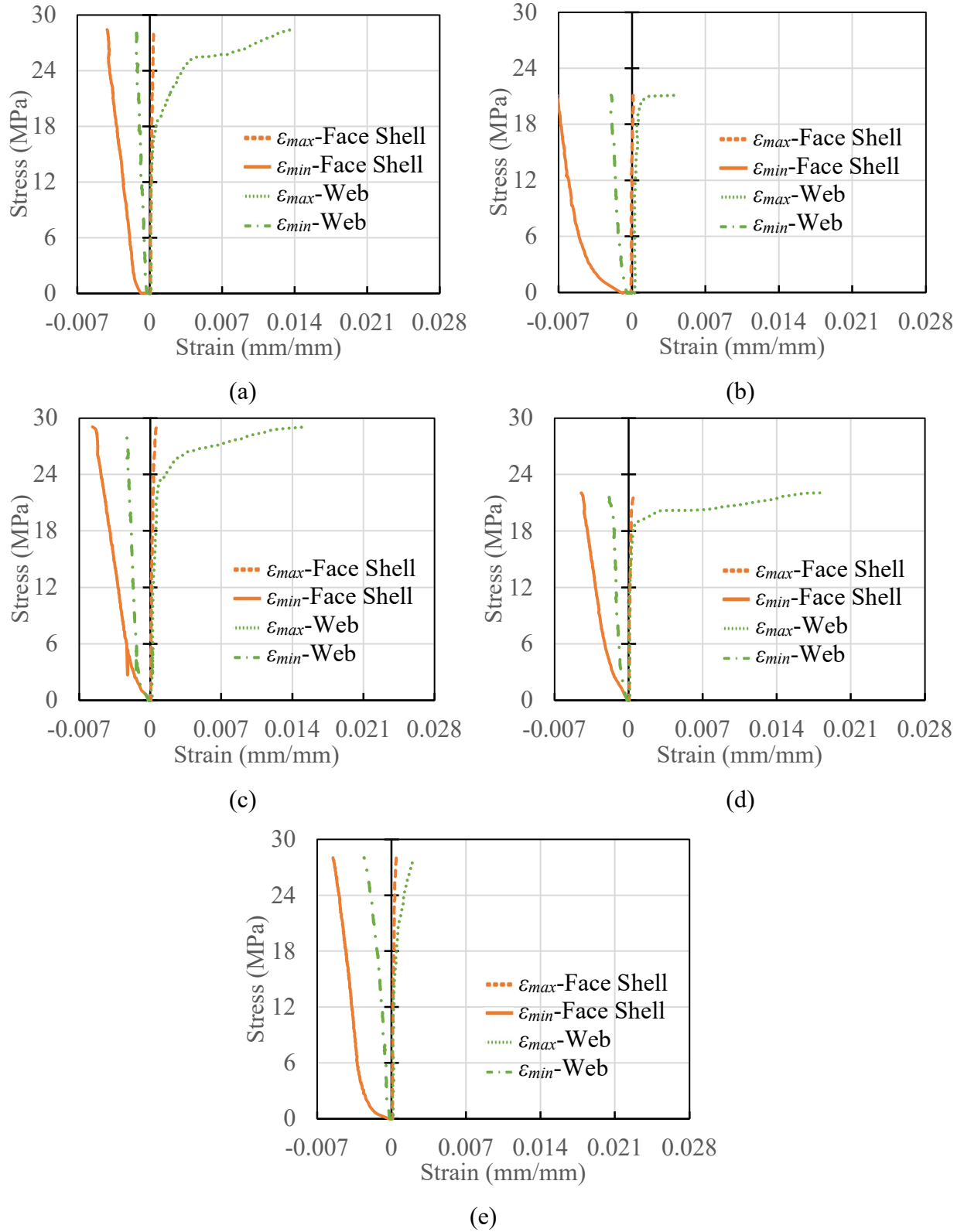
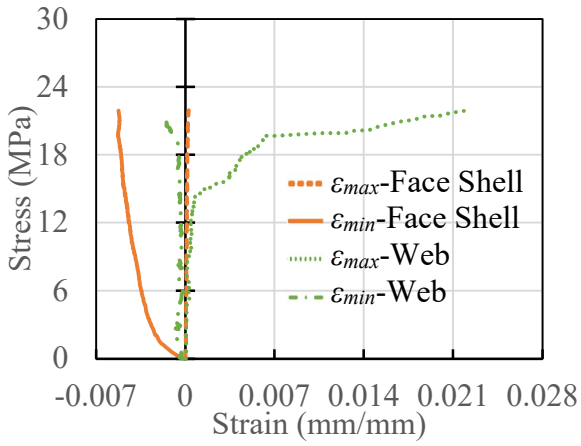
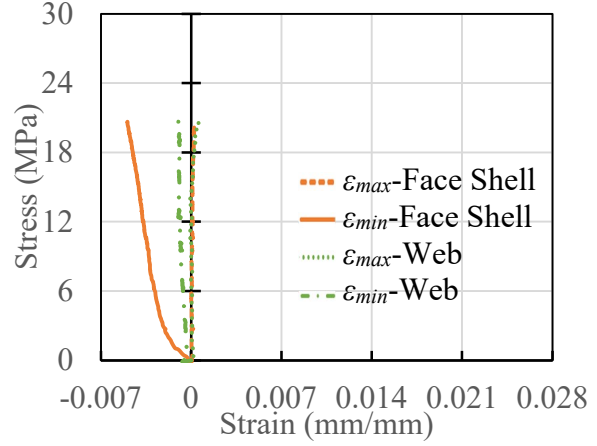


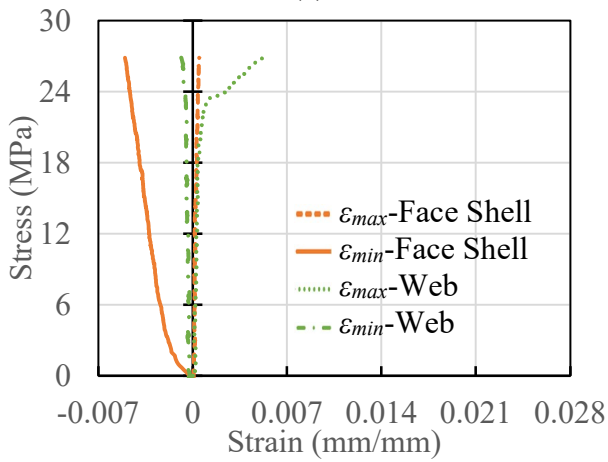
Figure 4C-19: Axial Stress versus Principal Strain Plot for Prisms: (a) A200H-1, (b) A200H-2, (c) A200H-3, (d) A200H-4, and (e) A200H-5



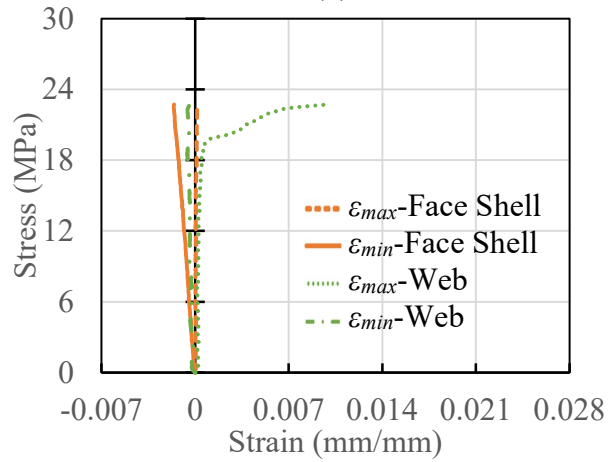
(a)



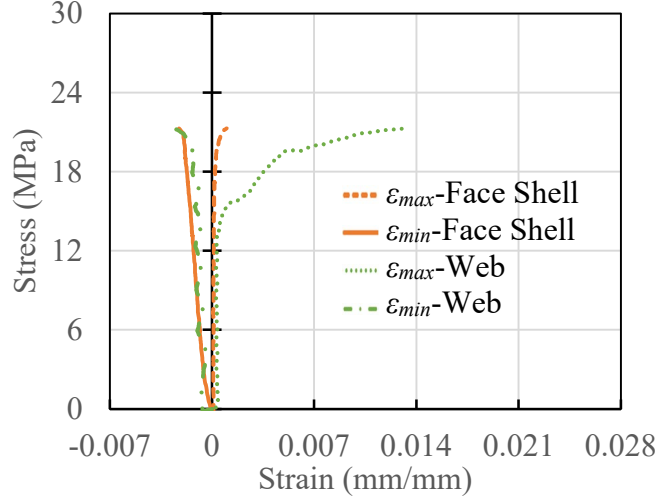
(b)



(c)



(d)



(e)

Figure 4C-20: Axial Stress versus Principal Strain Plot for Prisms: (a) B200H-1, (b) B200H-2, (c) B200H-3, (d) B200H-4, and (e) B200H-5

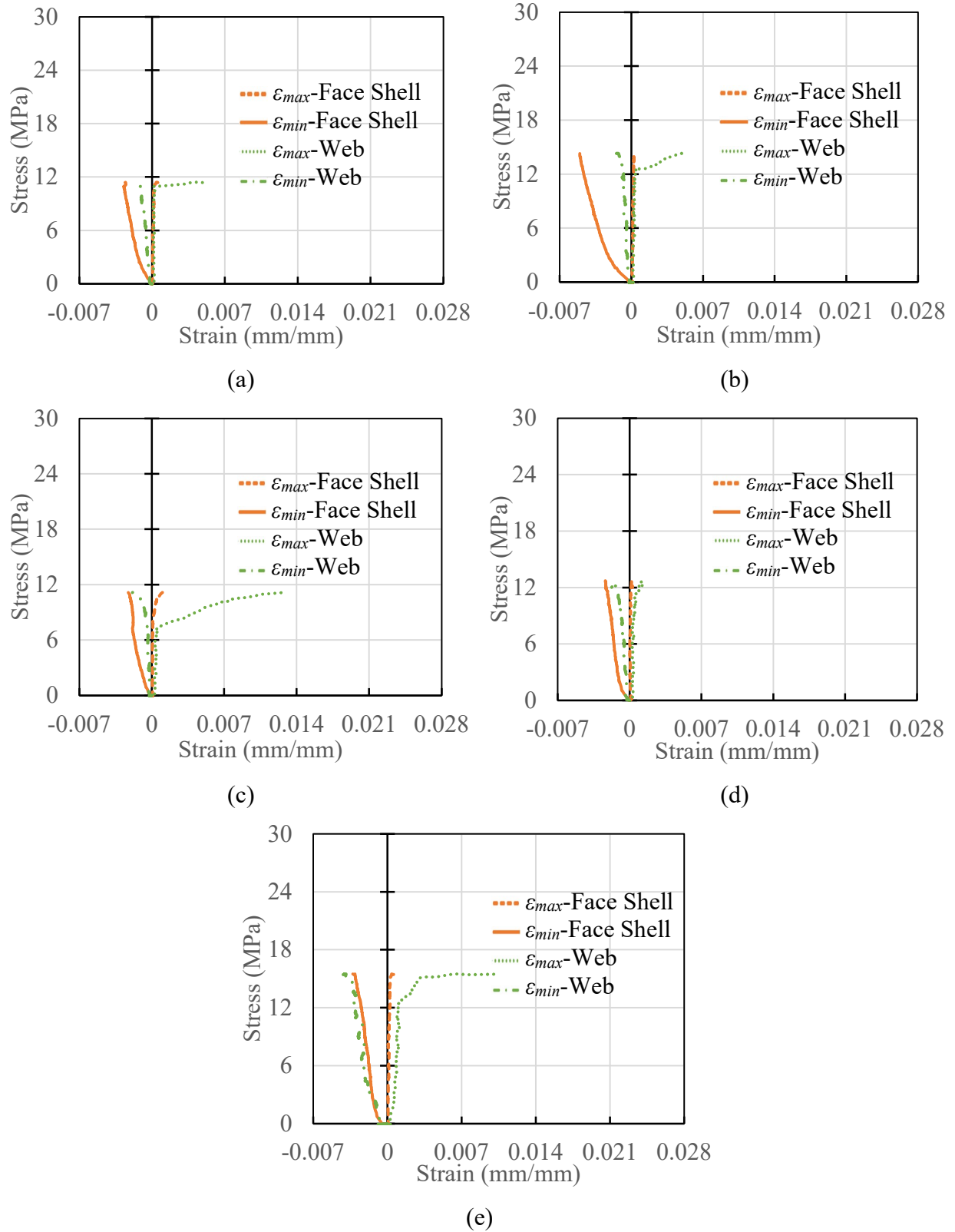


Figure 4C-21: Axial Stress versus Principal Strain Plot for Prisms: (a) C200H-1, (b) C200H-2, (c) C200H-3, (d) C200H-4, and (e) C200H-5

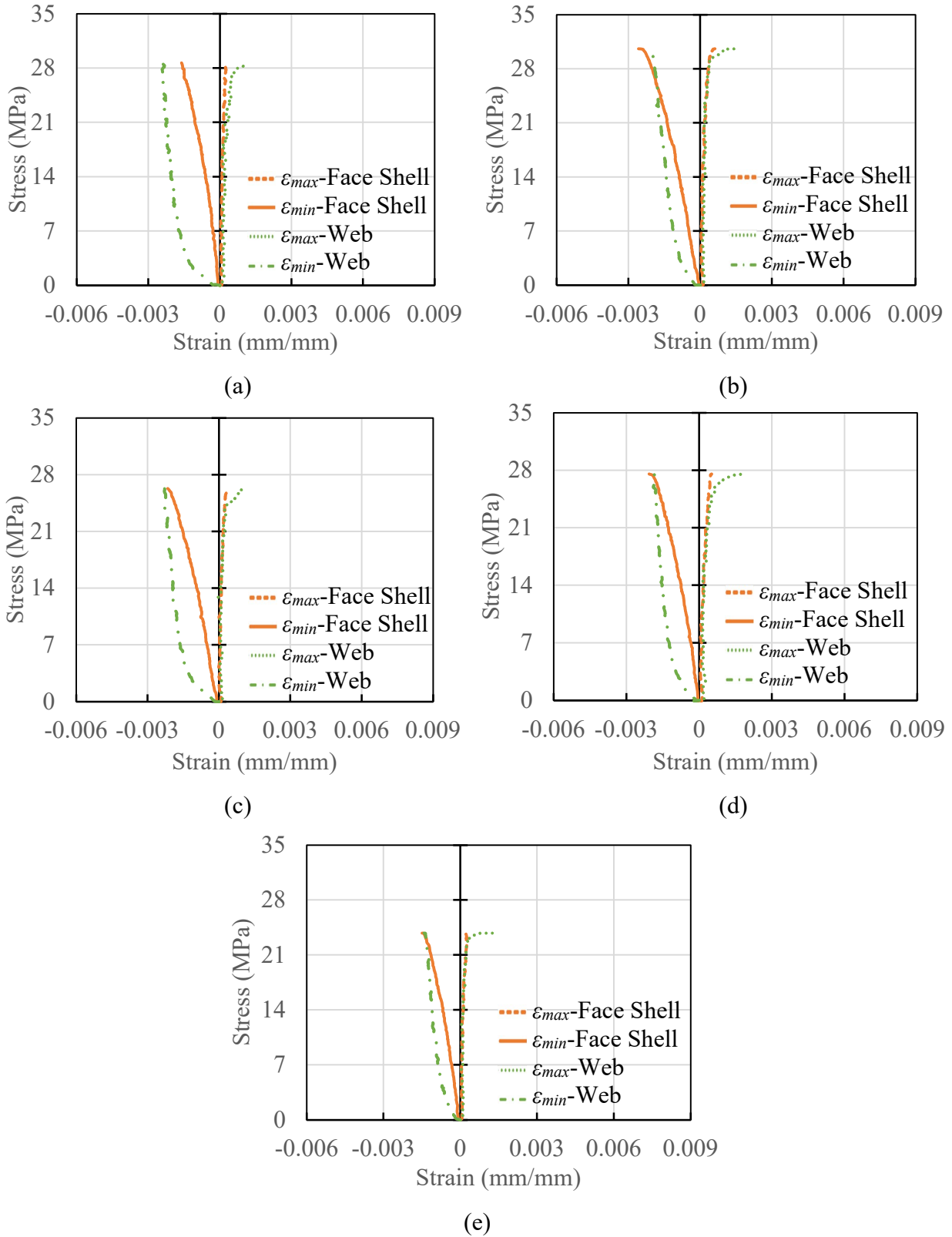


Figure 4C-22: Axial Stress versus Principal Strain Plot for Prisms: (a) A300H-1, (b) A300H-2, (c) A300H-3, (d) A300H-4, and (e) A300H-5

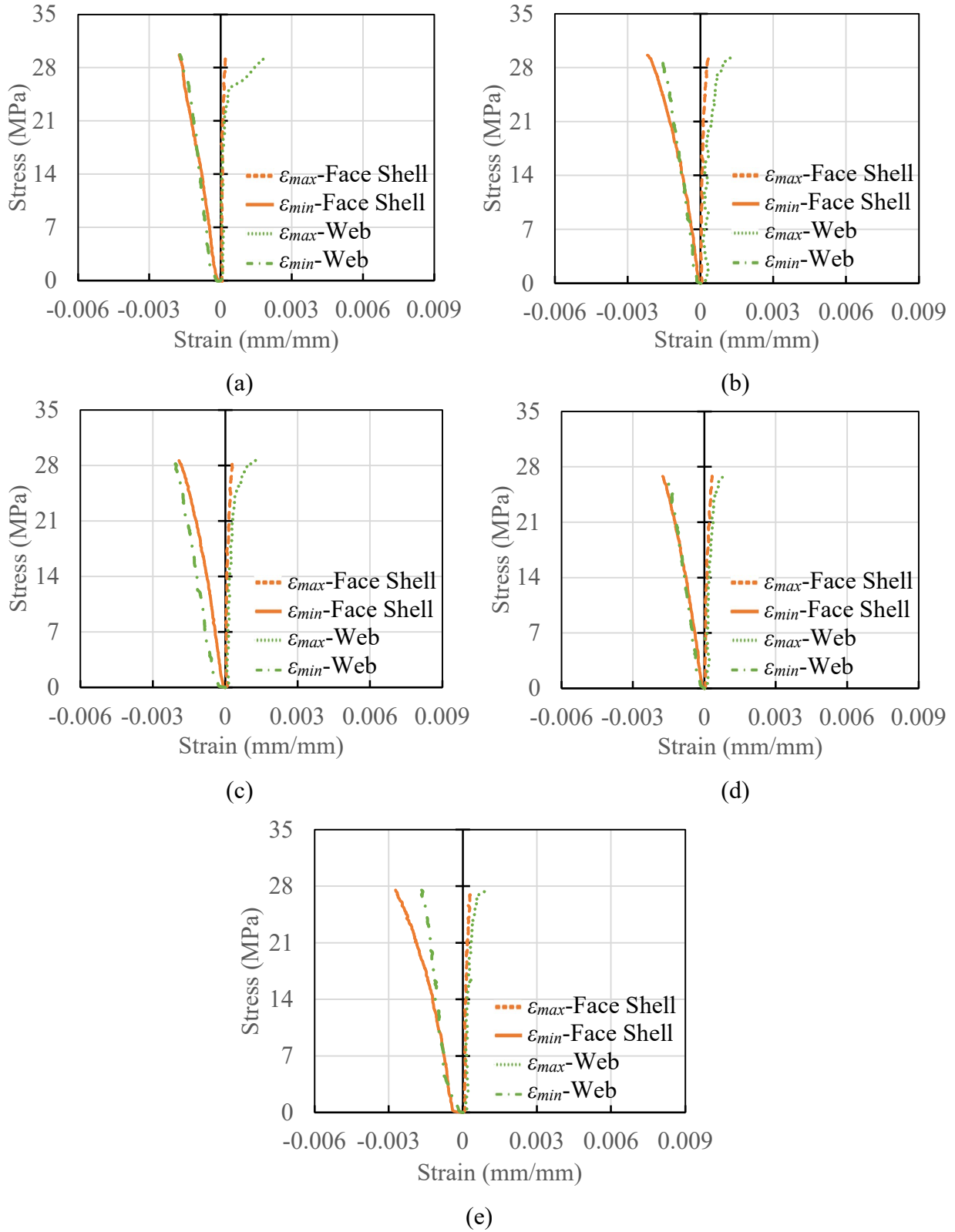


Figure 4C-23: Axial Stress versus Principal Strain Plot for Prisms: (a) B300H-1, (b) B300H-2, (c) B300H-3, (d) B300H-4, and (e) B300H-5

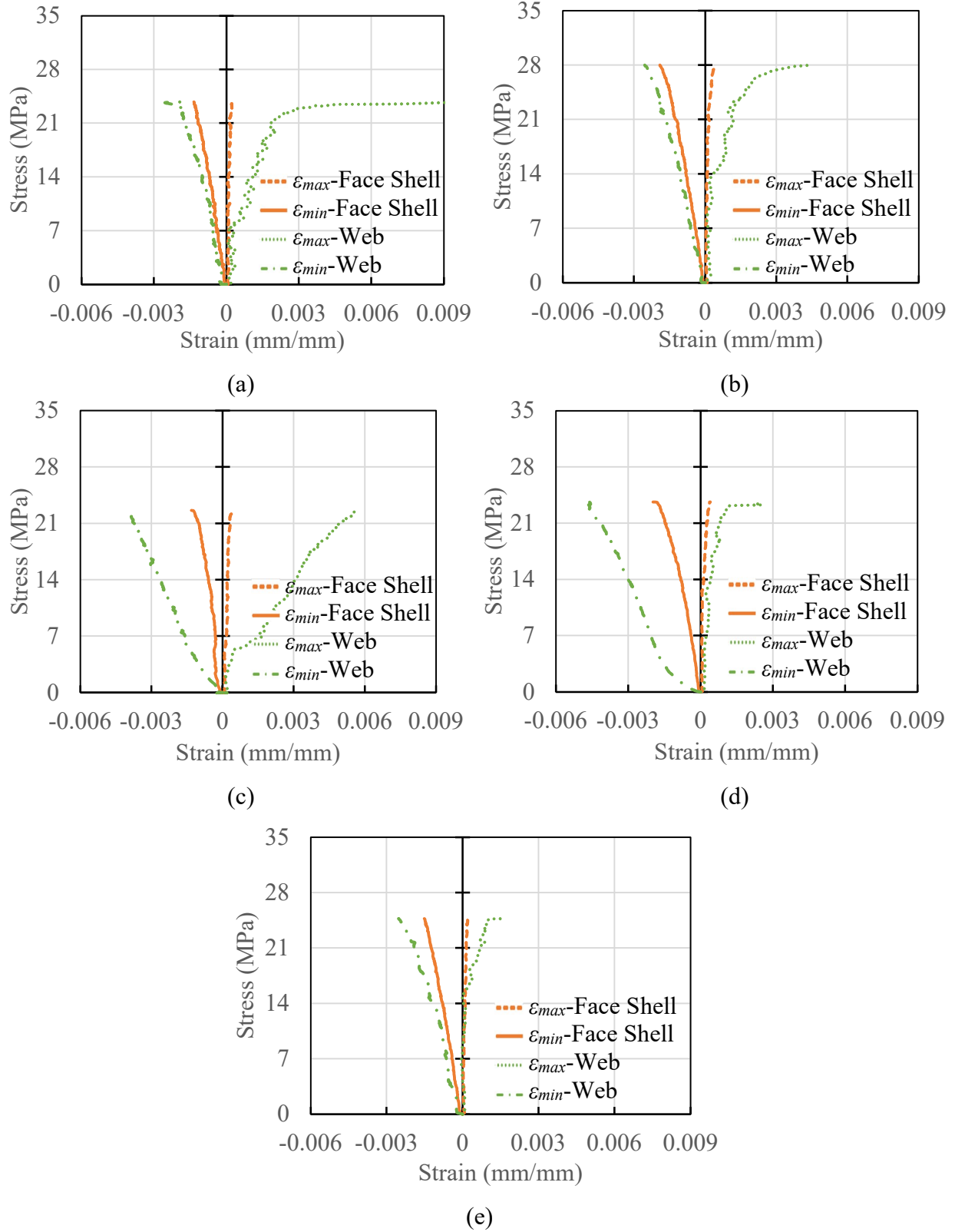
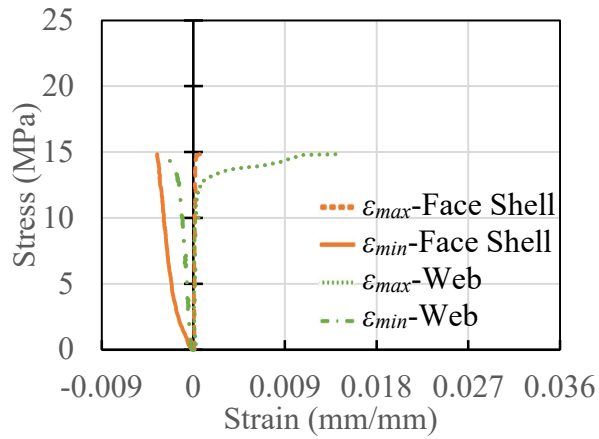
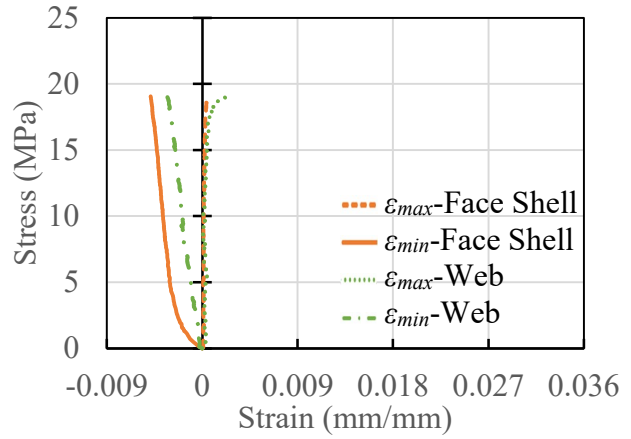


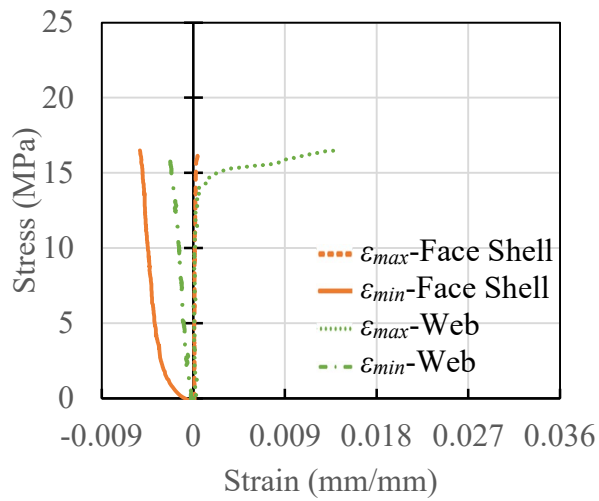
Figure 4C-24: Axial Stress versus Principal Strain Plot for Prisms: (a) C300H-1, (b) C300H-2, (c) C300H-3, (d) C300H-4, and (e) C300H-5



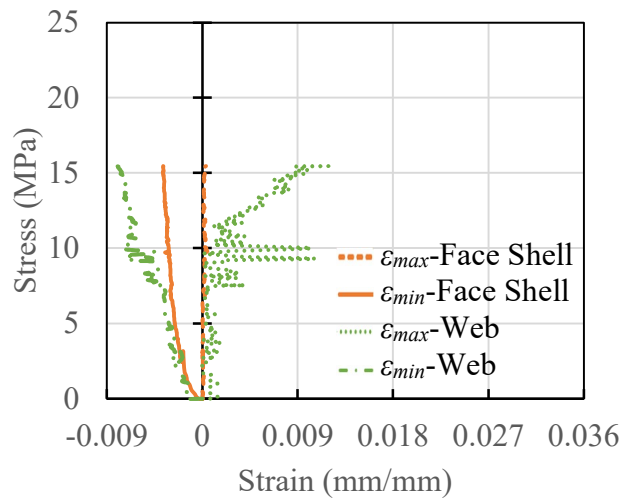
(a)



(b)

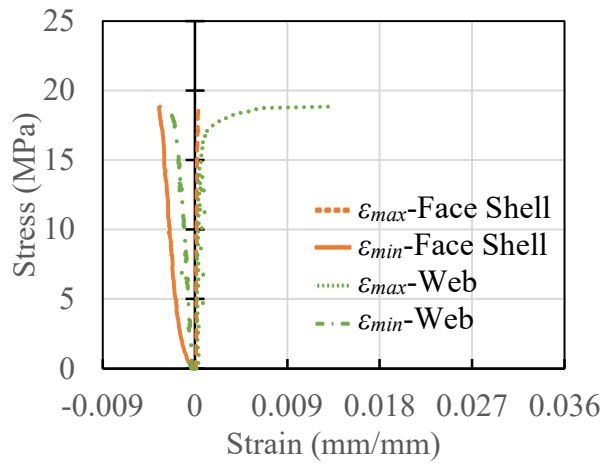


(c)

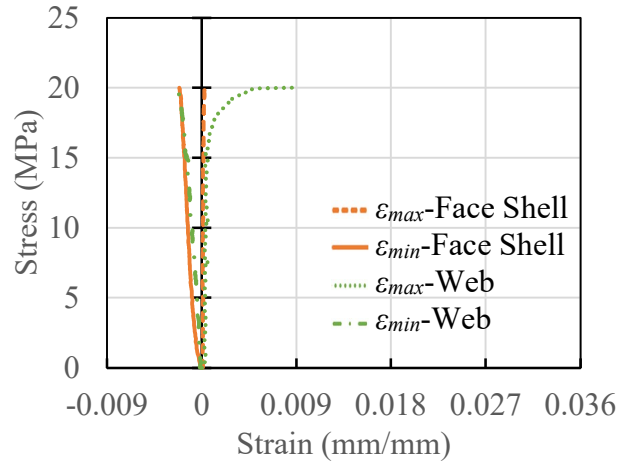


(d)

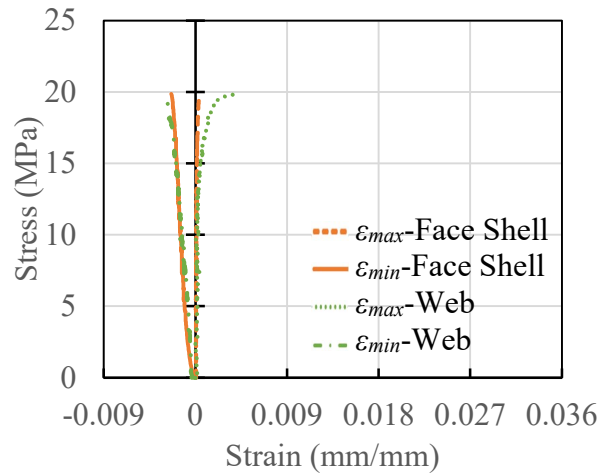
Figure 4C-25: Axial Stress versus Principal Strain Plot for Prisms: (a) A150G-1, (b) A150G-2, (c) A150G-3, and (d) A150G-4



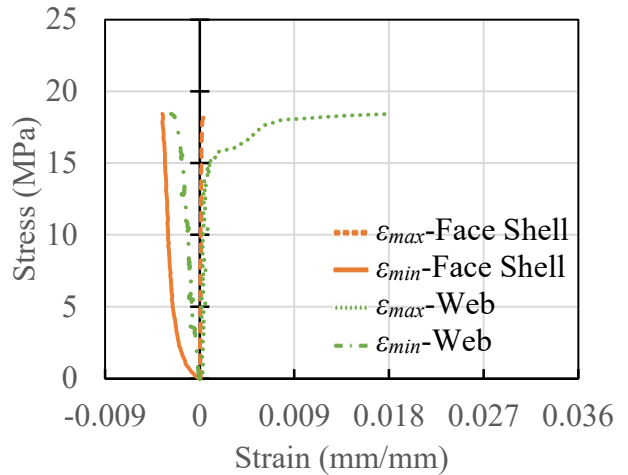
(a)



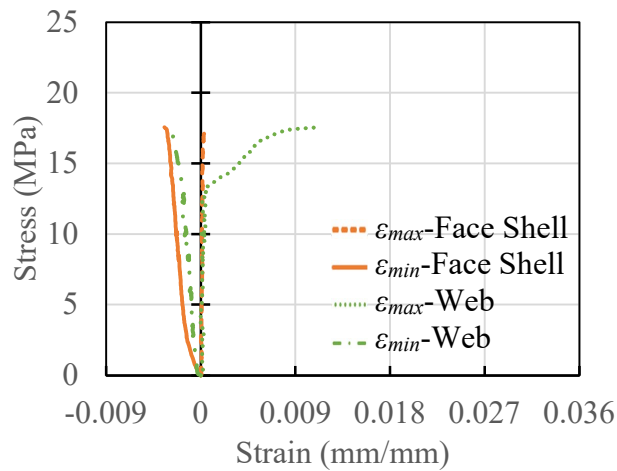
(b)



(c)

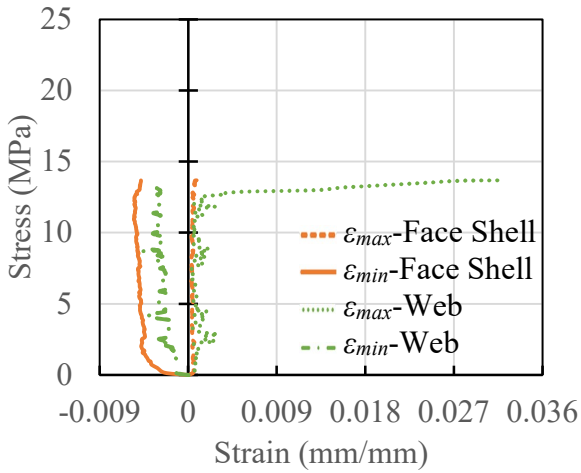


(d)

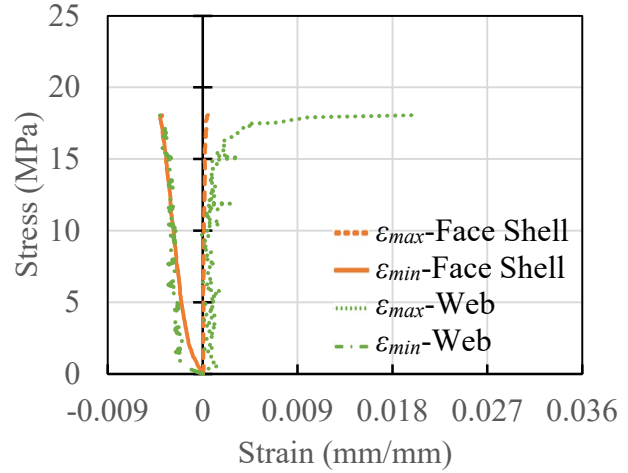


(e)

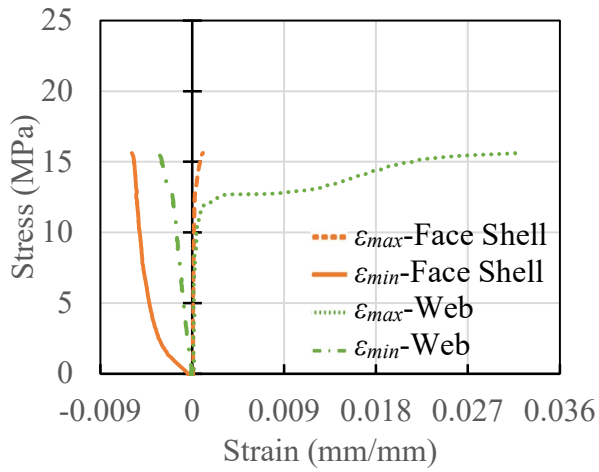
Figure 4C-26: Axial Stress versus Principal Strain Plot for Prisms: (a) B150G-1, (b) B150G-2, (c) B150G-3, (d) B150G-4, and (e) B150G-5



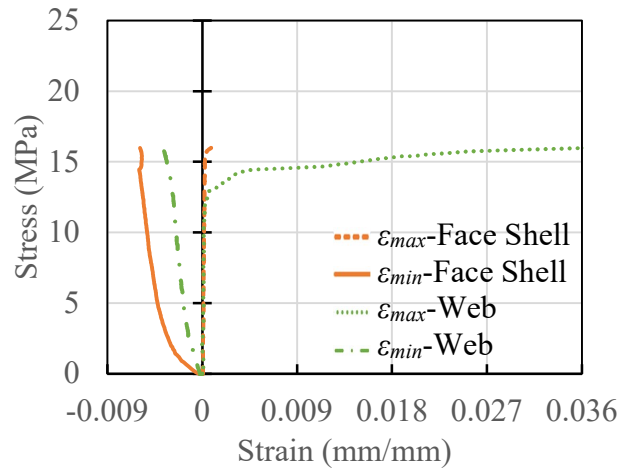
(a)



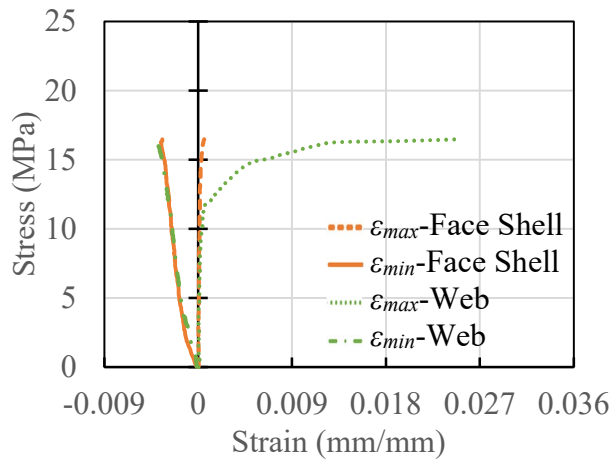
(b)



(c)

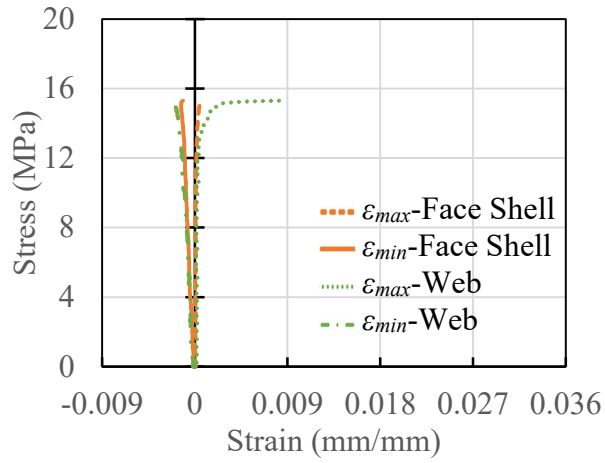


(d)

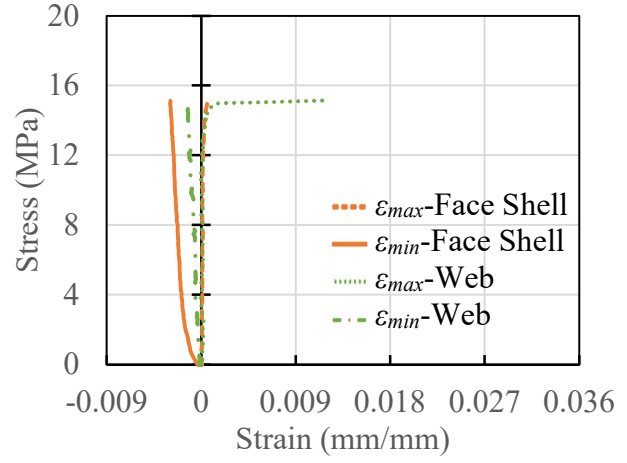


(e)

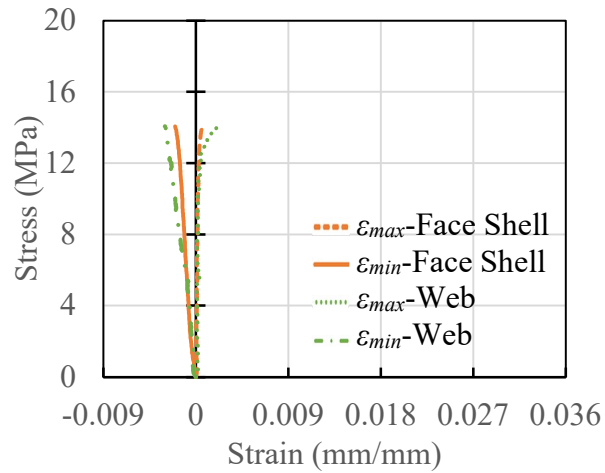
Figure 4C-27: Axial Stress versus Principal Strain Plot for Prisms: (a) C150G-1, (b) C150G-2, (c) C150G-3, (d) C150G-4, and (e) C150G-5



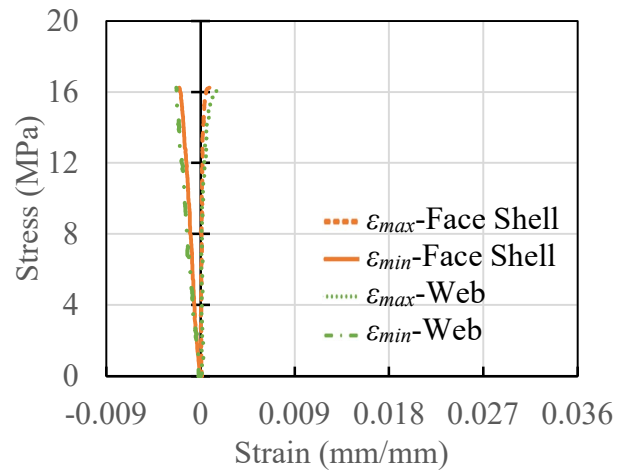
(a)



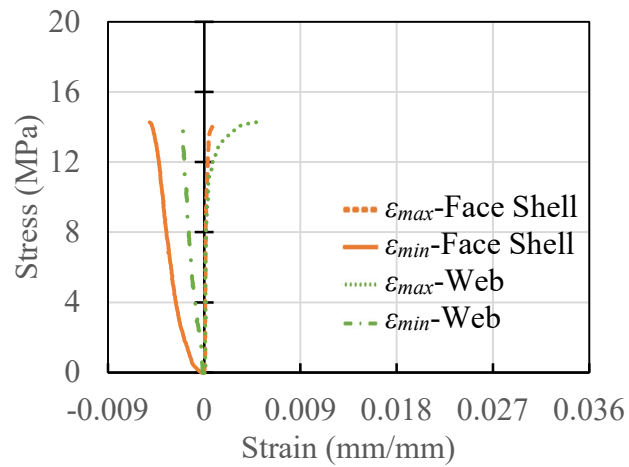
(b)



(c)

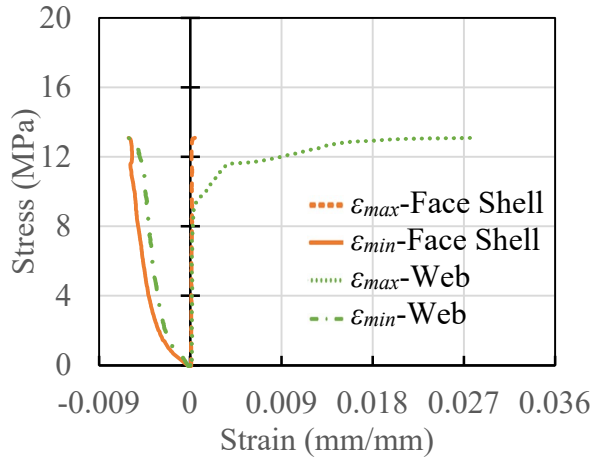


(d)

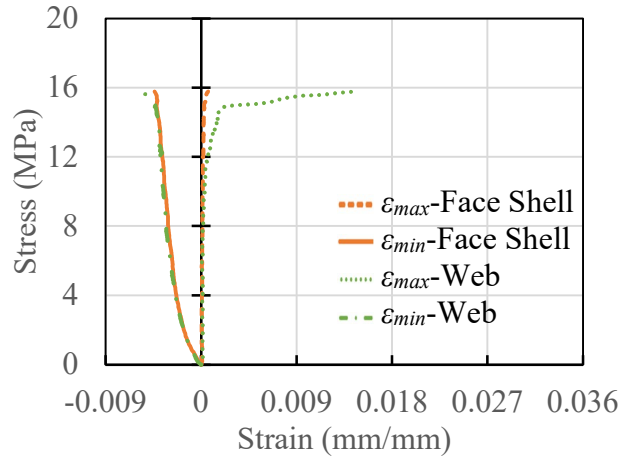


(e)

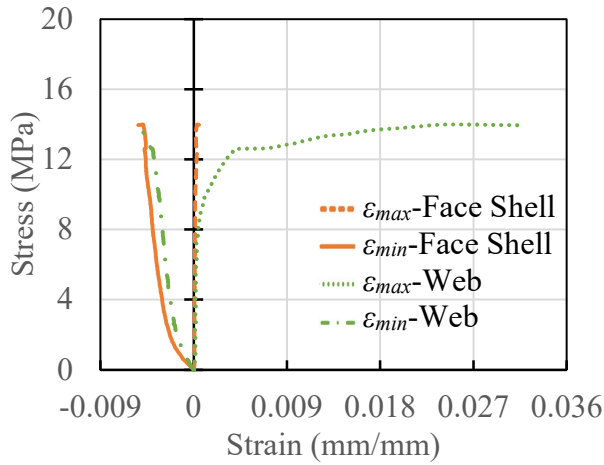
Figure 4C-28: Axial Stress versus Principal Strain Plot for Prisms: (a) A200G-1, (b) A200G-2, (c) A200G-3, (d) A200G-4, and (e) A200G-5



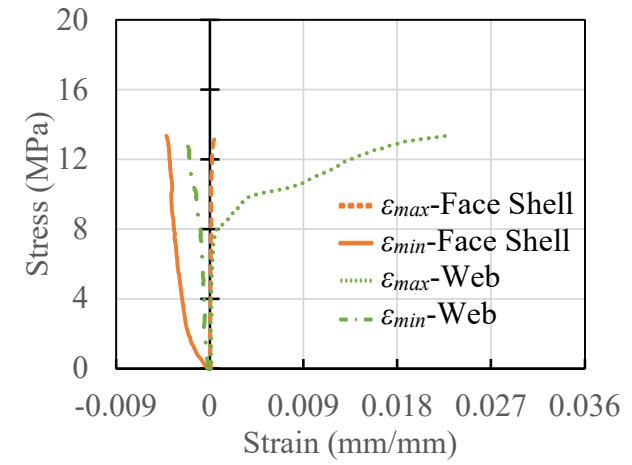
(a)



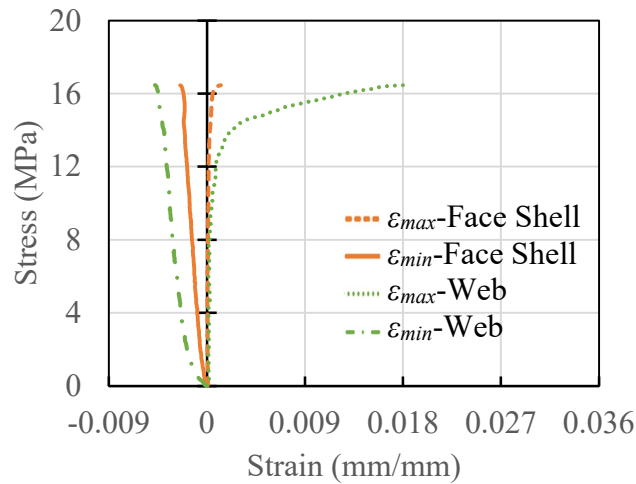
(b)



(c)

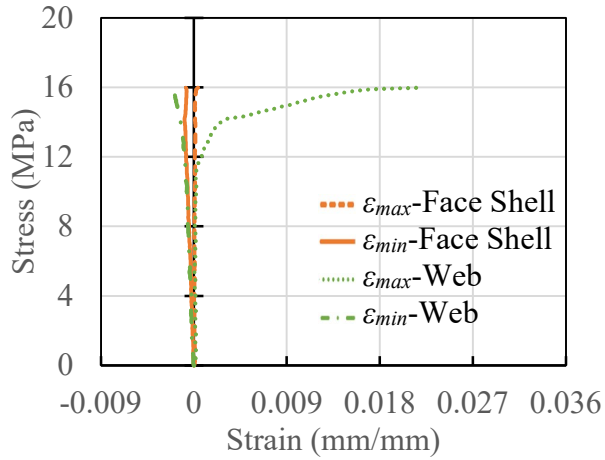


(d)

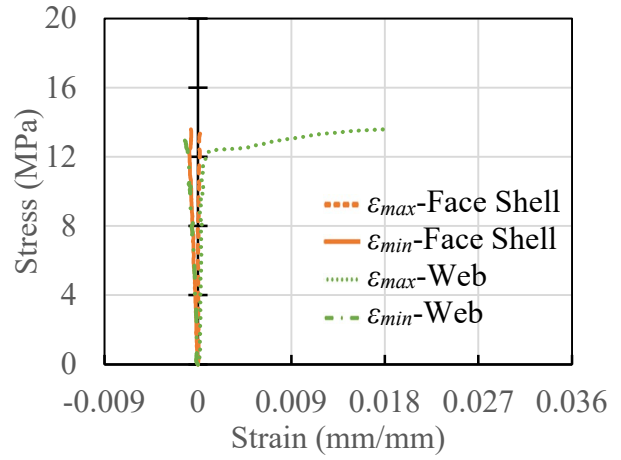


(e)

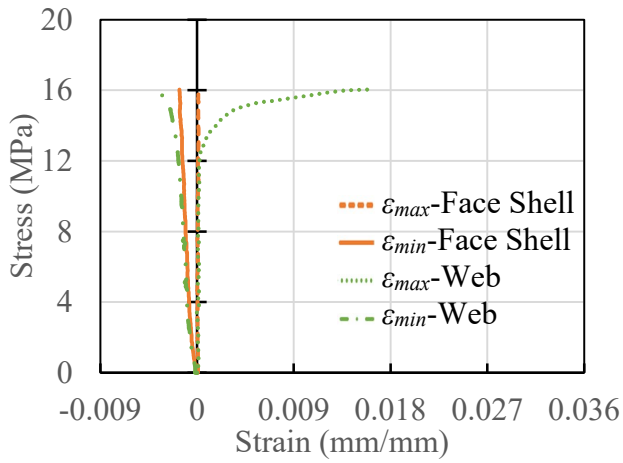
Figure 4C-29: Axial Stress versus Principal Strain Plot for Prisms: (a) B200G-1, (b) B200G-2, (c) B200G-3, (d) B200G-4, and (e) B200G-5



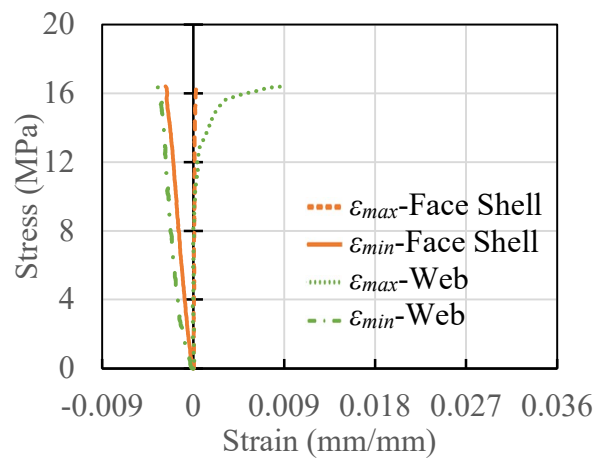
(a)



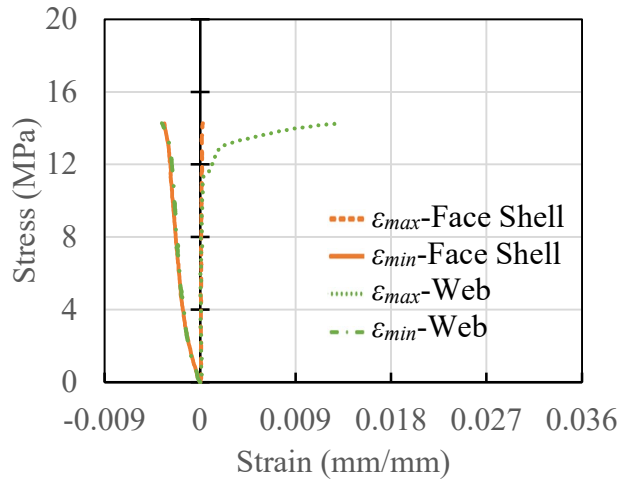
(b)



(c)



(d)



(e)

Figure 4C-30: Axial Stress versus Principal Strain Plot for Prisms: (a) C200G-1, (b) C200G-2, (c) C200G-3, (d) C200G-4, and (e) C200G-5

APPENDIX 4D: FINITE ELEMENT MODELING RESULTS

Figure 4D-1 shows that tapered face shells in CMUs resulted in different web widths (b_w) at different heights. This caused the width of the top surfaces of the three CMU types included in this study to be different due to the difference in CMU web heights. The width of the web at the top surface was always smaller than at the bottom surface and so the minimum web width was considered in this study to calculate the stress distribution. The maximum principal stress distribution was plotted at the top and bottom surfaces of the webs along its minimum width, which was automatically divided into forty-eight equal intervals. The corresponding maximum principal stress values, σ_{max} , at each interval were obtained from the FEM analysis and are shown in Tables 4D-1 to 4D-3. The identification mark for top and bottom web surfaces within each of the three block courses was explained in Section 4.4. For example, B1 represents the bottom surface of the exterior web within the top block course. The graphs resulting from these data were discussed in Section 4.4.

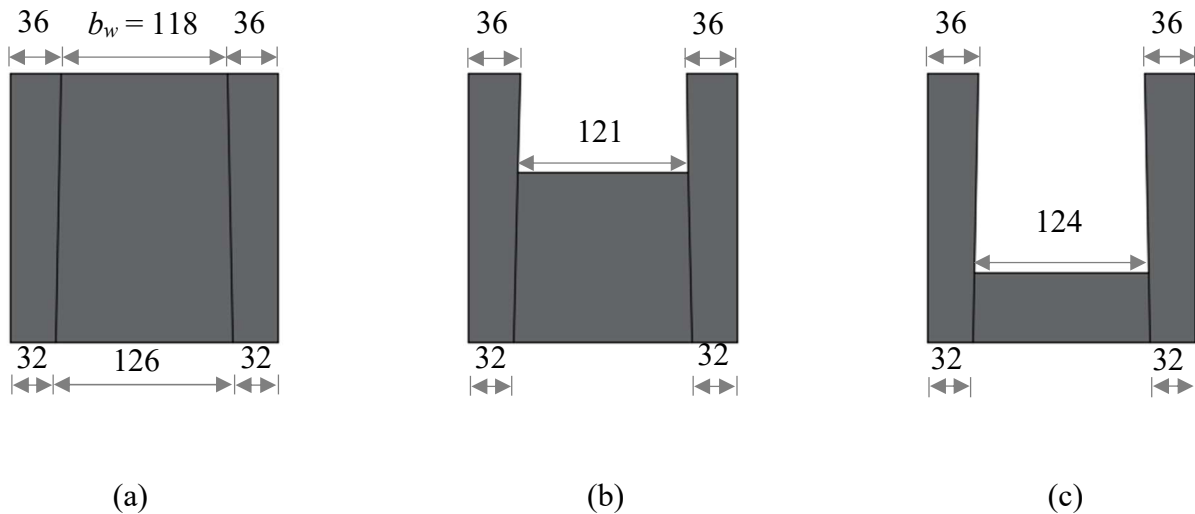


Figure 4D-1: Typical Width of the Web at the Top Surface for CMUs with: (a) Full-Height Webs, (b) 120 mm Tall Webs, and (c) 50 mm Tall Webs

Table 4D-1: Maximum Principal Stress Distribution - Test Series A200H

Position Along the Web Width (mm)	σ_{max} (MPa)					
	T1	B1	T2	B2	T3	B3
0	0.964	-2.49	-1.37	0.535	0.883	-2.64
2.46	1.19	0.615	0.733	0.471	0.958	-2.04
4.92	1.81	0.692	0.902	0.602	1.03	-1.43
7.38	2.46	1.36	1.21	1.27	1.34	-0.828
9.83	3.14	2.29	1.49	2.43	2.03	-0.224
12.3	3.87	3.27	1.95	3.04	2.87	0.387
14.8	4.63	3.79	2.69	3.48	3.87	1.39
17.2	4.67	3.85	2.88	3.95	4.02	1.30
19.7	4.62	3.90	3.06	4.33	4.08	1.27
22.1	4.59	3.96	3.25	4.70	4.15	1.32
24.6	4.56	4.02	3.46	5.04	4.22	1.44
27.0	4.54	4.08	3.67	5.12	4.27	1.61
29.5	4.51	4.14	3.89	5.19	4.28	1.80
32.0	4.48	4.20	3.92	5.26	4.28	1.97
34.4	4.45	4.20	3.96	5.30	4.29	1.98
36.9	4.43	4.20	3.99	5.35	4.29	2.00
39.3	4.40	4.20	4.02	5.38	4.30	2.02
41.8	4.38	4.20	4.06	5.38	4.29	2.04
44.3	4.36	4.20	4.09	5.39	4.29	2.05
46.7	4.34	4.19	4.10	5.40	4.29	2.07
49.2	4.32	4.18	4.11	5.40	4.29	2.08
51.6	4.29	4.17	4.12	5.41	4.29	2.09
54.1	4.29	4.16	4.12	5.41	4.29	2.10
56.5	4.29	4.15	4.12	5.41	4.29	2.11
59.0	4.29	4.14	4.12	5.41	4.29	2.12
61.5	4.29	4.14	4.12	5.41	4.29	2.10

Table 4D-1 Continued: Maximum Principal Stress Distribution - Test Series A200H

Position Along the Web Width (mm)	σ_{max} (MPa)					
	T1	B1	T2	B2	T3	B3
63.9	4.30	4.15	4.12	5.40	4.30	2.08
66.4	4.30	4.15	4.12	5.40	4.30	2.07
68.8	4.32	4.16	4.11	5.39	4.30	2.05
71.3	4.34	4.16	4.10	5.39	4.31	2.03
73.8	4.36	4.17	4.09	5.39	4.32	2.02
76.2	4.39	4.18	4.06	5.40	4.33	2.01
78.7	4.41	4.20	4.03	5.40	4.33	2.01
81.1	4.43	4.21	4.01	5.36	4.34	2.00
83.6	4.45	4.22	4.00	5.27	4.29	1.99
86.0	4.46	4.23	3.98	5.18	4.24	1.98
88.5	4.48	4.14	3.96	5.10	4.20	1.86
91.0	4.49	4.03	3.80	5.04	4.15	1.74
93.4	4.51	3.92	3.63	4.97	4.11	1.64
95.9	4.52	3.81	3.46	4.55	4.05	1.57
98.3	4.52	3.70	3.27	4.11	3.88	1.54
101	4.52	3.60	3.08	3.69	3.73	1.56
103	4.53	3.49	2.89	3.37	3.58	1.62
106	4.54	2.99	2.05	3.05	3.45	0.475
108	4.00	2.12	1.47	2.56	2.59	-0.154
111	3.05	1.30	1.09	1.62	1.43	-0.782
113	2.17	0.667	0.733	0.819	1.16	-1.41
116	1.37	0.622	0.601	0.485	0.908	-2.04
118	0.965	-2.54	-1.56	0.468	0.658	-2.66

Table 4D-2: Maximum Principal Stress Distribution - Test Series B200H

Position Along the Web Width (mm)	σ_{max} (MPa)					
	T1	B1	T2	B2	T3	B3
0	15.0	12.2	9.10	6.59	3.17	0.052
2.52	15.1	13.5	9.26	6.49	3.20	0.310
5.04	15.3	13.5	9.67	6.47	3.46	0.569
7.56	15.7	13.6	9.71	6.76	3.76	0.828
10.1	16.2	13.8	10.1	7.54	4.35	1.09
12.6	16.7	14.2	10.6	8.32	5.07	1.35
15.1	17.3	14.6	11.3	8.52	6.04	2.22
17.7	17.3	14.6	11.6	8.72	5.94	2.08
20.2	17.2	14.6	11.7	8.84	5.86	2.02
22.7	17.2	14.6	11.9	8.90	5.78	1.96
25.2	17.1	14.6	12.0	8.95	5.72	1.92
27.7	17.1	14.6	11.9	8.92	5.66	1.88
30.3	17.1	14.6	11.9	8.86	5.61	1.86
32.8	17.0	14.6	11.9	8.80	5.56	1.86
35.3	17.0	14.6	11.8	8.78	5.52	1.83
37.8	17.0	14.5	11.7	8.76	5.48	1.80
40.3	16.9	14.5	11.7	8.74	5.44	1.76
42.9	16.9	14.5	11.6	8.72	5.40	1.73
45.4	16.8	14.4	11.6	8.69	5.36	1.70
47.9	16.8	14.4	11.6	8.66	5.33	1.68
50.4	16.8	14.4	11.5	8.63	5.31	1.67
52.9	16.8	14.4	11.5	8.60	5.30	1.66
55.5	16.7	14.4	11.5	8.59	5.29	1.66
58.0	16.7	14.3	11.5	8.59	5.28	1.65
60.5	16.7	14.3	11.5	8.58	5.27	1.64
63.0	16.7	14.3	11.5	8.59	5.28	1.65

Table 4D-2 Continued: Maximum Principal Stress Distribution - Test Series B200H

Position Along the Web Width (mm)	σ_{max} (MPa)					
	T1	B1	T2	B2	T3	B3
65.5	16.7	14.4	11.5	8.60	5.29	1.65
68.1	16.8	14.4	11.5	8.61	5.30	1.66
70.6	16.8	14.4	11.5	8.63	5.32	1.67
73.1	16.8	14.4	11.6	8.66	5.33	1.68
75.6	16.8	14.4	11.6	8.69	5.37	1.70
78.2	16.9	14.5	11.6	8.73	5.40	1.73
80.7	17.0	14.5	11.7	8.76	5.44	1.75
83.2	17.0	14.5	11.7	8.79	5.48	1.78
85.7	17.1	14.6	11.8	8.81	5.52	1.81
88.2	17.1	14.6	11.8	8.83	5.55	1.83
90.8	17.2	14.6	11.9	8.87	5.58	1.83
93.3	17.3	14.6	11.9	8.92	5.62	1.86
95.8	17.4	14.6	11.8	8.92	5.66	1.92
98.3	17.4	14.5	11.8	8.83	5.72	2.0
101	17.5	14.5	11.8	8.74	5.78	2.10
103	17.6	14.5	11.9	8.57	5.85	2.21
106	17.7	14.5	11.7	8.35	5.92	2.39
108	16.9	14.2	11.0	8.15	5.00	1.46
111	16.3	13.8	10.4	7.51	4.31	1.17
113	15.8	13.6	9.8	6.81	3.75	0.889
116	15.3	13.5	9.8	6.40	3.44	0.611
119	15.1	13.5	9.4	6.34	3.19	0.332
121	15.0	12.2	9.3	6.40	3.16	0.054

Table 4D-3: Maximum Principal Stress Distribution - Test Series C200H

Position Along the Web Width (mm)	σ_{max} (MPa)					
	T1	B1	T2	B2	T3	B3
0	15.7	12.1	9.44	6.71	3.49	0.153
2.58	15.5	12.2	9.42	6.53	3.43	0.417
5.17	15.7	13.3	9.63	6.42	3.58	0.689
7.75	15.8	13.3	10.1	6.63	3.78	0.973
10.3	16.0	13.5	10.5	7.21	4.01	1.28
12.9	16.2	13.8	10.8	8.15	4.36	1.64
15.5	16.6	14.0	11.2	8.37	4.85	2.20
18.1	17.3	14.1	11.2	8.34	5.46	2.44
20.7	17.1	14.0	11.0	8.31	5.27	2.28
23.3	16.9	14.0	10.8	8.11	5.08	2.12
25.8	16.7	13.9	10.7	7.92	4.89	1.96
28.4	16.6	13.8	10.6	7.72	4.70	1.80
31.0	16.4	13.7	10.5	7.50	4.51	1.64
33.6	16.2	13.6	10.4	7.28	4.32	1.48
36.2	16.1	13.6	10.3	7.07	4.18	1.39
38.8	16.0	13.5	10.2	6.86	4.11	1.37
41.3	16.0	13.5	10.1	6.67	4.06	1.35
43.9	16.0	13.4	10.1	6.56	4.03	1.34
46.5	16.0	13.4	10.0	6.46	4.01	1.33
49.1	16.0	13.3	9.99	6.37	4.00	1.33
51.7	16.0	13.3	9.95	6.31	4.00	1.33
54.3	16.0	13.3	9.93	6.25	4.00	1.33
56.8	16.0	13.3	9.90	6.22	4.00	1.33
59.4	16.0	13.3	9.88	6.20	4.00	1.33
62.0	16.0	13.3	9.88	6.12	4.00	1.33
64.6	16.0	13.3	9.88	6.12	4.00	1.33

Table 4D-3 Continued: Maximum Principal Stress Distribution - Test Series C200H

Position Along the Web Width (mm)	σ_{max} (MPa)					
	T1	B1	T2	B2	T3	B3
67.2	16.0	13.3	9.90	6.12	4.00	1.33
69.8	16.0	13.3	9.92	6.22	4.00	1.33
72.3	16.0	13.3	9.94	6.31	4.00	1.33
74.9	16.0	13.3	9.97	6.40	4.00	1.33
77.5	16.0	13.4	10.0	6.48	4.00	1.33
80.1	16.0	13.4	10.1	6.57	4.00	1.33
82.7	16.0	13.5	10.1	6.66	4.00	1.33
85.3	16.0	13.5	10.2	6.83	4.00	1.33
87.8	16.0	13.6	10.3	7.02	4.08	1.34
90.4	16.2	13.6	10.4	7.22	4.24	1.41
93.0	16.4	13.7	10.5	7.46	4.45	1.58
95.6	16.6	13.8	10.6	7.69	4.67	1.74
98.2	16.9	13.9	10.7	7.81	4.88	1.91
101	17.1	13.9	10.8	7.87	5.10	2.07
103	17.3	14.0	11.1	7.93	5.31	2.24
106	17.5	14.1	11.3	8.10	5.53	2.40
109	16.7	14.0	11.2	8.27	4.72	2.20
111	16.2	13.7	10.8	8.17	4.21	1.62
114	16.0	13.5	10.5	7.56	3.94	1.24
116	15.8	13.3	10.1	6.91	3.70	0.943
119	15.6	13.3	9.62	6.73	3.47	0.693
121	15.4	12.0	9.32	6.82	3.28	0.458
124	15.6	12.0	9.35	6.96	3.41	0.226